

ABSTRACT

Title of dissertation: DYNAMICS OF SLENDER,
FLEXIBLE STRUCTURES

Nicholas Vljajic, 2014

Dissertation directed by: Professor Balakumar Balachandran
Department of Mechanical Engineering

Dynamics of slender beam-like structures subjected to rotational motions is studied experimentally, numerically, and analytically within this dissertation. As the aspect ratio of beam-like structures is increased (i.e., as the structures become slender), the structure can undergo large elastic deformations, and in addition, the torsional and lateral motions can be strongly coupled. Two different paradigms of rotor systems are constructed and used to investigate coupled torsional-lateral motions in slender rotating structures. The first rotor model is a modified version of the classical Jeffcott rotor, which accounts for torsional vibrations and stator contact. Analysis and simulations indicate that torsional vibrations are unlikely to exist during forward synchronous whirling, and reveal the presence of phenomena with high-frequency content, such as centrifugal stiffening and smoothening, during backward whirling. The second rotor model is a nonlinear distributed-parameter system that has been derived with the intent of capturing dynamics observed in an experimental apparatus with slender, rotating structures. Nonlinear oscillations observed in the experiments contain response components at frequencies other than

the drive speed, a feature that is also captured by predictions obtained from the distributed-parameter model. Further analysis of the governing partial-differential equations yields insights into the origins (e.g., nonlinear gyroscopic coupling and frictional forces) of the nonlinear response components observed in the spectrum of the torsion response. Slender structures are often subject to large deformations with pre-stress and curvature, which can drastically alter the natural frequencies and mode shapes when in operation. Here, a geometrically exact beam formulation based on the Cosserat theory of rods is outlined in order to predict the static configuration, natural frequencies, and mode shapes of slender structures with large pre-stress and curvature. The modeling and analysis are validated with experiments as well as comparisons with a nonlinear finite element formulation. The predictions for the first eight natural frequencies are found to be in excellent agreement with the corresponding experimentally determined values. The findings of this dissertation work have a broad range of applications across different length scales, including drill strings, space tethers, deployable structures, cable supported structures (e.g., bridges and mooring cables), DNA strands, and sutures for non-invasive surgery to name a few.

DYNAMICS OF SLENDER, FLEXIBLE STRUCTURES

Nicholas A. Vljic

Dissertation submitted to the Faculty of the Graduate School of the
University of Maryland, College Park, in partial fulfillment
of the requirements for the degree of
Doctor of Philosophy
2014

Advisory Committee:

Professor Balakumar Balachandran, Chair and Advisor

Professor Amr Baz, Department of Mechanical Engineering

Associate Professor Nikhil Chopra, Department of Mechanical Engineering

Distinguished University Professor Stuart Antman, Department of Mathematics

Professor Konstantina Trivisa, Department of Mathematics and AMSC (Dean's
Representative)

© Copyright by
Nicholas A. Vlajic
2014

Acknowledgments

I would like to thank Professor Balachandran for his guidance throughout this dissertation work. He gave me the opportunity to pursue aspects of research that interested me, and always made time to help when I encountered difficulties. I am also thankful for the help and discussions that I've had with current and former lab members at the University of Maryland. Further, I am grateful for the partial support of this work provided by the Energy and Education Research Collaboration between the University of Maryland and the Petroleum Institute, United Arab Emirates. Finally, I would especially like to thank my family for their unwavering support and encouragement throughout my dissertation work.

Table of Contents

List of Tables	v
List of Figures	vi
1 Introduction	1
1.1 Literature review of rotor dynamics and applications	2
1.1.1 Literature review on rotor dynamics	2
1.1.2 Drilling mechanics and drill strings	9
1.2 Literature review on dynamics of curved beams	12
1.2.1 Arches and rings	13
1.2.2 Buckled and pre-stressed beams	14
1.3 Scope and dissertation objectives	16
1.4 Organization of dissertation	17
2 Torsional Motions of the Jeffcott Rotor with Continuous Stator Contact	19
2.1 Jeffcott model and governing equations	20
2.1.1 Derivation of equations of motion	20
2.1.2 External stator forces and friction	22
2.2 Characteristic whirl phenomena	26
2.3 Simplification of the governing equations	27
2.3.1 Reduction of structural terms	27
2.3.2 Approximation of external forces and contact	29
2.3.3 Non-dimensionalization	31
2.4 Torsion response during forward whirling motions	32
2.5 Torsion response during backward whirling motions	39
2.5.1 Governing equation and equilibrium	39
2.5.2 Low-speed backward whirling	40
2.5.3 High-speed backward whirling	42
2.6 Summary	52
3 Rotor Dynamics with Coupled Torsional-Lateral Motions with Gyroscopic Effects	54
3.1 Experimental arrangement	55
3.2 Experimental results	57
3.2.1 Characteristic whirl phenomena	57
3.2.2 Torsional vibrations with continuous rotor-stator contact	62
3.2.2.1 Forward whirling	64
3.2.2.2 Backward whirling	64
3.3 Modeling efforts	65
3.3.1 Distributed-parameter structural model	66
3.3.2 Rotor-stator force-interaction model	74
3.4 Simulation Results	78
3.4.1 Characteristic whirl motions	78

3.4.2	Torsional vibrations during forward and backward whirl motions	80
3.4.2.1	Forward whirling	80
3.4.2.2	Backward whirling	81
3.5	Further reduced-order modeling and analysis	85
3.5.1	Forward whirling	86
3.5.2	Backward whirling	87
3.6	Summary	89
4	Modal Analysis of Geometrically Exact Beams with Pre-stress and Curvature	91
4.1	Geometrically exact model	92
4.1.1	Governing equations of motion	93
4.1.2	Beam kinematics and governing equations	95
4.1.3	Static analysis	95
4.1.4	Modal analysis about the pre-stressed configuration	100
4.2	Experimental studies	107
4.3	Comparison of experimental results, theory, and finite element analysis	110
4.4	Summary	115
5	Summary of Contributions and Recommendations for Future Studies	116
5.1	Coupled motions in rotor systems	116
5.2	Geometrically exact structures	119
A	Derivation of 1-2-3 Euler Angles and Angular Velocity	121
B	Kinetic Energy for Coupled Bending and Torsion Model	124
C	Coefficients for Coupled Bending and Torsional Model	128
D	Modal Analysis of Pre-stressed Semi-circular Configurations	130
E	ANSYS Input File for Experimental Parameters	138

List of Tables

2.1	Parameter values used in simulations	25
3.1	Experimental arrangement parameters used in simulations.	58
3.2	Friction parameters used in simulations.	77
4.1	Experimental dimensions and parameters used in the model and finite element analysis. Superscript asterisks (*) denote tabulated parameters, while the remaining parameters and dimensions are measured quantities.	112
4.2	Experimentally observed natural frequencies of the curved structure compared with predictions from the model and finite element model.	113
D.1	Natural frequencies for different semi-circular configurations predicted by the model and found with finite elements. *The finite element analysis also includes a prediction of a natural frequency at 157.64 Hz, which is omitted because it is associated with a combination of bending and centerline stretching.	137

List of Figures

1.1	Jeffcott rotor: (a) physical system and (b) schematic used for modeling.	3
1.2	Jeffcott rotor within a stator in the (a) static configuration and (b) at an instant of time.	4
1.3	Frequency response function for the Jeffcott rotor contained within a stator.	5
1.4	Characteristic motions of the Jeffcott rotor contained within a stator: (a) definitions used in describing the response, (b) forward whirling without contact, (c) forward whirling with contact, and (d) backward whirling with contact.	6
1.5	Schematic of a typical rotary drilling operation.	11
2.1	(a) Static configuration of the rotor within the stator. (b) Rotor system in a dynamic state.	22
2.2	(a) Illustration for defining parameters used in the friction coefficient. (b) Graphical depiction of change in friction coefficient for different values of v_m	25
2.3	Numerically generated solutions for stable responses of the system given by equations (2.4a)-(2.8) and (2.12).	28
2.4	Stability dependence on the friction parameter v_m when the damping ratio is set to $\zeta = 0.01$. Dotted lines represent unstable solutions while solid lines represent stable solutions for the equilibrium position θ_{eq}	35
2.5	Stability dependence on structural damping ζ . Dotted lines represent unstable solutions while solid lines represent stable solutions for the equilibrium position θ_{eq} for $v_m = 0.3$	36
2.6	Comparisons of the results from the full system (equations (2.4a)-(2.8) and (2.12)) and the reduced-order system (equations (2.24) and (2.12)) at $\Omega = 4.0$ rad/s. Perturbations decay in cases (a)-(c) and grow in case (d). (a) Whirl speed is greater than the minimum friction speed ($v_w > v_m$) in the presence of structural damping, (b) whirl speed is greater than the minimum friction speed ($v_w > v_m$) even without structural damping ($\zeta = 0$), (c) whirl speed is less than the minimum friction speed ($v_w < v_m$) in the presence of structural damping, and (d) whirl speed is less than the minimum friction speed ($v_w < v_m$) in the absence damping ($\zeta = 0$).	38
2.7	Effective friction coefficient given by equation (2.55) for $\Delta = 0.032$ corresponding to $\tilde{\alpha} = 12$	49
2.8	(a) Cross section of Figure 2.7 at $z = 0$ for different values of Δ . (b) Effective normal force at $z = 0$ for different values of Δ	49
2.9	(a) Fast-scale and slow-scale variable histories (equations (2.43) and (2.58)). (b) Analytical approximation history (equations (2.43), (2.58), and (2.40)). (c) Simulations of reduced-order system (equation (2.33)). (d) Simulations of full system (equations (2.4a)-(2.8) and (2.12)).	51

3.1	Vertical drill string experimental apparatus.	57
3.2	Experimentally observed forward whirling motions: (a) trajectory of rotor center within the stator, (b) time histories of the $v(L, t)$ and $w(L, t)$ displacement components, and (c) Fourier spectra of complex displacement quantity.	60
3.3	Experimentally observed backward whirling motions: (a) trajectory of rotor center within the stator, (b) time histories of the $v(L, t)$ and $w(L, t)$ displacement components, and (c) Fourier spectra of complex displacement quantity.	61
3.4	Experimentally observed impacting motions: (a) trajectory of rotor center within the stator, (b) time histories of the $v(L, t)$ and $w(L, t)$ displacement components, and (c) Fourier spectra of complex displacement quantity.	63
3.5	Experimentally determined frequency content of torsional strain during forward synchronous whirling.	65
3.6	Experimentally determined frequency content of torsional strain during dry-friction whirling.	66
3.7	Schematic of the structural model used to develop the governing equations of motion.	68
3.8	Schematic of forces when the rotor is in contact with the stator. . . .	75
3.9	Coefficient of friction μ as a function of the relative speed for the model given by equation (3.27).	76
3.10	Comparisons for the same input parameters: (a) experimental results and (b) numerical results.	79
3.11	Normalized Fourier spectra of the simulated torsional displacement for forward whirling with stator contact.	81
3.12	Two typical system responses for forward synchronous whirling: (a) Relative speed for 50 RPM, (b) relative speed for 51 RPM, (c) Fourier spectra of the steady-state torsion displacement for 50 RPM, and (d) Fourier spectra of the steady-state torsion displacement for 51 RPM.	82
3.13	Normalized Fourier spectra of the simulated torsional displacement for backward whirling with stator contact.	83
3.14	Two typical system responses for backward, dry-friction whirling: (a) Relative speed for 13 RPM, (b) relative speed for 34 RPM, (c) Fourier spectra of the steady-state torsion displacement for 13 RPM, and (d) Fourier spectra of the steady-state torsion displacement for 34 RPM.	84
3.15	Torsion response spectra determined by equation (3.35) for forward whirling motions.	88
3.16	Torsion response spectra determined by equation (3.34) for forward whirling motions.	88
4.1	Description of the variables used to describe the motion of the rod structure.	95
4.2	General static configurations admitted by equations (4.15). The solutions shown here have been numerically determined.	99

4.3	Description of the variables used to describe the motion of the beam about the pre-stressed configuration.	101
4.4	(a) Experimental arrangement used to determine the natural frequencies of a pre-stressed beam. (b) Detailed view of the bottom assembly.	108
4.5	Schematic of the experimental arrangement used to study the dynamics of slender structures.	109
4.6	Normalized strain-acceleration response for the curved structure shown in Figure 4.4.	111
4.7	One frame of the video with the backlit structure in black, the static configuration (dashed line), and the estimated current configuration (dots) from the image processing.	112
4.8	Static configuration and mode shapes from the experiments (black dots), the model formulation (solid black line) and finite element results. (a) Static configuration, (b) mode 1, (c) mode 2, and (d) mode 3.	114
A.1	Euler angles used to express the angular velocity of the structure. . .	122
B.1	Segment of the shaft in both the undeformed and deformed configuration.	126
D.1	Four different configurations for the semi-circle parameter ξ that satisfies equations (4.15) with boundary conditions (D.1). The analytical solution is given by equations (D.2), and numerical solutions are obtained through direct integration of equations (4.15) with boundary conditions (D.1).	132
D.2	Comparisons of the mode shapes determined from the model and the finite element modeling. Thin dashed lines represent the static configuration. Solid black lines are the mode shapes determined by the model, given by the differential eigenvalue problem (D.4) and spatial solution, equation (D.6).	136

Chapter 1

Introduction

Flexible structures occur in a variety of natural and synthetic systems, such as space tethers, deployable structures, cable supported structures (e.g. bridges and mooring cables), mechanics of deoxyribonucleic acid (DNA) strands, and sutures for non-invasive surgery to name a few. These structures are distinct from traditional engineering structures because of their high aspect ratios. These structures can undergo large deformations, and in addition, torsional, lateral, and axial motions can be strongly coupled. In certain instances, these structures also experience intermittent impacts and collisions with physical boundaries. These unique features can lead to strong nonlinear effects in the dynamic response of the system. Furthermore, slender structures may also operate under the effects of pre-stress or an initial static configuration (e.g., bridge cables). This initial pre-stress and curvature can drastically change the natural frequencies of the system, or can lead to a nonlinear response of the structure.

Within this dissertation, the dynamics of slender structures are explored experimentally, numerically, and analytically. The dynamics of drill strings, which is examined in the following section, is one physical system of interest, since they share many aspects common to slender structures in operation, such as intermittent contact with physical boundaries, coupling between different motions, and pre-stressed

and curved configurations. All three of these aspects will be explored within this dissertation, with emphasis on the latter two. The findings and results presented here have applications to slender structures across different length scales.

1.1 Literature review of rotor dynamics and applications

1.1.1 Literature review on rotor dynamics

The classical rotor system originally developed by Henry Jeffcott (Jeffcott, 1919) is shown in Fig. 1.1. This simplified, lumped-parameter model of a rotor has served as the basis for numerous studies found in the literature. The governing equations of motion may be written as

$$(M + m)\ddot{y} + c\dot{y} + ky = me\Omega^2 \cos \Omega t \quad (1.1)$$

$$(M + m)\ddot{z} + c\dot{z} + kz = me\Omega^2 \sin \Omega t \quad (1.2)$$

In equation (1.2), M is the mass of the rotor, m is the effective mass imbalance, e is the eccentricity, k is the stiffness of the rotor, c is the linear damping and Ω is the drive speed of the rotor. When under rotation, the rotor will whirl in a circular orbit about the origin due to the effective eccentricity and unbalanced mass. If the rotor is not symmetric (i.e., the mass, stiffness, and damping are not equivalent in the y and z directions), then the orbit will be elliptical. Although this lumped-parameter model is able to explain a variety of rotor dynamic phenomena, it does not account for certain dynamics, such as rotor-stator contact, torsional vibrations, or gyroscopic effects (i.e., rotations of the rotor about the y and z axes). A literature review of

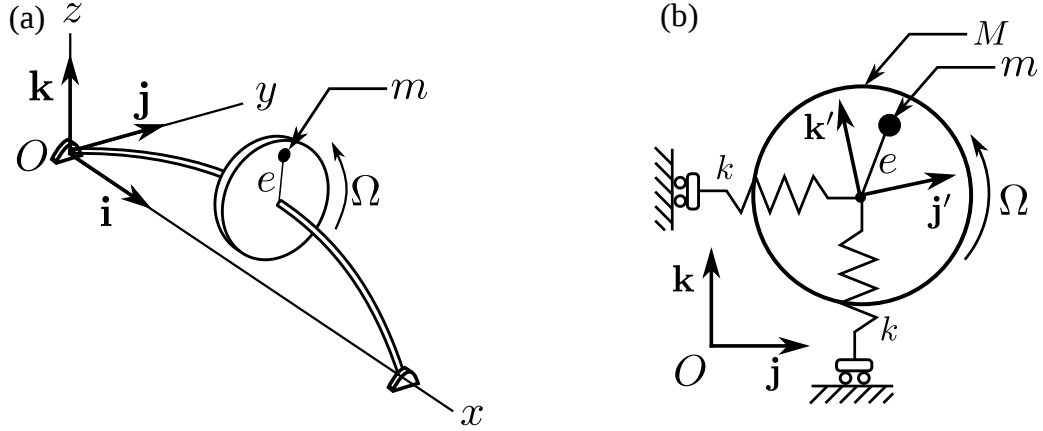


Figure 1.1: Jeffcott rotor: (a) physical system and (b) schematic used for modeling.

relevant rotor dynamic studies, as well as in introduction to certain rotor dynamic phenomena, is presented next.

Rotor-stator phenomena

Some form of rotor-stator contact exists in almost all rotating equipment. A schematic of the modified Jeffcott rotor contained within a stator, which is commonly studied in the literature, is provided in Figure 1.2. Within Figure 1.2, the quantity δ is the initial gap clearance between the rotor and the stator and Γ is the radial displacement of the geometric center of the rotor to the origin, and is stated

$$\Gamma(x, y) \equiv \Gamma = \sqrt{x^2 + y^2} \quad (1.3)$$

During run-up or run-down of a rotor system, the rotor may come into contact with a stator. Under certain circumstances, the rotor will stay in continuous contact with the stator, even while the drive speed is being varied, and whirl either in the direction of motor rotation or in the opposite direction of rotation. Some of the forward whirling and backward whirling solutions that were studied by Black (1967,

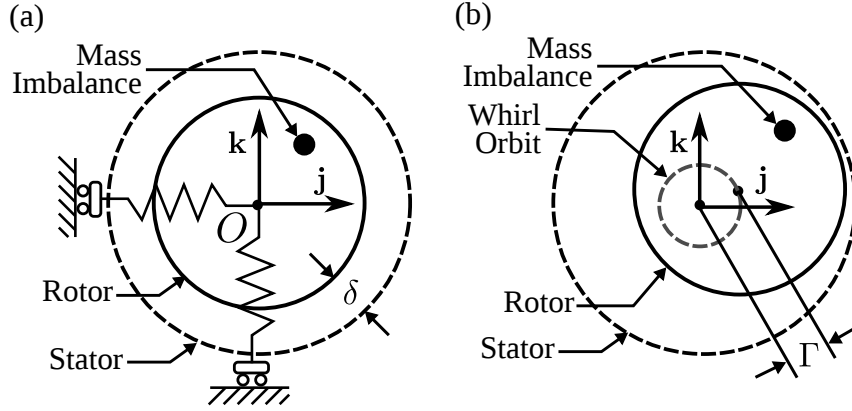


Figure 1.2: Jeffcott rotor within a stator in the (a) static configuration and (b) at an instant of time.

1968) for the Jeffcott Rotor contained within a stator subject to dry-friction are shown in Figure 1.3. Note that other backward whirling solutions exist for asymmetrical rotors and rotor systems with dominant gyroscopic terms, which are not shown on in Figure 1.3 for clarity (for instance, see Genta (2005); Yamamoto and Ishida (2001); Yabuno, Kashimura, Inoue, and Ishida (2011)). In Figure 1.3, the non-dimensional radial displacement is plotted as a function of the non-dimensional driving speed. Here, the rotor makes contact with the stator when $\Gamma/\delta \geq 1$ and lateral resonance occurs at $\Omega_{nd} = 1$. For this system, there are three stable solutions, namely forward whirling without stator contact, forward whirling with stator contact, and backward whirling with stator contact. A schematic of the rotor-stator motion for these three stable solutions, shown by points *b*, *c*, and *d* in Figure 1.3, are given in Figure 1.4(b)-(d), respectively. The rotor motion during forward whirling without contact is provided in Figure 1.4(b). During forward synchronous whirl, the rotor whirl frequency (or precession rate about the origin) is close to that of

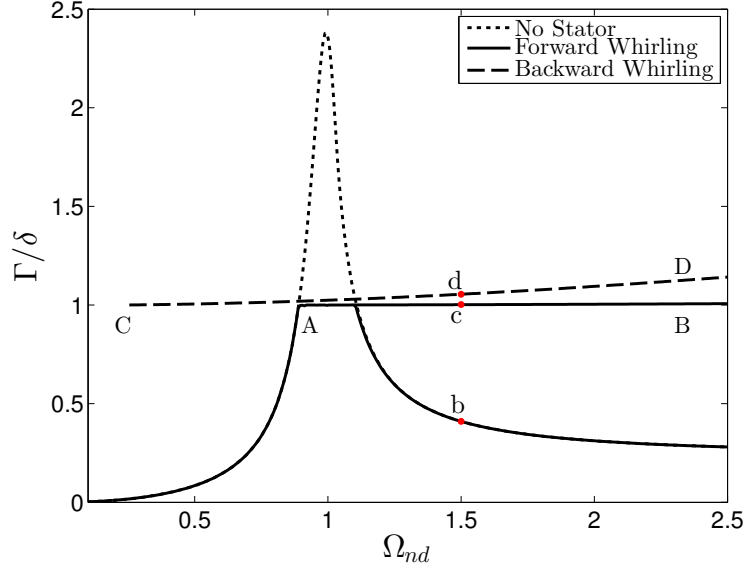


Figure 1.3: Frequency response function for the Jeffcott rotor contained within a stator.

the driving speed. Similarly, forward whirling with contact, also referred to as *synchronous rubbing* in the literature, is given by line segment AB in Figure 1.3 and the rotor motion is shown in Figure 1.4(c). Again, during forward synchronous rubbing, the rotor whirl frequency (or precession rate about the origin) is close to that of the driving speed. During synchronous whirling with contact, the rotor is also said to be *slipping*, where the relative speed between the rotor and zero is non-zero. In other instances, the rotor may come into contact with the stator, and start to undergo backward whirling with contact (also referred to as *dry-friction whirl*, counterwhirl, or rolling), which is represented by line segment CD in Figure 1.3, and the rotor motion is shown in Figure 1.4(d). For dry-friction whirl, the rotor whirl speed may be approximated by the equation

$$f_w = -f_d \frac{R}{\delta} \quad (1.4)$$

by imposing the *no-slip* condition; that is, the relative speed between the rotor and

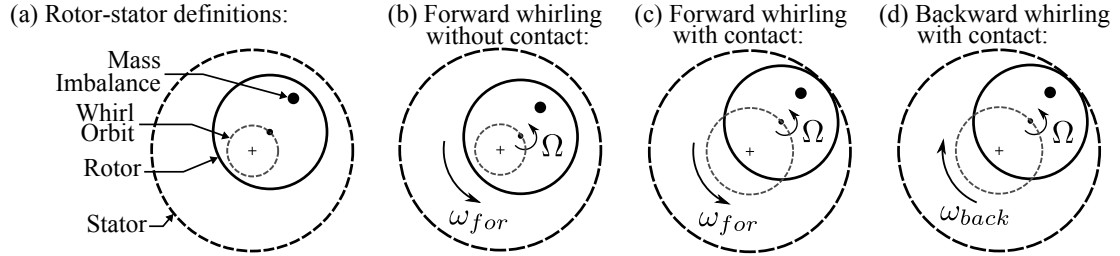


Figure 1.4: Characteristic motions of the Jeffcott rotor contained within a stator: (a) definitions used in describing the response, (b) forward whirling without contact, (c) forward whirling with contact, and (d) backward whirling with contact.

stator is zero. If the rotation speed of the motor is continuously increased while undergoing dry-friction whirling, eventually, the whirl speed saturates and the rotor is said to undergo *whip*. The mechanism through which the rotor transitions from whirl to whip has been studied by Childs and Bhattacharya (2007); Bartha (2000); Jiang and Ulbrich (2005), and others, but remains to be well understood. All three of these stable solutions coexist for the same system parameters. The initial conditions of the rotor determine which steady-state solution the rotor will attract to.

In the presence of a stator, rotors can also undergo *relative stick-slip* behavior. In the *stick* phase, the relative speed between the rotor and stator is zero, while during the *slip* phase the relative speed between the rotor is non-zero. During *relative stick-slip* the rotor undergoes a combination of both sticking and slipping, which can act to excite torsional motions in slender rotor systems. Stick-slip behavior is seen in other mechanical systems (e.g., squeal of brakes, the excitation of bowed instruments, wheels of train cars) and has been studied by Oestreich, Hinrichs, and Popp (1996); Leine and Nijmeijer (2004), and Leine, van Campen, Kraker, and van den Steen (1998) as well as others.

Coupled motions of slender structures

In traditional rotating structures, torsional vibrations are often considered to be independent of the lateral or bending vibrations. However, as the aspect ratio of a structure increases, the coupling among the torsional, lateral, and axial motions may become stronger. This potential coupling is made apparent with the following arguments. The linear natural frequencies for torsional and axial modes of vibration scale proportionally to the inverse of the length of the structure, while the natural frequencies for lateral or bending modes scale proportionally to the inverse of the length squared. As the length of the structure is increased, the natural frequencies of the three different motions decrease, and likewise, the spacing between the natural frequencies for each direction also decreases. If the natural frequencies of the different motions become close, energy may be exchanged between the torsional, axial, and lateral modes, and the structure is able to exhibit motions which are a combination of the different modes. Furthermore, the three motions may be strongly coupled through the boundary conditions of the structure, such as systems with lumped-mass elements. Since one aspect of this dissertation is concerned with structures that rotate, particular interest is given to the coupling between torsional and lateral motions.

A review is given here of studies which have focused on the response of rotors with coupled lateral and torsional motions in the absence of external stator forces. Nataraj (1993) developed a distributed-parameter structural model, and used perturbation analysis to show that the amplitude of torsional motions are second-order,

while lateral motions dominate the first-order response. Huang (2007) compared a numerically generated frequency-amplitude response for torsional vibrations with an experimental rotating shaft for forward synchronous whirling, and found a lateral vibration response component at twice the drive speed when driving the system at the first torsional resonance. Hosseini and Khadem (2009b) derived a distributed-parameter rotor model with torsional, bending, and axial coupling based on the kinematics and modeling of Nayfeh and Pai (2004), and performed perturbation analysis on the resulting model. Through numerical simulation and analysis, they determined that nonlinearities in stiffness and inertia excite both forward and backward whirling motions of the rotor without stator contact. Efforts with the aim of modeling coupled torsional-bending motions for finite element implementation include those of Hsieh, Chen, and Lee (2006) and Wu (2007).

The problem of coupled torsional-bending vibrations in rotor systems becomes more complex when accounting for rotor-stator contact and force-interactions. Edwards, Lees, and Friswell (1999) performed a numerical parametric study varying torsional parameters and found that the modified Jeffcott rotor can exhibit chaotic, torsional motions. In an experimental effort, Diangui (2000) found the natural frequency of torsional vibrations increase when the rotor is in contact with the stator during forward whirling, but this was not explained in that study. The potential origin of this stiffening behavior is explained in Chapter 2 of this dissertation. The effects of different frictional forces on the torsion response of lumped-parameter rotor system was investigated in the efforts of Mihajlovic, van de Wouw, Rosielle, and Nijmeijer (2007) and Mihajlovic (2005). In these efforts, the researchers constructed

stable and unstable solutions of the system, and verified their existence experimentally. It is noted that in system presented in the works of Mihajlovic *et. al* (Mihajlovic, van Veggel, van de Wouw, and Nijmeijer, 2004) and Mihajlovic (Mihajlovic, 2005), the rotor was subject to follower-forces; that is, frictional forces acted on the rotor for all lateral displacement. Stick-slip interactions and the nonlinear response of torsional vibrations of a rotor-stator system were explored numerically and experimentally in the efforts of Liao, Balachandran, Karkoub, and Abdel-Magid (2011) and Liao, Vlajic, Karki, and Balachandran (2012).

1.1.2 Drilling mechanics and drill strings

One application of slender rotating structures occurs in the use of drill strings that are used to bore holes into the Earth in order to retrieve natural resources such as petroleum and natural gas. Often times, these slender structures can extend several kilometers below the Earth's surface. A schematic of a typical rotary drill rig and drill-string assembly is provided in Figure 1.5. A drill string is a complex structure, which consists of hollow steel pipes screwed together to form a long continuous structure, and frequently, sections with larger diameters, referred to as stabilizers, are inserted in between two drill pipes to help keep the drill string in the center of the borehole. The base of the drill string is made of two main components, namely the drill collar and the drill bit. Drill collars are similar to drill pipes, except that they are larger in diameter and they help to provide weight-on-bit. A drill bit, the tool which breaks down the rock and soil, is secured at the end of the drill collar

assembly. The entire drill string assembly is rotated at the surface by using a rotary table and a motor. This actuation is transmitted down the drill string and to the drill bit, where it then acts to crush the rock and soil. Throughout the drilling process, a hydraulic fluid, known as drill mud, is pumped down through the center of the drill string and collars and serves two purposes. Not only does the mud keep the drill bit cool and lubricated, it also washes away the broken rock and soil. After the mud flows through the drill strings and the collars, it then flows in the annulus between the drill string and borehole carrying the cuttings to the surface.

A brief literature review of dynamics and control of drill strings is presented here. Jansen (1993) used a simplified rotor with an unbalanced mass supported by two bearings, which has since served as the basis for several other efforts with the intent of modeling drill strings. Kreuzer and Struck (2005) used a distributed-parameter model for the drill string and a proper orthogonal decomposition procedure to develop a reduced system model and build a control scheme. Their model predictions were verified with experimental results. Other spatially continuous models that have been developed include those presented in the work of Khulief and Al-Sulaiman (2007) and Piovan and Sampaio (2006). In both of these efforts, a finite element formulation is used to examine nonlinear vibrations of drill strings. Christoforou and Yigit (1997) used a Hertzian contact model and showed that chaotic dynamics and parametric resonances are possible.

Additionally, drill-string assemblies are subject to several non-smooth forces. For instance, the interaction forces between the drill bit and the well bottom, the drill bit and the well bore, and finally the drill string and the well bore. Because

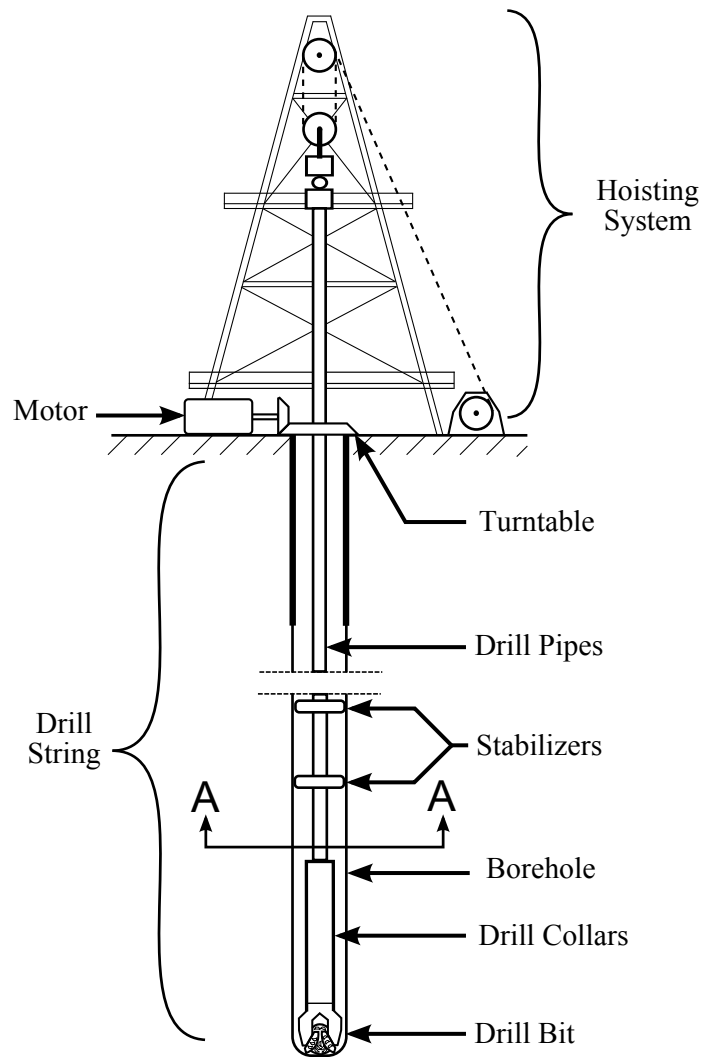


Figure 1.5: Schematic of a typical rotary drilling operation.

of the non-smooth interaction forces, another phenomena arises known as *absolute stick-slip*. It is noted that absolute stick-slip is different from relative stick-slip. In the *absolute stick* phase, the absolute angular speed of the drill bit is zero. In other words, the drill-bit becomes stuck on the rocks and soil. While the forces prevent the drill-bit from moving, the top motor can continue to turn and the drill string begins to twist, causing an increase in potential energy. Once the drill-bit breaks free, the absolute speed can increase to twice the drive speed of the motor. This violent motion is referred to as *absolute slip*. A few notable works which have studied the absolute stick-slip of drill strings include those of Yigit and Christoforou (2006), Leine, van Campen, and Keultjes (2002), and Leine and van Campen (2005).

1.2 Literature review on dynamics of curved beams

As previously mentioned, often times slender structures are initially manufactured in a straight configuration, but operate with initial pre-stress and about a curved configuration. This initial pre-stress and curvature can change the natural frequencies of the structure. Calculating and predicting the natural frequencies about the pre-stressed configuration is a problem of interest for design purposes as well as structural health monitoring.

Within the literature, researchers have studied large static deformations of initially straight beams, or have studied the dynamics of initially straight beams with pre-stress and relatively small-amplitude buckled configurations (i.e., displacements on the order of the beam thickness). Few efforts have focused on the dynamics of

initially straight beams that have been subject to a large static displacement with pre-stress and variable curvature, as will be addressed in this dissertation. A review of the dynamics of curved and pre-stressed beams is presented next.

1.2.1 Arches and rings

In most of the prior work, wherein the dynamics of non-straight beam structures have been considered in the context of arches or rings, the effects of pre-stress and neglected and/or special configurations, such as parabolic, hyperbolic, or semi-circular, are considered. A brief review of the dynamics of arches and ring structures is given next. Tüfekçi and Arpaci (1998) analytically determined the mode shapes and natural frequencies specific to circular arches; they included centerline extension, shear, and rotary inertia, for different boundary conditions. Oh, Lee, and Lee (1999) used a numerical scheme to determine the natural frequencies and mode shapes for non-circular arches with rotary inertia and shear effects. The results were in good agreement with finite element predictions. Extending on this work, Oh, Lee, and Lee (2000) investigated the influence of non-uniform cross-sections on non-circular arches. Their work was validated with experimental data. Chidamparam and Leissa (1995) investigated the influence of the centerline extensibility in circular arches with the effects of pre-stress. They determined that the centerline stretching decreases the natural frequencies, and this decrease can be considerable for certain geometries. Matsunaga (1996) found approximate solutions through series expansions of the buckling loads and natural frequencies for shallow circular beams that can un-

dergo shear. Recently, within the context of shells, Lacarbonara and Antman (2012) studied the stability of nonlinear viscoelastic shells with a combined pre-stress load and dynamic load in the form of pulsating pressure.

1.2.2 Buckled and pre-stressed beams

The studies (Tüfekçi and Arpacı, 1998; Oh, Lee, and Lee, 1999, 2000; Chidamparam and Leissa, 1995; Matsunaga, 1996; Lacarbonara and Antman, 2012) all considered initially curved geometries. On the other hand, the following studies (Nayfeh and Kreider, 1995; Kreider and Nayfeh, 1998; Lacarbonara, Nayfeh, and Kreider, 1998; Nayfeh and Emam, 2008; Li and Balachandran, 2006; Li, Preidikman, Balachandran, and Mote, 2006; Anderson, Nayfeh, and Balachandran, 1996; Lacarbonara, Paolone, and Yabuno, 2004; Addessi, Lacarbonara, and Paolone, 2005) analyzed the dynamics of initially straight beams deformed to pre-stressed or buckled configurations. Nayfeh and Kreider (1995) gave a closed form solution for the linear natural frequencies and mode shapes of a buckled beam with fixed-fixed, fixed-hinged, and hinged-hinged boundary conditions. The predictions for the fixed-fixed boundary conditions were confirmed experimentally. Initial pre-stress and curvature not only change the linear natural frequencies of a structure, but they can also accentuate the nonlinear response when subject to an excitation. Investigations into the nonlinear response and resonances of a fixed-fixed buckled beam were carried out by Kreider and Nayfeh (1998). Lacarbonara, Nayfeh, and Kreider (1998) used experimental data to compare different reduction methods to analyze nonlinear res-

onance behavior of a fixed-fixed buckled beam. More recently, Nayfeh and Emam (2008) determined an exact solution to the post-buckled configuration of a beam for different boundary conditions. The linear natural frequencies and dynamic stability around these configurations were also determined. Li and Balachandran (2006) and Li, Preidikman, Balachandran, and Mote (2006) investigated the free and forced response of a clamped-clamped, buckled piezoelectric microresonator. The analytical frequency-amplitude response and experimental data revealed stiffening-type behavior. Anderson, Nayfeh, and Balachandran (1996) explored the nonlinear response of a vertical fixed-free beam with pre-stress and curvature arising from gravity. For this structure, it was determined that nonlinear curvature had a strong influence on the response of the first mode of vibration, while inertia nonlinearities dominated the response of the second mode. Using a similar experimental structure, Anderson, Nayfeh, and Balachandran (1996) studied the effects of high-frequency modes on the response of the first mode of vibration. In their work, the analytically predicted response obtained by the method of averaging was in good agreement with experimental results.

In the prior studies (Nayfeh and Kreider, 1995; Kreider and Nayfeh, 1998; Lacarbonara, Nayfeh, and Kreider, 1998; Nayfeh and Emam, 2008; Li and Balachandran, 2006; Li, Preidikman, Balachandran, and Mote, 2006; Anderson, Nayfeh, and Balachandran, 1996), the different authors considered relatively small static deformations in comparison with the length of the beam. The studies of Lacarbonara, Paolone, and Yabuno (2004) and Addessi, Lacarbonara, and Paolone (2005) were concerned with modeling the dynamics of beams with large initial static displace-

ments. Lacarbonara, Paolone, and Yabuno (2004) outlined a geometrically exact formulation to model beams with large deformations with the intent of using perturbation techniques to analyze the dynamic problem. Addressi, Lacarbonara, and Paolone (2005) determined the natural frequencies and mode shapes of a highly curved beam with hinged-hinged boundary conditions and a prescribed force on one end by using a combined analytical and numerical approach. Their predictions were found to be in agreement with a finite element formulation. Addressi *et al.* (Addressi, Lacarbonara, and Paolone, 2005) considered special boundary conditions, which limit configurations that the beam may exhibit. Within this work, both end positions of the beam are prescribed, which allows the beam to deform to a broader class of static configurations. For the configurations considered within this dissertation, the beams are able to undergo large deformations with variable curvature.

1.3 Scope and dissertation objectives

Within this dissertation, the dynamic response of slender structures is studied experimentally, numerically, and analytically. Particular attention is given to the response of torsional vibrations in slender rotors subject to stator force-interactions. The coupled lateral-torsional response is studied for two different systems, namely a lumped-parameter Jeffcott rotor and a distributed-parameter rotor model. The modified Jeffcott model serves to illustrate nonlinear behavior that may exist in even simple rotor-stator systems, while the distributed-parameter model has been derived with the intent of capturing the dynamics observed in an experimental arrangement.

Objectives related to slender rotors with stator force-interactions are as follows:

- Study the response of the torsional vibrations for a Jeffcott rotor-stator system during forward whirling with stator contact (line segment AB in Figure 1.3) and dry-friction whirling (line segment CD in Figure 1.3)
- Design and create an experimental apparatus used to study the dynamics of slender rotor systems with stator contact
- Develop reduced-order models that are able to capture and explain the origins of the phenomena observed in the experiment

In addition to the coupling between torsional and lateral motions, the influence of pre-stress and large curvature on the natural frequencies and mode shapes of slender structures are also addressed within this dissertation. Objectives related to the modal analysis of slender structures are listed below.

- Develop a theoretical framework to predict the natural frequencies and mode shapes of slender structure with large curvature and pre-stress
- Validate model predictions with an experimental apparatus

1.4 Organization of dissertation

The organization of this dissertation is as follows. In Chapter 2, the torsion response of the modified Jeffcott rotor with stator force-interactions is studied for the forward whirling and backward whirling solutions with continuous stator contact.

A rotor-stator experimental arrangement is presented in Chapter 3, and typical phenomena observed in this experiment are discussed. A distributed-parameter rotor model is used to model the dynamics and phenomena seen in the experiment. Again, the special case of forward and backward whirling with continuous stator contact is investigated. In Chapter 4, the dynamics of slender structures are further explored, by developing a geometrically exact beam formulation that is used to predict the mode shapes and natural frequencies of beams with initial pre-stress and large curvature. The modeling and analytical work is validated with an experimental apparatus. In the last chapter, contributions from this dissertation are highlighted, and open areas of research yet to be addressed and future studies are discussed. Appendices which provide further information and work related to this dissertation are included after the last chapter.

Chapter 2

Torsional Motions of the Jeffcott Rotor with Continuous Stator

Contact

As previously discussed, different motions (e.g., lateral, torsional, and axial) can be strongly coupled in slender structures with large aspect ratios. In this chapter, the coupling between lateral and torsional motions is numerically and analytically studied for a modified version of the classical Jeffcott rotor (Jeffcott, 1919). This reduced-order rotor model is subject to stator force-interactions and is capable of torsional deformations. Within this chapter, the torsional motions of this rotor-stator system are investigated while the rotor whirls with continuous stator contact. Approximate equations to the torsion response are derived for forward and backward whirling motions. The modeling and analysis in this chapter serve to identify and explain phenomena that are observed in rotor-stator systems with torsional vibrations. Much of the work contained within this section was originally presented in the work of Vlajic, Liu, Karki, and Balachandran (2013).

2.1 Jeffcott model and governing equations

2.1.1 Derivation of equations of motion

A schematic of the Jeffcott rotor-stator system capable of torsional vibrations is shown in Figure 2.1(a). The rotor with radius R and mass M coincides with the center of the stator with a clearance δ in the static configuration. The rotor has a mass imbalance m with eccentricity e . The quantity J_o is the mass moment of inertia of the rotor without mass imbalance about the z -axis. The rotor is assumed to be symmetrical so that the lateral stiffnesses have equivalent spring constants $k_x = k_y = k_b$, and has a torsional stiffness k . Similarly, the rotor has lateral damping that is assumed to be symmetric such that the equivalent damping coefficients are $c_x = c_y = c_b$. Torsional motions also have dissipation denoted by the damping coefficient c . A schematic of the rotor in a dynamic state at an instant of time is depicted in Figure 2.1(b). The geometric center of the planar rotor is fully described in an inertial frame with coordinates x and y projected onto orthogonal unit vectors \mathbf{a}_1 and \mathbf{a}_2 , respectively. Further, two sets of unit vectors, namely $\mathbf{b}_1, \mathbf{b}_2$ and $\mathbf{c}_1, \mathbf{c}_2$, are placed at the geometric center of the rotor. The $\mathbf{b}_1, \mathbf{b}_2$ reference frame rotates at a constant angular speed Ω with respect to the $\mathbf{a}_1, \mathbf{a}_2$ reference frame. Thus, the angle between \mathbf{a}_1 and \mathbf{b}_1 is a measure of the rigid body rotation Ωt . The mutually orthogonal unit vectors \mathbf{c}_1 and \mathbf{c}_2 are fixed to the rotor, and the angle between \mathbf{b}_1 and \mathbf{c}_1 is the torsional deformation given by θ . For notational convenience, let $\beta(t) \equiv \beta = \theta(t) + \Omega t$, which represents the superposition of the torsional deformation and rigid body rotation. Physically, the torsional stiffness k and damping c act to

align the $\mathbf{b}_1, \mathbf{b}_2$ and $\mathbf{c}_1, \mathbf{c}_2$ unit vectors. Additionally, the rotor is only able to undergo planar motions with no gyroscopic effects due to rotations about the x and y axes; a constraint imposed as $\mathbf{a}_3 \equiv \mathbf{b}_3 \equiv \mathbf{c}_3$ for all time t , where $\mathbf{a}_3 \equiv \mathbf{a}_1 \times \mathbf{a}_2$, $\mathbf{b}_3 \equiv \mathbf{b}_1 \times \mathbf{b}_2$ and $\mathbf{c}_3 \equiv \mathbf{c}_1 \times \mathbf{c}_2$. For convenience, at time $t = 0$, $\mathbf{a}_1 \equiv \mathbf{b}_1 \equiv \mathbf{c}_1$, $\mathbf{a}_2 \equiv \mathbf{b}_2 \equiv \mathbf{c}_2$ and the mass imbalance m is located along the x -axis. With this kinematic description, the kinetic energy is written

$$T = \frac{M}{2}(\dot{x}^2 + \dot{y}^2) + \frac{J_o}{2}\dot{\beta}^2 + \frac{m}{2} \left[(\dot{x} - e\dot{\beta} \sin \beta)^2 + (\dot{y} + e\dot{\beta} \cos \beta)^2 \right] \quad (2.1)$$

The overdots denote derivatives with respect to time. With gravity acting normal to the xy plane, the potential energy of the system is

$$V = \frac{1}{2} [k_b x^2 + k_b y^2 + k\theta^2] \quad (2.2)$$

Rayleigh's dissipation function is expressed in the following form

$$D = \frac{1}{2} [c_b \dot{x}^2 + c_b \dot{y}^2 + c\dot{\theta}^2] \quad (2.3)$$

Lagrange's equations are used to derive the governing equations of motion, which are given to be

$$(M + m)\ddot{x} + c_b \dot{x} + k_b x = me \left[\ddot{\beta} \sin(\beta) + \dot{\beta}^2 \cos(\beta) \right] + F_x \quad (2.4a)$$

$$(M + m)\ddot{y} + c_b \dot{y} + k_b y = me \left[-\ddot{\beta} \cos(\beta) + \dot{\beta}^2 \sin(\beta) \right] + F_y \quad (2.4b)$$

$$J\ddot{\theta} + c\dot{\theta} + k\theta = me [\ddot{x} \sin(\beta) - \ddot{y} \cos(\beta)] + M_t \quad (2.4c)$$

In equation (2.4c), the quantity J is the total rotary inertia of the rotor and mass imbalance about the z -axis, which is given by $J = J_o + me^2$. From the structure

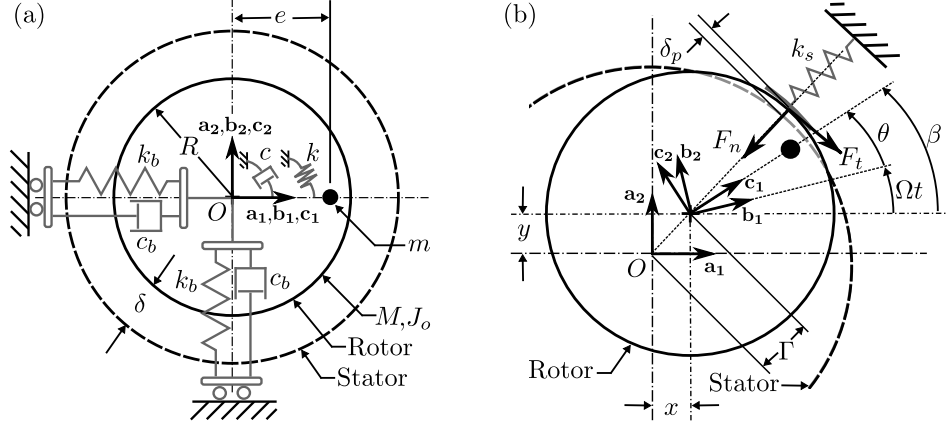


Figure 2.1: (a) Static configuration of the rotor within the stator. (b) Rotor system in a dynamic state.

of equations (2.4a), (2.4b) and (2.4c), the torsional and lateral vibrations are coupled by the eccentricity of the unbalanced mass through the inertial terms. In practice, the mass imbalance and the eccentricity are both small quantities, and this will be taken into account in further sections. The forces F_x and F_y as well as the moment M_t arise from contact with the stator and explicit forms of these quantities are given in the next section.

2.1.2 External stator forces and friction

Upon contact with the stator, the rotor is subject to a normal force that is linearly proportional to the deflection of the stator with stiffness k_s . This may be written as

$$F_n = \begin{cases} 0 & \text{for } \Gamma \leq \delta \\ k_s(\Gamma - \delta) & \text{for } \Gamma > \delta \end{cases} \quad (2.5)$$

where

$$\Gamma(x, y) \equiv \Gamma = \sqrt{x^2 + y^2} \quad (2.6)$$

The tangential force component is governed by both the normal force and friction coefficient μ and is given by

$$F_t = -\mu F_n \quad (2.7)$$

The tangential and normal forces may be transformed to accommodate the external forces and moments in equations (2.4a)-(2.4c) by using the following geometric relations

$$F_x = \frac{-F_t y - F_n x}{\Gamma}, \quad F_y = \frac{F_t x - F_n y}{\Gamma}, \quad M_t = F_t R \quad \text{for } \Gamma \neq 0 \quad (2.8)$$

Several models may be used to capture the frictional force between the rotor and the stator, see for example, Leine and Nijmeijer (2004) or Thomsen (2003). In the current study, friction is modeled as

$$\begin{aligned} \mu(v_{rel}) &= \mu_s \text{sgn}(v_{rel}) - \frac{3}{2}(\mu_s - \mu_m) \left(\frac{v_{rel}}{v_m} - \frac{1}{3} \left(\frac{v_{rel}}{v_m} \right)^3 \right) \\ &= \mu_s \text{sgn}(v_{rel}) - \mu_1 v_{rel} + \mu_3 v_{rel}^3 \end{aligned} \quad (2.9)$$

where μ_s is the static coefficient of friction when the relative speed v_{rel} is zero, and μ_m is the minimum coefficient of friction which occurs at a relative speed of $v_{rel} = v_m$. The coefficients μ_1 and μ_3 take the form

$$\mu_1 = \frac{3}{2} \frac{\mu_s - \mu_m}{v_m}, \quad \mu_3 = \frac{1}{2} \frac{\mu_s - \mu_m}{v_m^3} \quad (2.10)$$

The relative speed between the two surfaces at the point of contact is given by

$$v_{rel} = (\Omega + \dot{\theta})R - \dot{x} \frac{y}{\Gamma} + \dot{y} \frac{x}{\Gamma} \quad \text{for } \Gamma \neq 0 \quad (2.11)$$

The friction model given by equation (2.9) was chosen because it qualitatively captures the behavior of most macroscopic-scale friction models in certain ranges of

relative speeds. For instance, it accounts for the discontinuity at $v_{rel} = 0$ and it has two different values of friction to account for the change in static and dynamic (or kinematic) friction. Furthermore, a Taylor Series expansion of more complex macroscopic-scale friction models (around a point away from $v_{rel} = 0$) will yield a similar polynomial form as that of equation (2.9). Although the coefficients may differ between various models, the series expansions will be topologically similar. Thus, equation (2.9) is sufficient enough to qualitatively capture the features of friction at the macroscopic length scale. Equation (2.9) is a set-valued function due to the signum function. When the relative speed is zero, μ returns a set of values expressed as $\mu^\pm \equiv \mu(0) \in (-\mu_s, \mu_s)$, where μ_s is the static coefficient of friction. Here, the superscript plus minus $(\cdot)^\pm$ denotes a set of values rather than a single, scalar value. The graph of equation (2.9) is provided in Figure 2.2(a) for $v_m = 0.30$, $\mu_m = 0.05$, and $\mu_s = 1.1\mu_m$. The minimum friction coefficient μ_m occurs at the minimum relative speed v_m . For illustration purposes, equation (2.9) is graphed in Figure 2.2(b) for various values of v_m . The signum function in equation (2.9), poses difficulties when numerically integrating the system of equations. Therefore, when performing numerical simulations, equation (2.9) is replaced with

$$\mu(v_{rel}) = \mu_s \frac{2}{\pi} \arctan(\delta_f v_{rel}) - \frac{3}{2}(\mu_s - \mu_m) \left(\frac{v_{rel}}{v_m} - \frac{1}{3} \left(\frac{v_{rel}}{v_m} \right)^3 \right) \quad (2.12)$$

In equation (2.12), the normalized arctangent function closely approximates the signum function for $\delta_f \gg 1$. For the remainder of this work, equation (2.9) is used in the analyses, while equation (2.12) is used in the corresponding numerical simulations.

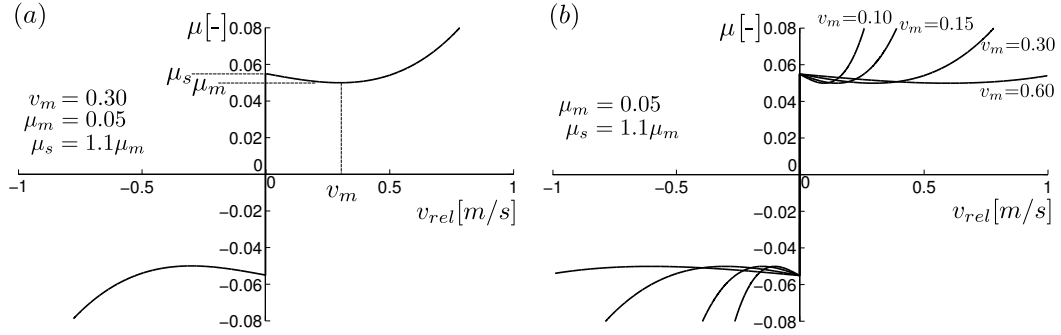


Figure 2.2: (a) Illustration for defining parameters used in the friction coefficient. (b) Graphical depiction of change in friction coefficient for different values of v_m .

Table 2.1: Parameter values used in simulations

Parameter	Value	Units
ζ_b (c_b)	0.01 (0.02)	$N \cdot s/m$
ζ (c)	0.01 ($1.83 e^{-4}$)	$N \cdot m \cdot s/rad$
e	0.05	m
M	1	kg
m	0.05	kg
k_b	1	N/m
k_s	$1e^4$	N/m
k	0.05	$N \cdot m/rad$
R	0.05	m
v_m	0.05-0.25	m/s
δ	0.01	m
δ_f	$1e^6$	-
μ_s	$1.05 \mu_m$	-
μ_m	0.005-0.1	-

2.2 Characteristic whirl phenomena

Equations (2.4a)-(2.8) and (2.12) are numerically integrated by using a modified Rosenbrock scheme, which is better suited to handle stiff systems. Simulations were also conducted by using a fourth order Runge-Kutta method with absolute and relative tolerances of $1e^{-6}$, with no discernible differences between the two schemes. The steady-state, non-dimensional whirling amplitude Γ/δ is plotted in Figure 2.3 as a function of drive speed for the parameters given in Table 2.1. In the simulations, rather than selecting the damping coefficients c_b and c , it is convenient to specify the damping ratios for the lateral and torsional motions, which are defined as $\zeta_b \equiv \frac{c_b}{2\sqrt{(M+m)k_b}}$ and $\zeta \equiv \frac{c}{2\sqrt{Jk}}$, respectively. In Figure 2.3, the rotor makes contact with the stator when $\Gamma/\delta = 1$. Solid lines correspond to forward whirling of the rotor while dashed lines indicate backward whirling rotor motions. The initial conditions determine which branch of the stable solution the system will reach. It is noted that there are two stable forward whirling solutions above the first natural frequency. Starting at a low drive speed near $\Omega = 0$ and sweeping up in the drive speed, the rotor will make contact with the stator and remain in contact with the stator while the driving speed is increased. For both the backward and forward whirling solutions with stator contact in Figure 2.3, the rotor will break contact with the stator. Approximate equations when the rotor breaks contact with the stator have been derived in Bartha (2000) and Childs (1993). Once the rotor breaks contact with the stator at a large Ω , the drive speed may be quasi-statically lowered back to zero and the lateral motions of the rotor will trace out the bottom branch

of the forward whirling solution. It has been determined both numerically and experimentally that the following whirl frequency relations hold for a range of drive speeds (Vlajic, Liao, Karki, and Balachandran, 2012).

$$\omega_{for} \approx \Omega, \quad \omega_{back} \approx -\Omega \frac{R}{\delta} \quad (2.13)$$

The forward whirling frequency, denoted ω_{for} is approximately equal to the prescribed angular speed of the rotor and the whirl motion is in the direction of motor rotation. On the other hand, the backward whirling frequency ω_{back} is of a faster rate than the motor rotation speed for $\delta < R$ and the whirling is in the opposite direction of motor rotation, which is represented by the negative sign in equation (2.13). Additionally, the backward whirling frequency relation only holds for a range of operating speeds. As the speed is increased the backward whirling speed saturates and the rotor is said to be in the *whipping region*. The remainder of this work is focused on examining the response of torsional vibrations during both forward and backward whirling motions.

2.3 Simplification of the governing equations

2.3.1 Reduction of structural terms

In this section, the system of equations given by equations (2.4a)-(2.4c) are reduced to a single equation which will be analyzed in subsequent sections to explain phenomena observed in numerical simulations of equations (2.4a)-(2.8) and (2.12).

When the rotor maintains contact with the stator while whirling at a constant rate,

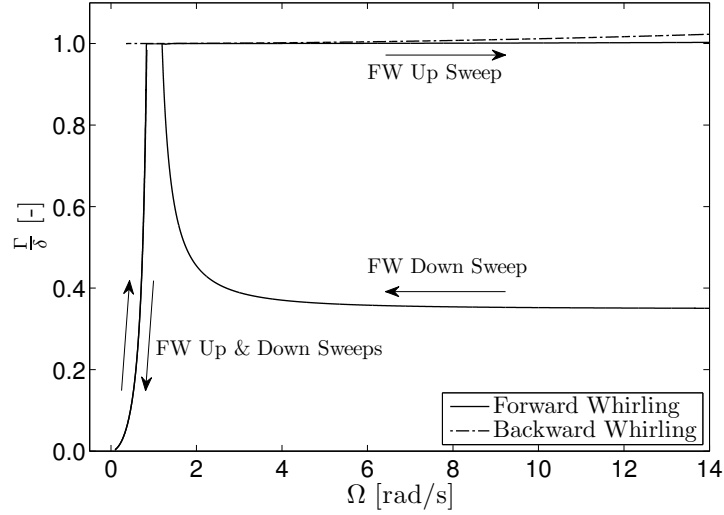


Figure 2.3: Numerically generated solutions for stable responses of the system given by equations (2.4a)-(2.8) and (2.12).

the corresponding x and y displacements may be prescribed as:

$$x(t) = (\delta + \delta_p) \cos(\omega t + \phi_o) \approx \delta \cos \omega t \quad (2.14a)$$

$$y(t) = (\delta + \delta_p) \sin(\omega t + \phi_o) \approx \delta \sin \omega t \quad (2.14b)$$

In equations (2.14), the quantity $\delta_p = \Gamma - \delta$ is the deflection of the stator, or similarly, the penetration depth of the rotor into the stator, and this quantity is assumed to be much smaller than the initial clearance; that is, $\delta \gg \delta_p$ and $\delta_p \approx 0$. The quantity ω is termed the *whirl frequency* and ϕ_o is the phase angle. For the following analysis, ϕ_o is set equal to zero for convenience. When $\omega > 0$, the rotor is whirling in the direction of motor rotation (forward whirling), and when $\omega < 0$, the rotor motion is in the opposite direction of motor rotation (backward whirling). Furthermore, for most rotor systems, the amplitude of torsional vibrations are small, so that $\sin \theta$ and $\cos \theta$ may be approximated by the first term of their respective Taylor Series expansions. The relative error is less than 1% for $\sin \theta \approx \theta$ and approximately

1.51% for $\cos \theta \approx 1$ for an angular displacement of 10° – a reasonable amplitude of torsional vibrations in most rotating equipment. Under this assumption, the following relations are used

$$\begin{aligned}\sin(\beta(t)) &= \sin(\theta(t) + \Omega t) = \sin \theta(t) \cos \Omega t + \cos \theta(t) \sin \Omega t \\ &\approx \theta(t) \cos \Omega t + \sin \Omega t\end{aligned}\tag{2.15}$$

$$\begin{aligned}\cos(\beta(t)) &= \cos(\theta(t) + \Omega t) = \cos \theta(t) \cos \Omega t - \sin \theta(t) \sin \Omega t \\ &\approx \cos \Omega t - \theta(t) \sin \Omega t\end{aligned}\tag{2.16}$$

Equations (2.14), (2.15), and (2.16) are substituted into (2.4c) in order to obtain the following simplified equation for torsional motions while the rotor is whirling with a constant frequency and amplitude

$$J\ddot{\theta} + c\dot{\theta} + [k + \delta m e \omega^2 \cos((\omega - \Omega)t)] \theta = \delta m e \omega^2 \sin((\omega - \Omega)t) + M_t\tag{2.17}$$

If the external moment is linear with respect to θ and $\dot{\theta}$, then equation (2.17) is linear with periodic coefficients and external forcing. This equation falls into the general class of equations known as the Mathieu-Hill equations, and the solution stability may be determined by using Floquet theory or Hill's Infinite Determinant (e.g., Nayfeh and Mook (1979) and Nayfeh and Balachandran (1995)).

2.3.2 Approximation of external forces and contact

Given the assumptions in equation (2.14) and using equation (2.5), the normal force is zero. However, when $k_s \gg k_b$, a force balance is used to determine the normal

force in terms of the reactive force. This is given by

$$F_n \approx [\delta M + (\delta + e \cos \phi_{ubm})m] \omega^2 - k_b \delta \quad (2.18)$$

In equation (2.18), the angle ϕ_{ubm} is the location of the unbalanced mass with respect to the radial position vector of the rotor. During forward, synchronous whirling ϕ_{ubm} , is constant for a fixed drive speed. During constant backward whirling, the phase grows linearly in time and the mass imbalance creates a periodic component in the normal force. If the rotor mass and the clearance are much larger than the unbalance mass and eccentricity $\delta(M + m) > me$, the approximated equivalent of equation (2.18) for both forward and backward whirling take the form

$$F_n = (M + m)\delta\omega^2 - k_b\delta \quad (2.19)$$

The first driving speed at which the rotor makes contact with the stator during forward whirling (or breaks contact in the case of backward whirling), Ω_c is termed the *contact frequency* and can be approximated by determining the frequency at which the normal force becomes zero; that is, $F_n|_{\Omega=\Omega_c} = 0$. With this definition and the whirl relations given by equation (2.13), the contact frequencies for forward and backward whirling are expressed as

$$\Omega_{c,for} = \sqrt{\frac{k_b}{M + m}}, \quad \Omega_{c,back} = \frac{\delta}{R} \sqrt{\frac{k_b}{M + m}} \quad (2.20)$$

Similar contact conditions during backward whirling have been derived by Bartha (2000). It is important to point out that equation (2.19) is an under approximation of the actual normal given by equation (2.5) during forward whirling, which generally has a higher magnitude. Additionally, equation (2.19) is a simplification of

the normal force during backward whirling, since the periodic component has been neglected. Likewise, equations (2.20) are to be considered approximate speeds when the rotor makes or breaks contact with the stator, and serve only to indicate when equation (2.17) is valid, namely, when $\Omega > \Omega_c$. In practice, the normal force and contact speeds are dependent upon the lateral damping and the phase angle.

2.3.3 Non-dimensionalization

With the transformation $t = \omega_o \tau$, where τ represents dimensionless time and $\omega_o = \sqrt{k/J}$ is the linear natural frequency in torsion, equation (2.17) may be rewritten in terms of non-dimensional parameters as

$$\ddot{\theta} + 2\zeta\dot{\theta} + [1 + \tilde{m}\tilde{\omega}^2 \cos(\tilde{\alpha}\tau)] \theta = \tilde{m}\tilde{\omega}^2 \sin(\tilde{\alpha}\tau) + \tilde{M}_t$$

In equation (2.21) and in the remainder of this work, overdots represent derivatives with respect to τ and the following non-dimensional parameters have been introduced:

$$\begin{aligned} \tilde{m} &\equiv \frac{\delta m e}{J}, \quad \tilde{\omega} \equiv \frac{\omega}{\omega_o}, \quad \tilde{\alpha} \equiv \frac{\omega - \Omega}{\omega_o}, \quad \tilde{\Omega} \equiv \frac{\Omega}{\omega_o}, \\ 2\zeta &\equiv \frac{c}{\sqrt{Jk}}, \quad \tilde{c} \equiv \frac{\delta + R}{R}, \quad \tilde{M}_t \equiv \frac{M_t}{J\omega_o^2} = -\tilde{N}\mu(\tilde{v}_{rel}) \end{aligned} \quad (2.21)$$

In the last of equations (2.21), the quantity \tilde{N} is proportional to normal force (physically it is the normal force multiplied by the radius of the rotor) and is written

$$\tilde{N} \equiv \frac{F_n}{J\omega_o^2} = (\tilde{n}_1\tilde{\omega}^2 - \tilde{n}_2) \quad (2.22)$$

where

$$\tilde{n}_1 = \frac{R\delta(M+m)}{J}, \quad \tilde{n}_2 = \frac{k_b\delta R}{J\omega_o^2} \quad (2.23)$$

Similarly, the relative speed is non-dimensionalized by $\tilde{v}_{rel} = v_{rel}/(\omega_o R)$. Additionally, the two friction coefficients in equation (2.9) are also non-dimensionalized provided the relative speed is non-dimensionalized, and they are denoted as $\tilde{\mu}_1$ and $\tilde{\mu}_3$. The term \tilde{m} is referred to as the mass ratio in this work, and is a measure of the gap distance, unbalance, and eccentricity to the rotary inertia of the rotor. The quantities $\tilde{\Omega}$ and $\tilde{\omega}$ are the non-dimensional drive frequency and whirl frequency, respectively. The term $\tilde{\alpha}$ is the non-dimensional whirl ratio, which takes on values less than zero for backward whirling and equal to zero for synchronous forward whirling. The parameter \tilde{c} is the clearance ratio and gives a measure of the rotor radius to clearance.

2.4 Torsion response during forward whirling motions

When undergoing forward, synchronous whirling, the whirl frequency is approximately equal to the drive frequency ($\tilde{\omega} \approx \tilde{\Omega}$) and equation (2.21) becomes autonomous and reduces to

$$\ddot{\theta} + 2\zeta\dot{\theta} + [1 + \tilde{m}\tilde{\omega}^2] \theta = -(\tilde{n}_1\tilde{\omega}^2 - \tilde{n}_2) \mu(\tilde{v}_{rel}) \quad (2.24)$$

It is understood that throughout the rest of the work equation (2.24) is only valid for $\omega = \Omega > \Omega_{c,for}$ in order to ensure contact between the rotor and stator as prescribed by the original assumptions. Equation (2.24) has features similar to that

of the classic stick-slip problem, which is generally illustrated by a mass-spring-damper system on a drive belt with dry-friction, with the exception of two notable differences. Namely, the system at hand has a centrifugal stiffening effect, and the normal force is quadratic in the whirl frequency. Likewise, the relative speed for forward whirling reduces to

$$\begin{aligned}\tilde{v}_{rel} &= \tilde{\omega}\tilde{c} + \dot{\theta} \\ &= \tilde{v}_w + \dot{\theta}\end{aligned}\tag{2.25}$$

The term \tilde{v}_w in equation (2.25) is referred as the *whirl speed* in this work. While undergoing forward whirling motions, the relative speed between the rotor and the stator is greater than zero and is away from the signum function in equation (2.9). Therefore, for forward whirling, the signum function in equation (2.9) is always positive, and it is assumed that the relative speed does not reach zero; that is, $\tilde{v}_w > -\dot{\theta}$. The equilibrium of the torsional displacement is found by setting the time derivatives equal to zero in equation (2.24), which for this case yields

$$\begin{aligned}\dot{\theta}_{eq} &= 0 \\ \theta_{eq} &= -\frac{(\tilde{n}_1\tilde{\omega}^2 - \tilde{n}_2)\mu(\tilde{v}_w)}{1 + \tilde{m}\tilde{\omega}^2}\end{aligned}\tag{2.26}$$

The transformation $u(t) \equiv u = \theta + \theta_{eq}$ is used to shift the origin of u to be centered at the equilibrium θ_{eq} . Equation (2.24) is transformed to be

$$\ddot{u} + [1 + \tilde{m}\tilde{\omega}^2]u + \epsilon\hat{F}(\dot{u}) = 0\tag{2.27}$$

where $F(\dot{u}) = \epsilon\hat{F}(\dot{u})$ and $F(\dot{u})$ is given by

$$F(\dot{u}) = 2\zeta\dot{u} + (\tilde{n}_1\tilde{\omega}^2 - \tilde{n}_2)[\mu(\tilde{v}_w + \dot{u}) - \mu(\tilde{v}_w)]\tag{2.28}$$

The nondimensional parameter ϵ has been introduced as a scaling parameter to indicate that the friction quantity is small compared to the other terms in equation (2.27). For the analytical considerations, $0 < \epsilon \ll 1$ and it follows that $\hat{F}(\dot{u}) = \mathcal{O}(1)$ and $F(\dot{u}) = \epsilon \hat{F}(\dot{u}) = \mathcal{O}(\epsilon)$. The relative strengths of the different magnitudes approximately hold for Table 2.1 values and whirl speeds in the range $\tilde{\omega} \in (1, 5)$. A Taylor series expansion is used to expand equation (2.28) to obtain the approximate polynomial for the analyses.

$$F(\dot{u}) \approx f_0 + f_1 \dot{u} \quad (2.29)$$

The coefficients in equation (2.29) are given by

$$\begin{aligned} f_0 &= 0 \\ f_1 &= 2\zeta - \tilde{\mu}_1(\tilde{n}_1\tilde{\omega}^2 - \tilde{n}_2) \left(1 - \left(\frac{\tilde{v}_w}{\tilde{v}_m} \right)^2 \right) \end{aligned} \quad (2.30)$$

The fixed points given by equation (2.26) may be stable or can lose stability through a Hopf bifurcation. In the absence of structural damping ($\zeta = 0$), the equilibrium will be unstable if $v_{c,\text{for}} < v_w < v_m$, where $v_{c,\text{for}} = (R + \delta)\Omega_{c,\text{for}}$ is the relative speed when the rotor first makes contact with the stator. According to this, the whirl speed of the rotor must be greater than the contact speed, but less than the minimum velocity which defines the coefficient of friction profile. In the presence of damping, a Hopf instability can occur if $f_1 < 0$. In practice the relative speed at first contact is likely to be larger than the minimum velocity (i.e., $v_{c,\text{for}} > v_m$), which is typically a small value. Consequently, during forward, synchronous whirling, the frictional force effectively results in additional damping and oscillations asymptotically decay to zero in time. For illustrative purposes, the equilibrium and the nature of its

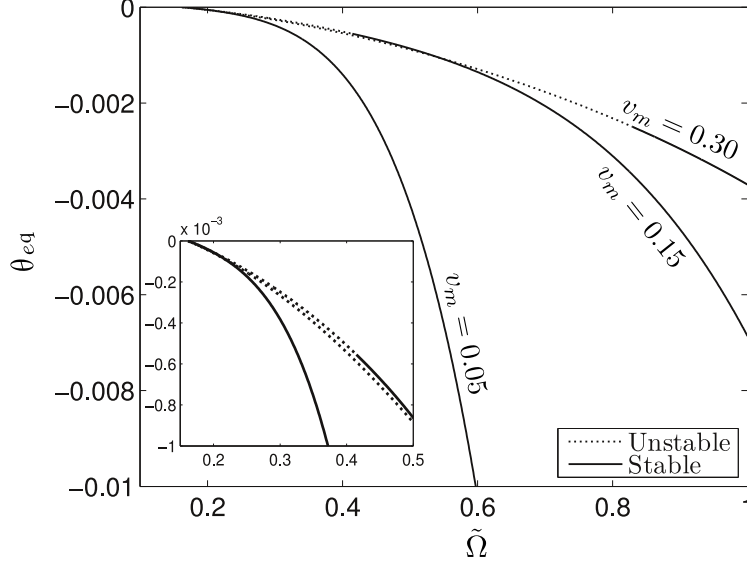


Figure 2.4: Stability dependence on the friction parameter v_m when the damping ratio is set to $\zeta = 0.01$. Dotted lines represent unstable solutions while solid lines represent stable solutions for the equilibrium position θ_{eq} .

stability are plotted in Figure 2.4 for $\zeta = 0.01$ and different values of the minimum relative speed v_m .

As the damping is increased, the point that transitions from stable to unstable oscillations moves toward the left. This is found by determining the zeros of the term f_1 , as illustrated in Figure 2.5. As ζ is increased, the region of stability is increased until the term f_1 no longer has any zeros. Upon which, the entire equilibrium solution becomes stable. The onset of this condition occurs when f_1 no longer has any real valued roots, and is found to be

$$2\zeta > \tilde{\mu}_1(\tilde{n}_1\tilde{\omega}^2 - \tilde{n}_2) \left(1 - \left(\frac{\tilde{v}_w}{\tilde{v}_m} \right)^2 \right) \quad (2.31)$$

Numerical simulations of the full system, given by equations (2.4a)-(2.8) and (2.12), indicate that if equation (2.31) is not satisfied, then the amplitude of tor-

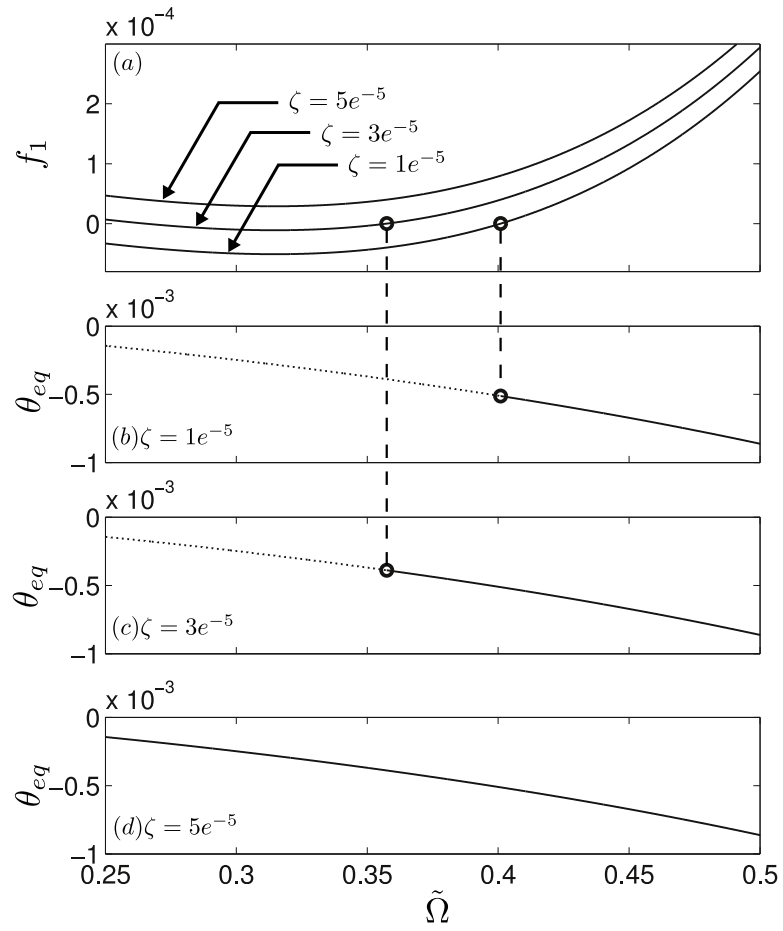


Figure 2.5: Stability dependence on structural damping ζ . Dotted lines represent unstable solutions while solid lines represent stable solutions for the equilibrium position θ_{eq} for $v_m = 0.3$.

sional vibrations becomes large and the rotor will either lose contact with the stator, or it will remain in contact with the stator and no longer whirl at a constant rate. Comparisons between the full model and reduced-order model, subject to a perturbation of $\theta_o = 0.05$ for four different cases are provided in Figure 2.6 for a drive speed of $\Omega = 4.0$ rad/s. In cases (a) and (b), the minimum friction is set for $v_m = 0.15$ m/s, which is less than the average relative speed between the rotor and stator $v_{rel} = (R + \delta)\Omega = 0.24$ m/s. During case (a), with the damping ratio $\zeta = 0.01$, the initial perturbation of $\theta_o = 0.05$ decays exponentially with time. Similarly in case (b) when the damping ratio is set to $\zeta = 0.0$, the perturbation still asymptotically decays, and the system returns to the equilibrium position, however, at a much slower rate. In cases (c) and (d), the minimum velocity was equal to $v_m = 0.3$, which is higher than the relative velocity v_{rel} . During case (c), the damping ratio is set to $\zeta = 0.01$, and again the perturbation decays asymptotically back to the equilibrium position. On the other hand, when the damping ratio is set $\zeta = 0.0$, as in case (d), the perturbation in both the full model and the reduced-order model start to grow. For the parameter values used in cases (a) – (c), the criterion for stability given by equation (2.31) holds, whereas the equation (2.31) is not satisfied for the parameters used in case (d).

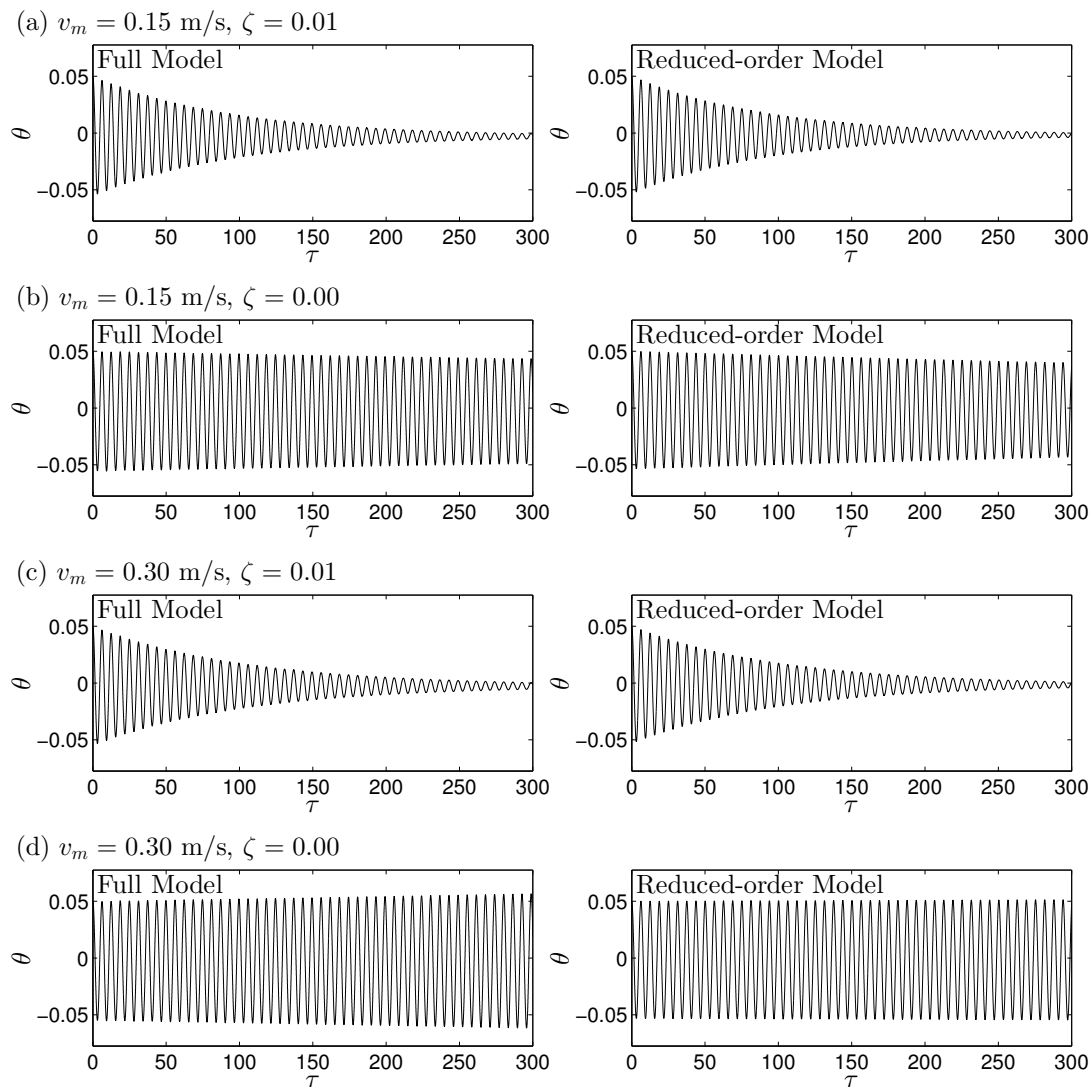


Figure 2.6: Comparisons of the results from the full system (equations (2.4a)-(2.8) and (2.12)) and the reduced-order system (equations (2.24) and (2.12)) at $\Omega = 4.0$ rad/s. Perturbations decay in cases (a)-(c) and grow in case (d). (a) Whirl speed is greater than the minimum friction speed ($v_w > v_m$) in the presence of structural damping, (b) whirl speed is greater than the minimum friction speed ($v_w > v_m$) even without structural damping ($\zeta = 0$), (c) whirl speed is less than the minimum friction speed ($v_w < v_m$) in the presence of structural damping, and (d) whirl speed is less than the minimum friction speed ($v_w < v_m$) in the absence damping ($\zeta = 0$).

2.5 Torsion response during backward whirling motions

2.5.1 Governing equation and equilibrium

While undergoing backward, dry-friction whirling, the whirl speed of the rotor may be expressed in terms of system parameters as $\omega \approx -\frac{R}{\delta}\Omega$, which is derived under the assumption of the no-slip condition; that is, the relative speed between the rotor and stator is zero in the absence of torsional vibrations. By using this relationship, the non-dimensional whirl frequency, whirl ratio and relative speed are found to be

$$\tilde{\omega} = -\frac{R}{\delta}\tilde{\Omega}, \quad \tilde{\alpha} = -\tilde{\Omega} \left(\frac{R}{\delta} + 1 \right), \quad \tilde{v}_{rel} = \dot{\theta} \quad (2.32)$$

Again, the negative signs in equation (2.32) indicate that the whirl direction of the rotor is in the opposite direct of the driving rotation. With the above relations, equation (2.21) reduces to equation (2.33).

$$\ddot{\theta} + 2\zeta\dot{\theta} + [1 + \tilde{m}\tilde{\omega}^2 \cos(\tilde{\alpha}\tau)] \theta = \tilde{m}\tilde{\omega}^2 \sin(\tilde{\alpha}\tau) - [\tilde{n}_1\tilde{\omega}^2 - \tilde{n}_2] \mu(\dot{\theta}) \quad (2.33)$$

It is understood that equation (2.33) is valid only while the rotor is in continuous contact with the stator while undergoing backward whirling motions, which is valid for $\Omega > \Omega_{c,back}$. The frequency component $\tilde{\alpha}$ observed in the torsion response is confirmed experimentally in Chapter 3.

Equation (2.33) has a differential inclusion because the friction model is a set-valued function, which returns values $\mu^\pm \equiv \mu(0) \in (-\mu_s, \mu_s)$ at $v_{rel} = 0$. Seeking an equilibrium solution of the form $\dot{\theta} = 0$, $\theta = \theta_{eq}^\pm$ and performing a static force balance, the stable equilibrium set is determined to be $\theta_{eq}^\pm \in (-\theta_{eq}, \theta_{eq})$ where

$$\theta_{eq} = \min \left(\frac{[\tilde{n}_1 \tilde{\omega}^2 - \tilde{n}_2] \mu_s - \tilde{m} \tilde{\omega}^2 \sin \tilde{\alpha} \tau}{1 + \tilde{m} \tilde{\omega}^2 \cos \tilde{\alpha} \tau} \right) \quad \text{for } \tilde{m} \tilde{\omega}^2 \leq [\tilde{n}_1 \tilde{\omega}^2 - \tilde{n}_2] \mu_s \quad (2.34)$$

The boundary of the equilibria set given by equation (2.34) is determined over $0 \leq \alpha\tau < 2\pi$. Considering the limiting case, as $\tilde{m}\tilde{\omega}^2$ approaches $[\tilde{n}_1\tilde{\omega}^2 - \tilde{n}_2]\mu_s$, θ_{eq} approaches zero. If the amplitude of the external forcing is larger than the coefficient of friction (i.e., $\tilde{m}\tilde{\omega}^2 > [\tilde{n}_1\tilde{\omega}^2 - \tilde{n}_2]\mu_s$), then no stable set exists and the system will undergo limit-cycle motions. Two separate cases of low-speed and high-speed backward whirling are considered below.

2.5.2 Low-speed backward whirling

The term “low-speed” backward whirling in this work refers to parameter values that yield the small quantity $\tilde{m}\tilde{\omega}^2 = \mathcal{O}(\epsilon)$, where $\epsilon \ll 1$. Further, if $2\zeta, \tilde{N}\mu_s = \mathcal{O}(\epsilon)$, then equation (2.33) may be rewritten as

$$\ddot{\theta} + \theta + \epsilon \hat{B}_{LS}(\theta, \dot{\theta}, \tau) = 0$$

where $B_{LS} = \epsilon \hat{B}_{LS}$ and

$$B_{LS}(\theta, \dot{\theta}, \tau) = 2\zeta\dot{\theta} + \tilde{m}\tilde{\omega}^2 \cos(\tilde{\alpha}\tau)\theta - \tilde{m}\tilde{\omega}^2 \sin(\tilde{\alpha}\tau) + [\tilde{n}_1\tilde{\omega}^2 - \tilde{n}_2] \mu(\dot{\theta})$$

Again, ϵ is a small positive bookkeeping parameter that indicates the B_{LS} term is of order $\mathcal{O}(\epsilon)$ and is small compared with the other terms in equation (2.35). For the parameters found in Table 2.1, the scaling used in equations (2.35) and (2.35) can be said to hold over $\tilde{\alpha} \in (-0.1, -0.8)$. An approximate solution to equation (2.35) may be constructed by using the Method of Multiple Scales (Nayfeh and Mook,

1979) with independent time scales $T_0 = \tau$ and $T_1 = \epsilon\tau$. An approximate solution is sought of the expanded form

$$\theta = \theta_0(T_0, T_1) + \epsilon\theta_1(T_0, T_1) + \dots \quad (2.35)$$

Upon substituting equation (2.35) into equation (2.35) and collecting appropriate terms of ϵ , the $\mathcal{O}(1)$ solution is

$$\theta_0(T_0, T_1) = A(T_0, T_1)e^{jT_0} + A^*(T_0, T_1)e^{-jT_0} \quad (2.36)$$

Here, $A = \frac{1}{2}ae^{jb}$ is a complex function in polar form with $a(T_1), b(T_1) \in \mathbb{R}$, j is the imaginary number, and the superscript star $(\cdot)^*$ denotes the complex conjugate. Invoking the solvability conditions and performing a Fourier Series on the signum function, three separate cases are considered below to ensure the elimination of terms that will result in secular terms of the particular solution of θ_1 .

Off Resonance: $\tilde{\alpha}$ away from $-1, -2$. The slow-time amplitude and phase variation equations are found to be

$$\begin{aligned} \frac{da}{dT_1} &= \left(\frac{\tilde{N}}{2}\tilde{\mu}_1 - \zeta \right) a - \frac{3}{8}\tilde{N}\tilde{\mu}_3a^3 - \frac{2}{\pi}\tilde{N}\mu_s \\ \frac{db}{dT_1} &= 0 \end{aligned} \quad (2.37)$$

where \tilde{N} is given by equation (2.22). The steady-state amplitude and phase of the response θ is determined from the steady-state solution to equation (2.37). The phase is simply a constant b_o whose value is governed by initial conditions. The steady-state amplitude is determined by setting $a' = g(a) = 0$ and determining the zeros of $g(a)$. In general, $g(a)$ may have upto three real valued roots, denoted by

a_j . The stability of the steady-state amplitude is determined by the sign of $\frac{dg}{da}|_{a=a_j}$, where positive values indicate the amplitude solution is unstable and negative values signify the amplitude solution is stable. Further analysis is needed when $\frac{dg}{da}|_{a=a_j} = 0$. *Primary Resonance:* $\tilde{\alpha} \approx -1$. The transformation $\tilde{\alpha} = -1 + \epsilon\sigma$ is introduced, where σ is a detuning parameter that indicates how close $\tilde{\alpha}$ is to -1. Further, with the transformation $\psi = \sigma T_1 + b$, the slow-time variation or modulation equations may be expressed in autonomous form as

$$\begin{aligned} \frac{da}{dT_1} &= \left(\frac{\tilde{N}}{2} \tilde{\mu}_1 - \zeta \right) a - \frac{3}{8} \tilde{N} \tilde{\mu}_3 a^3 - \frac{2}{\pi} \tilde{N} \mu_s - \frac{\tilde{m} \tilde{\omega}^2}{2} \cos \psi \\ a \frac{d\psi}{dT_1} &= a\sigma - \frac{\tilde{m} \tilde{\omega}^2}{2} \sin \psi \end{aligned} \quad (2.38)$$

Parametric Resonance: $\tilde{\alpha} \approx -2$. As before, with the transformations $\tilde{\alpha} = -2 + \epsilon\sigma$ and $\psi = \sigma T_1 + 2b$, the autonomous form of the modulation equations become

$$\begin{aligned} \frac{da}{dT_1} &= \left(\frac{\tilde{N}}{2} \tilde{\mu}_1 - \zeta \right) a - \frac{3}{8} \tilde{N} \tilde{\mu}_3 a^3 - \frac{2}{\pi} \tilde{N} \mu_s - \frac{\tilde{m} \tilde{\omega}^2}{4} a \sin \psi \\ a \frac{d\psi}{dT_1} &= 2a\sigma - \frac{\tilde{m} \tilde{\omega}^2}{2} a \cos \psi \end{aligned} \quad (2.39)$$

Approximate solutions to equations (2.38) and (2.39) may be determined by using perturbation analysis (e.g. Nayfeh and Mook (1979)), but they are not discussed in this work. The special case when $|\tilde{\omega}|, |\tilde{\alpha}| \gg 1$ is examined in detail in the next section.

2.5.3 High-speed backward whirling

In this work, “high-speed” backward whirling refers to instances when the backward whirling frequency is much greater than the first torsional natural fre-

quency; that is, $|\tilde{\omega}|, |\tilde{\alpha}| \gg 1$. This case readily occurs in practice for most rotor systems since the radius of the rotor is generally much larger than the clearance of the stator (i.e., $R \gg \delta$). It is important to point out that $\tilde{\omega} = \mathcal{O}(\tilde{\alpha})$, which is made apparent from equations (2.32). Additionally, as mentioned earlier, the mass and eccentricity are typically small quantities so that $\tilde{m} \ll 1$. If the whirl frequency of the rotor is such that $\tilde{m}\tilde{\omega}, \tilde{m}\tilde{\alpha} = \mathcal{O}(1)$, a range valid for $\tilde{\alpha} \in (-1, -8)$, then equation (2.33) may be written

$$\ddot{\theta} + [1 + (\tilde{m}\tilde{\omega})\tilde{\omega} \cos(\tilde{\alpha}\tau)] \theta + \epsilon \hat{B}_{HS}(\dot{\theta}) = (\tilde{m}\tilde{\omega})\tilde{\omega} \sin(\tilde{\alpha}\tau)$$

where $B_{HS} = \epsilon \hat{B}_{HS}$ and

$$B_{HS}(\dot{\theta}) = 2\zeta\dot{\theta} + [\tilde{n}_1\tilde{\omega}^2 - \tilde{n}_2] \mu(\dot{\theta})$$

The quantity B_{HS} is assumed to be smaller than the other terms in Eq. (2.40), and this is expressed by stating that $B_{HS} = \mathcal{O}(\epsilon)$ with $\hat{B}_{HS} = \mathcal{O}(1)$. An approximate solution to equation (2.40) will be constructed following the Method of Direct Partition of Motions (MDPM) as shown by Blekhman (1976) and used in reference Thomsen (2003). As such, two time scales are introduced, namely a slow scale τ and a fast scale $\tau_1 = \tilde{\alpha}\tau$ where $\tau_1 > \tau$. The torsional amplitude is then decomposed into a superposition of the slow and fast scales as

$$\theta(\tau, \tilde{\alpha}\tau) = z(\tau) + \tilde{\alpha}^{-1}\varphi(\tau, \tilde{\alpha}\tau) \quad (2.40)$$

where z is the slow-scale variable and φ is the fast-scale variable. It is noted that the approximate solution assumed for low-speed backward whirling, given by equation

(2.35), is different than the solution presented in equation (2.40). The expansion assumed while using the Method of Multiple Scales results in fast-scale evolutions with slow-scale modulations in amplitude and phase (equation (2.35)), while the expansion assumed in using the Method of Direct Partition of Motions is a superposition of the slow and fast scales (equation (2.40)) to capture the superposition of the “high-frequency oscillations” on the “slow” evolutions (Thomsen, 2003). The introduction of two scales transforms one unknown θ into two unknowns z and φ . Therefore, an additional constraint is necessary to make the transformation unique. A reasonable constraint is to impose the condition that the average over one period of the fast-scale variation is zero, while the variation on the slow time-scale is constant. This is expressed as

$$\langle \varphi(\tau, \tilde{\alpha}\tau) \rangle = \frac{1}{2\pi} \int_0^{2\pi} \varphi(\tau, \tilde{\alpha}\tau) d(\tilde{\alpha}\tau) = 0 \quad (2.41)$$

The bracket operator, denoted by $\langle \cdot \rangle$, indicates the integration of the argument over one period of the fast scale as defined by equation (2.41). Equation (2.40) is substituted into equation (2.33) and making use of the Chain Rule, the following equation is obtained

$$\begin{aligned} \varphi'' &= -z \frac{\tilde{m}\tilde{\omega}^2}{\tilde{\alpha}} \cos \tilde{\alpha}\tau + \frac{\tilde{m}\tilde{\omega}^2}{\tilde{\alpha}} \sin \tilde{\alpha}\tau \\ &- \frac{1}{\tilde{\alpha}} \left\{ \ddot{z} + 2\dot{\varphi}' + z + 2\zeta(\dot{z} + \varphi') + \frac{\tilde{m}\tilde{\omega}^2}{\tilde{\alpha}} \varphi \cos \tilde{\alpha}\tau + (\tilde{n}_1\tilde{\omega}^2 - \tilde{n}_2)\mu(\dot{z} + \varphi') \right\} + \mathcal{O}(\tilde{\alpha}^{-2}) \end{aligned} \quad (2.42)$$

The dot operation $(\dot{\cdot})$ and the prime operation $(\cdot)'$ denote the derivatives with respect to τ and $\tilde{\alpha}\tau$, respectively. Once the $\mathcal{O}(1)$ equation is obtained, the following

expression for the fast-scale variable is found by recognizing that $\frac{\tilde{m}\tilde{\omega}^2}{\tilde{\alpha}} = \mathcal{O}(1)$.

$$\varphi = z\Delta \cos \tilde{\alpha}\tau - \Delta \sin \tilde{\alpha}\tau + \mathcal{O}(\tilde{\alpha}^{-1}) \quad (2.43)$$

where

$$\Delta = \frac{\tilde{m}\tilde{\omega}^2}{\tilde{\alpha}} = \frac{\tilde{m}\tilde{\alpha}}{(\delta/R + 1)^2} \quad (2.44)$$

Note that the expression for φ satisfies the imposed constraint $\langle \varphi \rangle = 0$ given by equation (2.41). The slow-scale variation has been assumed to be constant while solving for the fast variable. In a similar manner, while solving for slow-scale variable, average values are taken for the fast scale. After substituting the expression for φ and its appropriate derivatives into equation (2.42), performing the necessary average over the fast scale, and neglecting terms of $\mathcal{O}(\tilde{\alpha}^{-2})$ and higher, the following equation governing the slow-scale variable is obtained

$$\ddot{z} + 2\zeta\dot{z} + z + \Delta \langle \varphi \cos \tilde{\alpha}\tau \rangle + (\tilde{n}_1\tilde{\omega}^2 - \tilde{n}_2) \langle \mu(\dot{z} + \varphi') \rangle = 0 \quad (2.45)$$

Initial conditions for equation (2.45), are found by using equations (2.40) and (2.43).

They are given by

$$z_o = \frac{\theta_o}{1 + \Delta/\tilde{\alpha}} \quad (2.46)$$

$$\dot{z}_o = \dot{\theta}_o + \Delta \quad (2.47)$$

The superimposed high frequency upon the slow scale will have two effects. The term $\langle \varphi \cos \tilde{\alpha}\tau \rangle$ contributes to a stiffening effect, as seen in stabilization of an inverted pendulum subject to high frequency base excitation (for example, see the studies Yabuno, Miura, and Aoshima (2004) and Thomsen (2003)). The term $\langle \mu(\dot{z} + \varphi') \rangle$

effectively acts to smoothen out the discontinuous signum function in the friction model. Both terms are given special consideration below.

Stiffening Effect: The averaging operation is performed on the fourth term in equation (2.45) leading to

$$\Delta \langle \varphi \cos \tilde{\alpha}\tau \rangle = \frac{\Delta^2}{2\pi} \int_0^{2\pi} [z \cos^2 \tilde{\alpha}\tau - \sin \tilde{\alpha}\tau \cos \tilde{\alpha}\tau] d(\tilde{\alpha}\tau) \quad (2.48)$$

$$= \frac{\Delta^2 z}{2} \quad (2.49)$$

After substituting equation (2.49) into equation (2.45), the effective stiffness of the torsional mode on the slow scale becomes $k_{eff} = 1 + \frac{1}{2} \frac{\tilde{m}^2 \tilde{\omega}^4}{\tilde{\alpha}^2}$. It is noted that this stiffening effect is independent of the friction model and arises because of coupling with the lateral vibrations. Thus, for fast enough driving speeds, this effect is present for a large class of rotors undergoing dry-friction whirl.

Smoothening Effect: Consideration is now given to the averaged frictional force in equation (2.45). The averaged friction coefficient is defined as $\bar{\mu}(\dot{z}) \equiv \langle \mu(\dot{z} + \varphi') \rangle$. First, examining the $\mathcal{O}(1)$ equation for $\dot{\theta}$, it is found that

$$\dot{\theta} = \dot{z} + \varphi' + \mathcal{O}(\tilde{\alpha}^{-1}) \quad (2.50)$$

$$\approx \dot{z} - \Delta [z \sin \tilde{\alpha}\tau + \cos \tilde{\alpha}\tau]$$

$$\approx \dot{z} - \Delta \sqrt{1 + z^2} \sin(\tilde{\alpha}\tau + \gamma) \quad (2.51)$$

where

$$\gamma = \arctan\left(\frac{1}{z}\right) + \begin{cases} 0 & \text{for } z \geq 0 \\ \pi & \text{for } z < 0 \end{cases} \quad (2.52)$$

It is noted that from the original assumption of small torsional motions, a reasonable approximation of $\sqrt{1+z^2} \approx 1$ may be employed, which then results in the approximation $\dot{\theta} \approx \dot{z} - \Delta \cos \tilde{\alpha}\tau$. For the sake of completeness, the remaining analysis will be carried out by using equations (2.51) and (2.52). Equations (2.51) and (2.52) are substituted into equations (2.9) and after performing the averaging operation, the average friction coefficient acting on the slow scale $\bar{\mu}(\dot{z})$ is obtained. The averaged friction coefficient $\bar{\mu}(\dot{z})$ takes a different form depending on the magnitude of $|\dot{z}(t)|$. If $|\dot{z}| > |\Delta\sqrt{1+z^2}|$, then there is no switch condition in the signum function, and after performing the necessary integrations, one obtains

$$\bar{\mu} = \mu(\dot{z}) + \frac{3}{2}\tilde{\mu}_3\Delta^2(1+z^2)\dot{z} \quad \text{for } |\dot{z}| > |\Delta\sqrt{1+z^2}| \quad (2.53)$$

In the instance when $|\dot{z}| \leq |\Delta\sqrt{1+z^2}|$, the values of the averaging operation depend on the value of the signum function. The quantity $\text{sgn}(\dot{z} + \varphi')$ takes on values of -1 for $\tau \in [\tau_a, \tau_b]$ and yields values of 1 for $\tau \in [0, \tau_a] \cup [\tau_b, 2\pi]$. The points of zero crossing τ_a and τ_b are determined to be

$$\begin{aligned} \tau_a &= \arcsin\left(\frac{\dot{z}}{-\Delta\sqrt{1+z^2}}\right) - \gamma \\ \tau_b &= \pi - \tau_a - 2\gamma \end{aligned} \quad (2.54)$$

With this information, and performing the necessary integrations, the effective fric-

tion coefficient acting on the slow scale is governed by equation (2.55).

$$\bar{\mu}(\dot{z}) = \begin{cases} \frac{2}{\pi}\mu_s \arcsin\left(\frac{\dot{z}}{-\Delta\sqrt{1+z^2}}\right) - \tilde{\mu}_1\dot{z} + \tilde{\mu}_3\dot{z}^3 + \frac{3}{2}\tilde{\mu}_3\Delta^2(1+z^2)\dot{z} & \text{for } |\dot{z}| \leq |\Delta\sqrt{1+z^2}| \\ \mu(\dot{z}) + \frac{3}{2}\tilde{\mu}_3\Delta^2(1+z^2)\dot{z} & \text{for } |\dot{z}| \geq |\Delta\sqrt{1+z^2}| \end{cases} \quad (2.55)$$

Because of the fast-scale vibrations, the signum function in equation (2.9) has been smoothed out and is replaced by the arcsine function in equation (2.55). This smoothing effect has been studied before in studies Nayfeh and Mook (1979); Thomsen (2003, 1999, 2002), as well as others. An interesting feature in the result of equation (2.55) is that the averaged friction coefficient also has dependence upon the slow-scale position z . As mentioned earlier, due to the small torsional motions, this dependence upon z is not strong. The effective friction coefficient given by equation (2.55) is plotted in Figure 2.7 as a function of the slow-scale relative speed and torsional deformation. In Figure 2.7, the parameters have been set so that $\Delta = -0.101$ corresponding to $\tilde{\alpha} = -8.0$, while the friction parameters have been selected so that $\mu_m = 0.005$, $\mu_s = 1.05\mu_m$, and $v_m = 0.05$ m/s. It is noted that the effective friction force in Figure 2.7 resembles planing forces experienced by a supercavitating body with similar types of nonlinearities (Nguyen and Balachandran, 2011). A cross-section in the $\mu - \dot{z}$ plane at $z = 0$ of Figure 2.7 is provided in Figure 2.8(a) for various values of Δ . With increasing drive speed and similarly Δ , the discontinuous friction force becomes smooth in nature. The effective normal forces for selected values of Δ are provided in Figure 2.8(b). Here, both the smoothing effect from the high-frequency excitation, and increasing normal force, originating from centrifugal forces, are apparent.

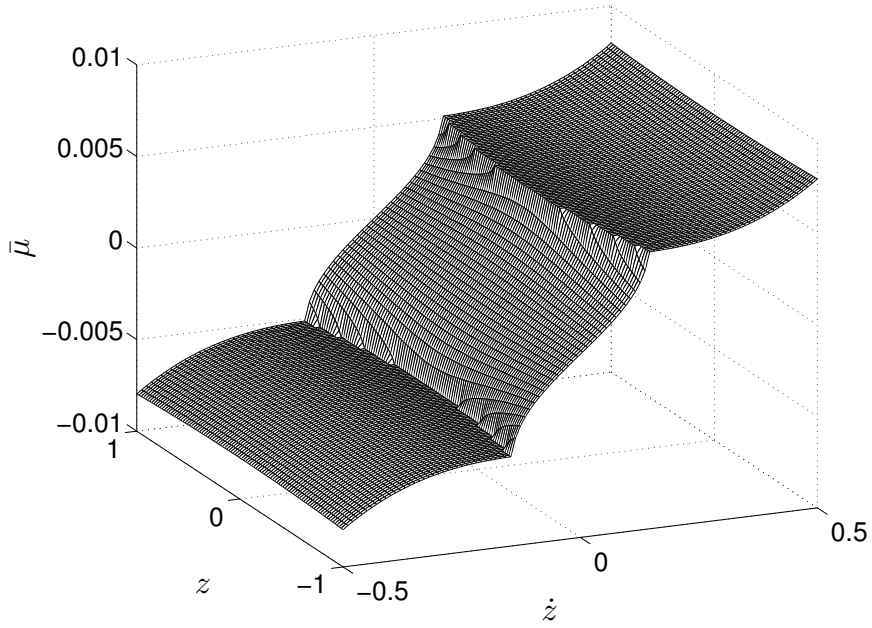


Figure 2.7: Effective friction coefficient given by equation (2.55) for $\Delta = 0.032$ corresponding to $\tilde{\alpha} = 12$.

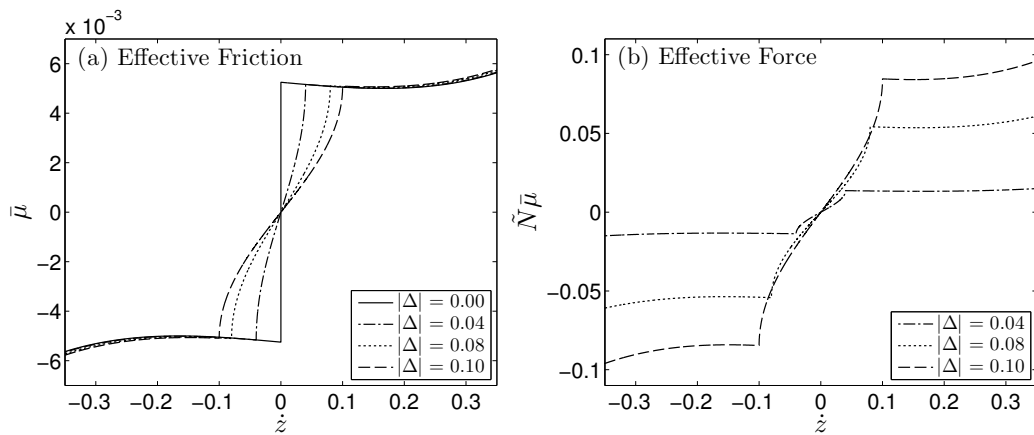


Figure 2.8: (a) Cross section of Figure 2.7 at $z = 0$ for different values of Δ . (b) Effective normal force at $z = 0$ for different values of Δ .

Approximate analytic solution

If the slow-scale velocity \dot{z} of the torsional vibration is sufficiently small, so that $|\dot{z}| \ll |\Delta\sqrt{1+z^2}|$, then the slow-scale variable, governed by equation (2.45), may be further linearized by performing a Taylor Series expansion of the averaged friction coefficient given by equation (2.55). In performing this operation, the slow-scale variable is governed by the following ordinary differential equation

$$\ddot{z} + \bar{c}\dot{z} + \bar{k}z = 0 \quad \text{for } |\dot{z}| \ll |\Delta\sqrt{1+z^2}| \quad (2.56)$$

where

$$\bar{c} = \tilde{N} \left(-\frac{2\mu_s}{\pi\Delta} - \tilde{\mu}_1 + \frac{3}{2}\tilde{\mu}_3\Delta^2 \right) + 2\zeta, \quad \bar{k} = 1 + \frac{\Delta^2}{2} \quad (2.57)$$

An algebraic, closed-form equivalent solution to equation (2.56) is

$$z(\tau) = C_1 e^{s_1\tau} + C_2 e^{s_2\tau} \quad (2.58)$$

with roots $s_{1,2}$ and amplitudes $C_{1,2}$ given by

$$s_{1,2} = \frac{1}{2} \left(-\bar{c} \pm \sqrt{\bar{c}^2 - 4\bar{k}} \right), \quad C_1 = z_o - C_2, \quad C_2 = \frac{\dot{z}_o - s_1 z_o}{s_2 - s_1} \quad (2.59)$$

Because $\bar{c} > 0$, perturbations on the slow scale will asymptotically decay to zero and only the fast-scale motions, governed by equation (2.43), contribute to the steady-state torsion response. For illustrative purposes, the analytic fast-scale solution (equation (2.43)), slow-scale solution (equation (2.58)) are shown in Figure 2.9(a), along with the superposition of both (equation (2.40)) to form an approximate solution for θ , provided in Figure 2.9(b). Comparisons of the simulations of the full system of equations given by equations (2.4a)-(2.8) and (2.12), simulations

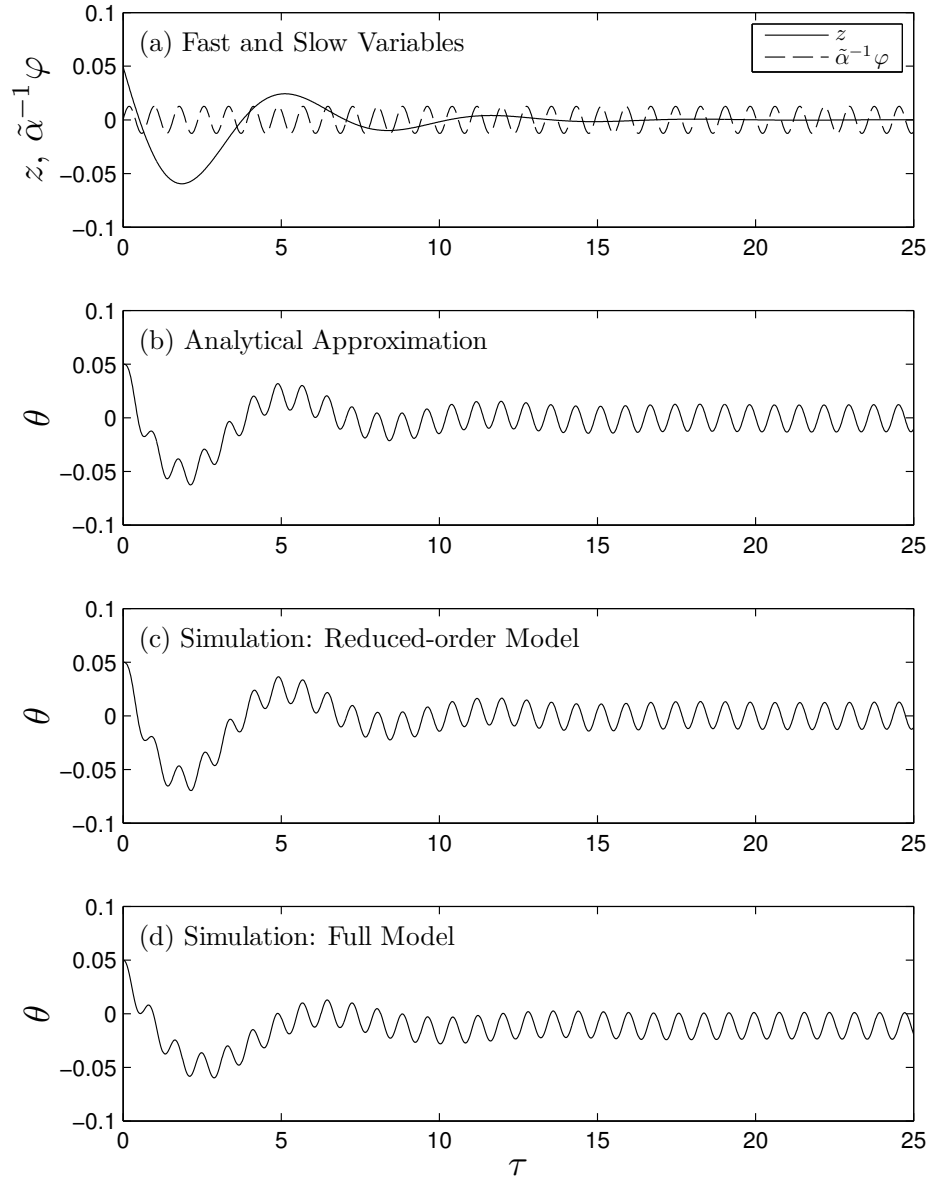


Figure 2.9: (a) Fast-scale and slow-scale variable histories (equations (2.43) and (2.58)). (b) Analytical approximation history (equations (2.43), (2.58), and (2.40)). (c) Simulations of reduced-order system (equation (2.33)). (d) Simulations of full system (equations (2.4a)-(2.8) and (2.12)).

of the reduced-order differential equation given by equation (2.33), and the approximate algebraic solution governed by equations (2.58),(2.43), and (2.40) are provided in Figure 2.9(b)-(d), respectively. Here, an initial displacement of $\theta_o = 0.05$, $\dot{\theta}_o = 0$ is applied to all three systems and the time histories are shown. The steady-state responses of the three solutions agree; however, there is discrepancy in transient motion, which is governed by equation (2.58) in the analysis. This can be attributed to differences in the effective damping \bar{c} . Additionally, the full model has a finite mean in the steady-state (i.e., a DC component), which is not captured in the reduced-order model or approximate solution. However, the qualitative features of the full model prediction, reduced-order model prediction, and results from analysis are in good agreement.

2.6 Summary

The Jeffcott rotor with torsional vibrations in the presence of continuous stator contact and subject to dry-friction has been studied within this chapter. In order to simplify the dynamics, a reduced-order equation has been constructed with the aim of capturing the torsional oscillation features during whirling motions. Key findings from the numerical studies and analysis of the reduced-order equation are highlighted below.

1. During forward whirling, if $v_c < v_w < v_m$ and $f_1 < 0$, torsional vibrations can be excited through a Hopf instability in the reduced-order model. Numerical simulations of the full model reveal that with the onset of this bifurcation in

the reduced-order model, the rotor is likely to break contact with the stator or whirl with a non-constant speed.

2. During forward whirling, with increasing damping ratio, the bifurcation in the reduced-order model can be suppressed as given by equation (2.31), after which no vibrations exist in simulations of the full system.
3. During backward whirling, if the rotor whirls at high speeds, away from resonance, the discontinuous dry friction starts to behave in a manner similar to that of viscous damping.
4. During both forward whirling and backward whirling, the torsional vibrations are subject to a centrifugal stiffening effect that originates from coupling with the lateral vibrations. This effect is consistent with previously published experimental work (Diangui, 2000).

Chapter 3

Rotor Dynamics with Coupled Torsional-Lateral Motions with Gyroscopic Effects

In the last chapter, the torsional vibration response was analyzed for a reduced-order, lumped-parameter rotor model. Although this reduced-order model was able to demonstrate certain phenomena capable in rotor-stator systems, it is inadequate at predicting the dynamics in more complex rotor systems. For instance, the dynamics of slender structures can be better described with distributed-parameter models, which have the virtue of relating the mass and stiffness to physical quantities of the system, and can capture high-order modes. Additionally, the modified Jeffcott rotor presented in Chapter 2 was a planar rotor, so that it did not account for gyroscopic effects (i.e., finite rotations about the y and z axes). Some of these dynamic features, which were not considered in the reduced-order model presented in Chapter 2, are addressed within this chapter. The study of these additional dynamic features is motivated by the need to understand the dynamic behavior observed in an experimental slender rotor system.

Here, the dynamics of slender rotating beams are studied experimentally, analytically, and numerically. Phenomena observed in the experimental arrangement, including the response of torsional vibrations with continuous stator contact, are presented. The reduced-order model presented in the previous chapter is insuffi-

cient in predicting the dynamic response of the slender structure in the experiment. Thus, within this chapter, a distributed-parameter model is derived with the intent of capturing experimentally observed phenomena. The resulting partial differential equations are strongly nonlinear and closed-form solutions are not feasible; therefore, solutions to the nonlinear equations are numerically determined and numerical predictions are compared with experimental data. Under a given set of assumptions, the system of differential equations can be reduced to a single, nonlinear equation which is used to predict the torsion response while in continuous stator contact. This single DOF equation gives insights into the origins of the components observed in the torsion response spectra.

3.1 Experimental arrangement

A photograph with annotations of the experimental arrangement is shown in Figure 3.1. An aluminum rotor is secured to the end of a slender aluminum rod, which is referred to as a string in this work due to its slenderness. The rotor is enclosed within an aluminum circular stator, and when in contact, the rotor is subject to frictional forces. The entire string-rotor assembly is driven by a chuck which is connected to a stiff stainless steel drive shaft and servo-motor. The eccentricity and unbalanced mass of the rotor may be varied by using a series of holes located radially away from the center of the rotor. The parameters for the experimental arrangement are listed in Table 3.1. The natural frequencies and the damping ratios for the first torsion and bending modes have been obtained from the free response

of the system without mass imbalance. More specifically, the natural frequencies were determined through an impulse-input response of the structure, while the damping ratios were determined with the log-decrement method.

While in operation, data are gathered from the system by using digital video cameras, a torque sensor, and strain gages. The strain gages are secured to the string near the chuck, where linear strain theory predicts the occurrence of maximum strains for the torsional and bending motions. The wires from the strain gages are fed back to a data acquisition module through a slip-ring. By using a special rosette and signal processing procedure, bending and torsional strain information is extracted from the sensors. Data have been gathered for drive speeds and whirl speeds in the vicinity of the first bending and torsional natural frequencies. Caution was taken to not excite the second bending mode of vibration. Due to the large inertia of the rotor at the end of the string, the second torsional natural frequency is in the kilohertz (kHz) range and the corresponding vibration mode has little participation in the system dynamics. Consequently, only the first torsional and bending modes are excited and the strain measurements can be directly related to the corresponding displacements. In addition to the strain gage data, a digital video camera mounted above the rotor is able to record the lateral motions. By using an image processing procedure developed by the author, the displacement time histories of the rotor may be determined from the video data. Furthermore, the coefficient of friction between the rotor and stator is varied by securing a thin layer of synthetic rubber to each surface, or by introducing a lubricant such as oil. An aluminum on aluminum contact surface corresponds to a lower coefficient of friction in comparison to the

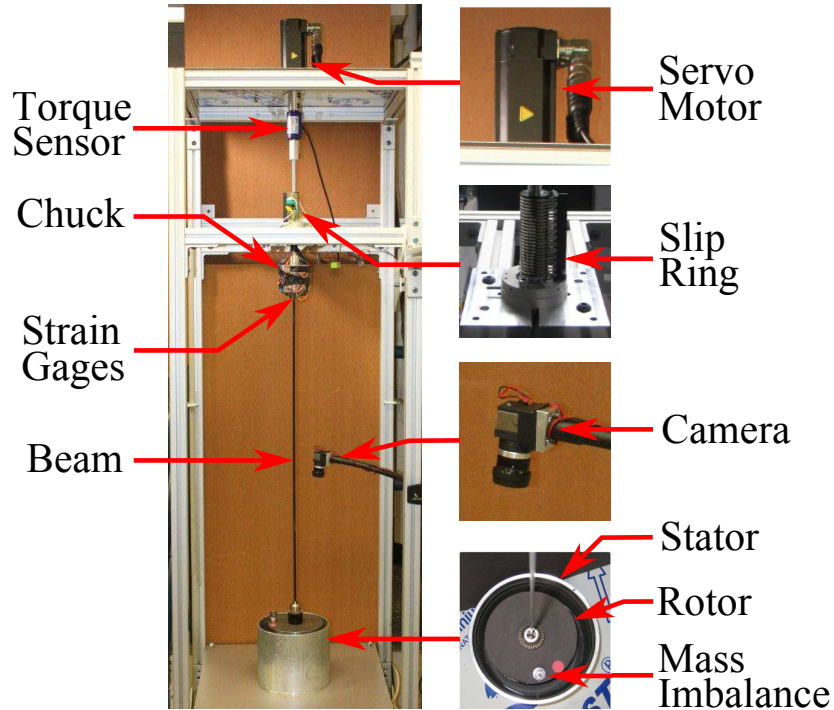


Figure 3.1: Vertical drill string experimental apparatus.

rubber on rubber contact surface, which is representative of a higher coefficient of friction.

3.2 Experimental results

3.2.1 Characteristic whirl phenomena

Representative motions of the bottom rotor are illustrated in Figure 3.2(a), Figure 3.3(a), and Figure 3.4(a). At low driving speeds, and low weights of unbalanced mass, the rotor stays near the center of the stator. However, as the driving speed and/or weight of the unbalanced mass is increased, the lateral forcing becomes larger and the rotor has a high likelihood of coming into contact with the stator. Upon contact, several behaviors are possible. When the coefficient of friction

Table 3.1: Experimental arrangement parameters used in simulations.

Parameter	Value	units
D_R	0.1534	m
D_S	0.1905	m
e	0.0650	m
L	1.1300	m
M	0.6250	Kg
m	0.010-0.090	Kg
r	1.600	mm
E	$70 \cdot 10^9$	Pa
G	$25 \cdot 10^9$	Pa
Ω_{back}	11-65	RPM
$\Omega_{forward}$	31-56	RPM
ζ_b	0.0004	-
ζ_t	0.002	-
f_{b1}	0.50	Hz
f_{b2}	6.92	Hz
f_t	1.75	Hz

between the surfaces of the rotor and stator is small in magnitude (corresponding to an aluminum to aluminum contact surface), the rotor may stay in continuous contact with the stator and synchronously whirl in the direction of rotation. In contrast, when the coefficient of friction between the two surfaces is large (corresponding to a rubber on rubber contact surface), the rotor has a higher probability of undergoing dry-friction whirling motions. Through both simulations and experiments, it is found that friction plays a large role in transient response of the system and ultimately determines the steady-state motion (i.e., whirl with no contact, forward synchronous whirl with contact, and backward dry-friction whirling) (Li and Paidoussis, 1994). These results indicate that the friction is a dominant parameter in mapping out the *basin of attraction* – the set of initial conditions (or states of the system) that converge to a steady-state motion. Although friction plays a large

role in determining the steady-state response, it does not have a large effect on the existence of the steady-state solutions. In other words, all three solutions shown in Figure 1.3 exist for a large range of friction values.

Experimental data for the rotor during forward synchronous whirling with stator contact is provided in Figures 3.2(a)-(c). Under these conditions, the relative speed between the two surfaces is non-zero and slipping is said to occur. The lateral displacement time histories denoted by $v(L, t)$ and $w(L, t)$, which correspond to the data given in Figure 3.2(a), are presented in Figure 3.2(b). After using the transformation $Z(t) = v(L, t) + j \cdot w(L, t)$, where j is the imaginary number, the two displacements may be cast into complex form. The centered Fourier transform of the complex signal is shown in Figure 3.2(c). Here, positive frequencies correspond to whirling in the direction of rotation, while negative frequencies denote whirling in the opposite direction of rotation (Yamamoto and Ishida, 2001). The motor driving speed was set to 85 revolutions per minute (RPM) for the data presented in Figures 3.2(a)-(c), and the corresponding driving frequency is observed at 1.42 Hz in Figure 3.2(c).

Experimental data for the rotor during dry-friction whirl (similarly, backward whirl with contact, or rolling) are shown in Figures 3.3(a)-(c). Under perfect rolling conditions, the relative speed between the rotor and the stator is equal to zero. Under the assumption that the deflection of the stator and the torsional vibration amplitudes are both small, as discussed in references (Black, 1967, 1968; Feng and Zhang, 2002; Yamamoto and Ishida, 2001; Vljajic, Liao, Karki, and Balachandran, 2011, 2012), the response angular speed can be approximated as

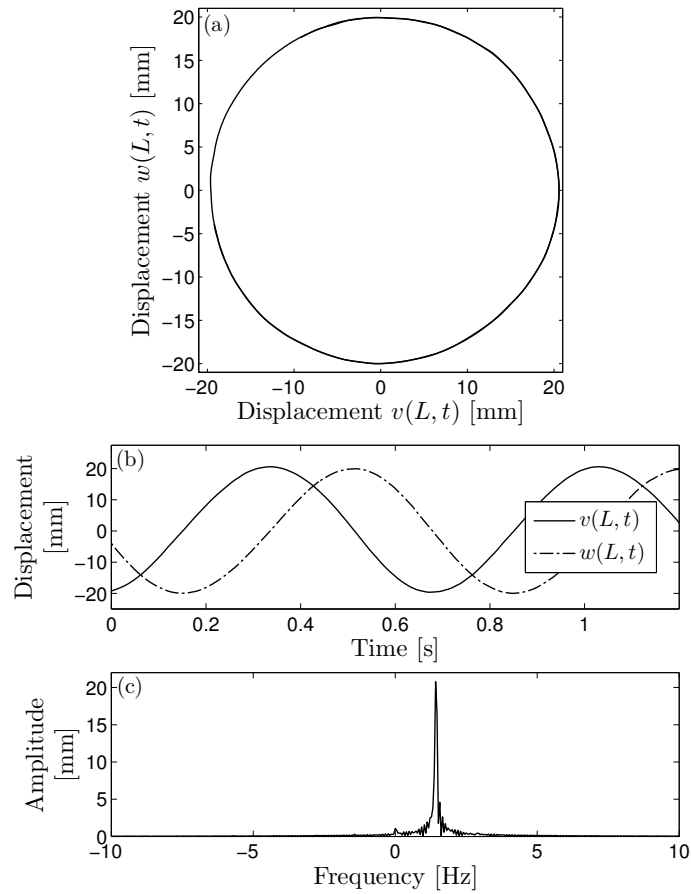


Figure 3.2: Experimentally observed forward whirling motions: (a) trajectory of rotor center within the stator, (b) time histories of the $v(L, t)$ and $w(L, t)$ displacement components, and (c) Fourier spectra of complex displacement quantity.

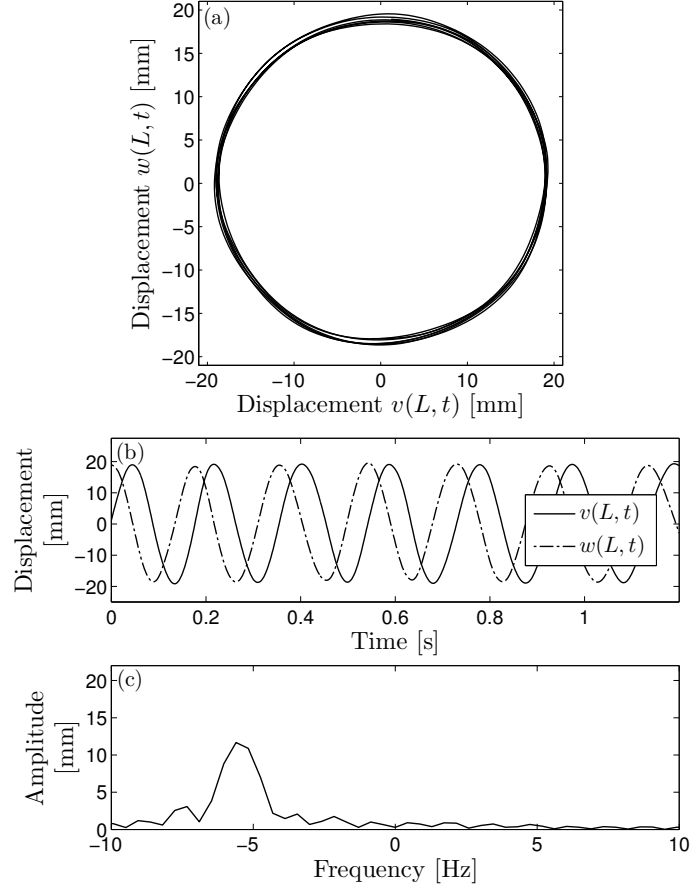


Figure 3.3: Experimentally observed backward whirling motions: (a) trajectory of rotor center within the stator, (b) time histories of the $v(L, t)$ and $w(L, t)$ displacement components, and (c) Fourier spectra of complex displacement quantity.

$$\Omega_{back} = -\frac{D_R}{D_S - D_R}\Omega_{for} = -\frac{R}{\delta}\Omega_{for} \quad (3.1)$$

For the given experimental parameters, $R/\delta \approx 4.13$. The centered Fourier transform of the data provided in Figure 3.3(b) is shown in Figure 3.3(c). For this specific experiment, the driving angular frequency was again approximately 85 RPM or 1.42 Hz. The peak value in the spectrum is approximately at -5.61 Hz, which is in close agreement with the value obtained from equation (3.1). Here, the negative frequency indicates that the rotor is whirling in the opposite direction of the drive rotation.

Additionally, for low friction coefficient values and small levels of unbalanced mass, and for certain driving speeds, the rotor may undergo impacting motions, as depicted in Figure 3.4(a)-(c). It is mentioned that impacting motions are difficult to reproduce experimentally and numerically, as small perturbations from these motions may cause the rotor to undergo forward whirling with contact, backward whirling with contact, or the rotor may simply whirl without contact. The centered Fourier transform of the data in Figure 3.4(b) is presented in Figure 3.4(c). For this particular experiment, the Fourier spectra shows a forward whirling frequency of 1.07 Hz which corresponds to the driving speed of 61 RPM, as well as a component at -1.40 Hz which is assumed to originate from collisions with the stator.

3.2.2 Torsional vibrations with continuous rotor-stator contact

Within this section, experimental data of the torsion response while the rotor undergoes forward and backward whirling motion is presented. When a linear system is forced at a particular frequency Ω , the system response will also occur at the same frequency Ω . As will be shown in this section, the torsion response spectra contain frequencies that are different than the driving (or forcing) frequency of the system. These additional response components are a strong indication that nonlinearities are present in the system. For all of the data presented in this section, the contact surface was aluminum on aluminum.

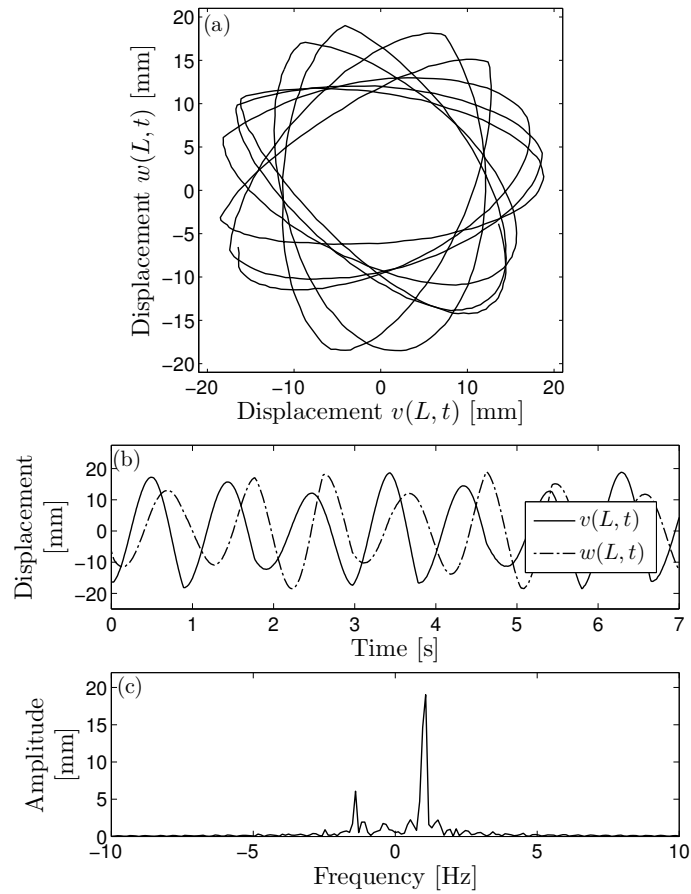


Figure 3.4: Experimentally observed impacting motions: (a) trajectory of rotor center within the stator, (b) time histories of the $v(L, t)$ and $w(L, t)$ displacement components, and (c) Fourier spectra of complex displacement quantity.

3.2.2.1 Forward whirling

The Fourier transforms of the torsional strain collected during forward, synchronous whirling are given in Figure 3.5. Here, the DC offset (0 Hz frequency component) has been removed, and the amplitudes have been normalized by dividing throughout by the largest amplitude and raising the result to the 0.8th power for clarity. This torsional strain response corresponds to the rotor radial movements along the line AB in Figure 1.3. Data have been collected for 56 different driving speeds between 31-56 RPM (0.52-0.93 Hz) for a total of 60 seconds. From Figure 3.5, it is seen that the component at the driving speed f_d is one of the dominant components in the frequency response; small amplitude contributions at the harmonics of f_d are also present. Additionally, large amplitude responses occur when the harmonic components $2f_d$ and $3f_d$ coincide with the natural frequency f_t .

3.2.2.2 Backward whirling

The Fourier transforms of the torsional strain collected during backward, dry-friction whirling are given in Figure 3.6, where the same normalization procedure has been implemented. The strain response presented in Figure 3.6 corresponds to the radial displacement along the line CD in Figure 1.3 for driving speeds ranging from 11-65 RPM, or equivalently, 0.18-1.08 Hz. In this case, data have been gathered at 94 different driving speeds for 60 seconds each. The strongest component of the response for all driving speeds occurs at the sum of the whirling frequency and driving frequency, $f_w + f_d$. Furthermore, the second strongest contribution occurs

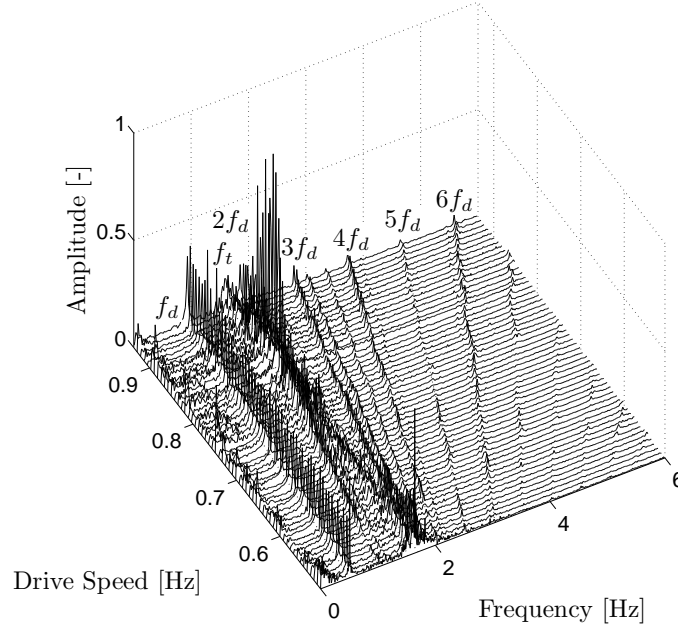


Figure 3.5: Experimentally determined frequency content of torsional strain during forward synchronous whirling.

at the drive speed f_d . Additionally, small amplitude components at $f_w - f_d$, f_w , $f_w + 2f_d$ and $2(f_w + f_d)$ are also visible in the response spectra. These response frequencies in the case of backward whirling were reported in the work Vlajic, Liao, Karki, and Balachandran (2012).

3.3 Modeling efforts

Within this section a structural model with coupled torsional and lateral motions is derived along with a force-interaction model that aims to capture the dynamics observed in the experimental arrangement.

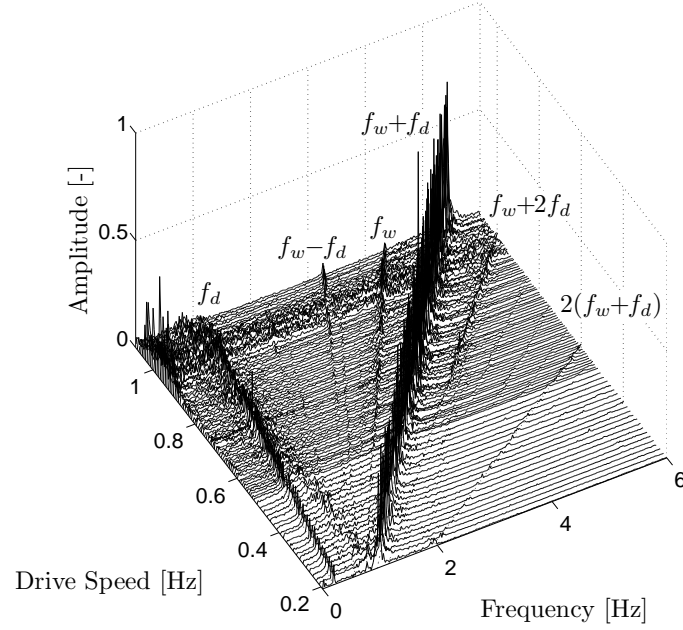


Figure 3.6: Experimentally determined frequency content of torsional strain during dry-friction whirling.

3.3.1 Distributed-parameter structural model

A schematic which depicts the structure shown in Figure 3.1 is provided in Figure 3.7. In the modeling efforts, the beam or string is taken to be a distributed parameter element, while the disk is modeled as a rigid, lumped-parameter element. Let the fixed xyz frame with mutually orthogonal unit vectors \mathbf{ijk} be used to describe the undeformed geometry of the initially straight string. Additionally, let $x_3y_3z_3$ be the reference frame in the deformed configuration with mutually orthogonal unit vectors $\mathbf{i}_3\mathbf{j}_3\mathbf{k}_3$, with the frame's origin located along the centerline of the string. An arbitrary material point P_o in the undeformed configuration is displaced to the point P in the deformed configuration. The position vector from the origin of the xyz frame to the origin of the local coordinate frame $x_3y_3z_3$ is given by

$$\mathbf{r}_{C/O} = (x + u(x, t))\mathbf{i} + v(x, t)\mathbf{j} + w(x, t)\mathbf{k} \quad (3.2)$$

where $u(x, t)$, $v(x, t)$, and $w(x, t)$ are the displacements of the string centerline along the \mathbf{i} , \mathbf{j} , and \mathbf{k} directions, respectively. Likewise, the position vector from the local coordinate frame to the material point located in the cross-section of the string is given by

$$\mathbf{r}_{\mathbf{P}/\mathbf{C}} = 0\mathbf{i}_3 + y_3\mathbf{j}_3 + z_3\mathbf{k}_3 \quad (3.3)$$

Next, a relationship between the orientation of the local coordinate frame relative to the fixed coordinate frame is needed in order to completely determine the position of the material point in the fixed frame and to construct an expression for the velocity of the material point P . This relationship is given by the use of 1-2-3 Euler angles, which decomposes the transformation from the fixed frame to the local frame through the use of three rotations. A detailed derivation of the 1-2-3 Euler angles is given in Appendix A, along with a derivation of the angular velocity of the local coordinate frame with respect to the fixed coordinate frame, which is

$$\boldsymbol{\omega} = (\dot{\beta} - \dot{\alpha}S_\psi)\mathbf{i}_3 + (\dot{\psi}C_\beta - \dot{\alpha}S_\beta)\mathbf{j}_3 + (\dot{\psi}S_\beta + \dot{\alpha}C_\beta)\mathbf{k}_3 \quad (3.4)$$

The $(\dot{\cdot})$ operation denotes the partial derivative with respect to time and the $S_{(\cdot)}$ and $C_{(\cdot)}$ symbols denote the sine and cosine function of the argument, respectively. For the given configuration, β is a measure of the angular displacement of the lower disk which may undergo large displacements. On the other hand, ψ and α are measures of bending, which are assumed to be small and hence the trigonometric functions of the two angles may be approximated by the first term of the Taylor series expansion. Further, from Bernoulli-Euler beam theory, $\psi = -w'$ and $\alpha = v'$ where the operation $(\cdot)'$ denotes the partial derivative with respect to x . Since β is

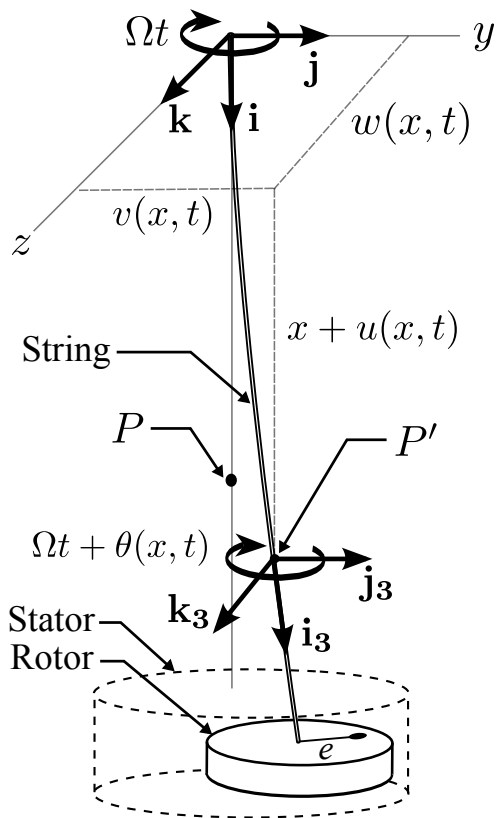


Figure 3.7: Schematic of the structural model used to develop the governing equations of motion.

a measure of the angular displacement about the x direction, it can be decomposed into a sum of the torsional deformation and a rigid body rotation. By using the above expression for the angular velocity, the kinetic energy of the shaft may be expressed as

$$\mathcal{T}_{string} = \frac{1}{2} \int_{Vol} \rho (\mathbf{r}_{\mathbf{P}/\mathbf{O},t} \cdot \mathbf{r}_{\mathbf{P}/\mathbf{O},t}) dVol \quad (3.5)$$

where ρ is the cubic density and integration over the continuum has been carried out. The string is initially straight so that the deformed coordinate system aligns with the fixed coordinate system, and shear effects are neglected due to the slenderness of the structure. The local coordinate system is aligned with the principal axes of inertia of the string, such that the kinetic energy of the string may be written as

$$\mathcal{T}_{string} = \frac{1}{2} \int_0^L \left[\rho A (\dot{u}^2 + \dot{v}^2 + \dot{w}^2) + \rho I (\dot{v}'^2 + \dot{w}'^2) + \rho I_o \dot{\beta}^2 + 2\rho I_o \dot{\beta} \dot{v}' w' \right] dx \quad (3.6)$$

A detailed derivation of the string kinetic energy can be found in Appendix B. Similarly, it follows that the kinetic energy of the lower disk is given by

$$\mathcal{T}_{rotor} = \frac{1}{2} \left[M (\dot{u}^2 + \dot{v}^2 + \dot{w}^2) + I_D (\dot{v}'^2 + \dot{w}'^2) + I_{D_o} (\dot{\beta}^2 + 2 \dot{\beta} \dot{v}' w') \right] \Big|_{x=L}$$

If the rotary inertia of the unbalanced mass about the z and y axes is neglected, the kinetic energy of the unbalanced mass is determined to be

$$\mathcal{T}_{ubm} = \frac{m}{2} \left[\dot{u}^2 + (\dot{v} - \dot{\beta} e \sin \beta)^2 + (\dot{w} + \dot{\beta} e \cos \beta)^2 \right] \Big|_{x=L} \quad (3.7)$$

Next, in order to construct the system Lagrangian, an expression for the potential energy of the system is determined. From linear elasticity, the potential

energy of the string can be expressed as

$$\mathcal{U} = \frac{1}{2} \int_0^L [EAu'^2 + EI(v''^2 + w''^2) + GI_o\beta'^2 - 2Su'] dx \quad (3.8)$$

In equation (3.8), the first term represents the axial potential energy, the second and third terms account for the potential energy due to bending, the fourth term is a measure of the torsion potential energy, and the last term accounts for the axial pre-stress on the beam due to a force S . Here, $S = Mg$, where M is the total mass of the rotor and g is the acceleration due to gravity. Next, through geometric reasoning, the strain in the x direction can be expressed as a function of the two bending displacements v and w through geometry as

$$dx^2 = \left(dx + \frac{\partial u}{\partial x} dx\right)^2 + \left(\frac{\partial v}{\partial x} dx\right)^2 + \left(\frac{\partial w}{\partial x} dx\right)^2 \quad (3.9)$$

Making use of the binomial expansion theorem and rearranging the above equation, the geometric relation may be cast into the following form

$$\frac{\partial u}{\partial x} \approx -\frac{1}{2} \left(\left(\frac{\partial v}{\partial x}\right)^2 + \left(\frac{\partial w}{\partial x}\right)^2 \right) \quad (3.10)$$

The above relation is a result of the *inextensibility condition*, which is constraint that prevents the centerline of the beam from extending or contracting. Equation (3.10) is substituted into equation (3.8). In addition, the variation of the external work can be expressed as

$$\delta\mathcal{W} = \lambda [F_{tan}R\delta\beta + F_v\delta v + F_w\delta w] \quad (3.11)$$

where λ is a contact parameter that is equal to unity when the rotor is in contact with the stator and zero otherwise. It is assumed that the axial inertia is negligible,

and attention is focused on the torsional and bending vibrations. For a constant rotating angular speed Ω , the transformation $\beta = \Omega t + \theta$ can be used, where θ is the torsional deformation. The Lagrangian may then be written as

$$\mathcal{L} = \mathcal{T} - \mathcal{U} \quad (3.12)$$

where

$$\mathcal{T} = \mathcal{T}_{string} + \mathcal{T}_{rotor} + \mathcal{T}_{umb} \quad (3.13)$$

Invoking the Extended Hamilton's Principle,

$$\int_{t_1}^{t_2} \delta(\mathcal{L} - \mathcal{W}) dt = 0 \quad (3.14)$$

one can obtain the equations of motion described by a system of three nonlinear coupled partial differential equations with ten associated boundary conditions. The governing equations of motion for $0 < x < L$ are obtained as

$$\rho A \ddot{v} - \rho I \ddot{v}'' - \rho I_o \left(\ddot{\beta}' w' + \ddot{\beta} w'' + \dot{\beta}' \dot{w}' + \dot{\beta} \dot{w}'' \right) + EI v'''' - S v'' = 0 \quad (3.15a)$$

$$\rho A \ddot{w} - \rho I \ddot{w}'' + \rho I_o \left(\dot{\beta}' \dot{v}' + \dot{\beta} \dot{v}'' \right) + EI w'''' - S w'' = 0 \quad (3.15b)$$

$$\rho I_o \left(\ddot{\beta} + \ddot{v}' w' + \dot{v}' \dot{w}' \right) - GI_o \beta'' = 0 \quad (3.15c)$$

with boundary conditions at $x = L$

$$(M + m)\ddot{v} + \rho I \ddot{v}' + \rho I_o \ddot{\beta} w' + \rho I_o \dot{\beta} \dot{w}' - EI v''' + S v' = me \left(\ddot{\beta} \sin \beta + \dot{\beta}^2 \cos \beta \right) \quad (3.16a)$$

$$I_d \ddot{v}' + I_{D_o} \left(\ddot{\beta} w' + \dot{\beta} \dot{w}' \right) + EI v'' = 0 \quad (3.16b)$$

$$(M + m)\ddot{w} + \rho I \ddot{w}' - \rho I_o \dot{\beta} \dot{v}' - EI w''' + S w' = me \left(-\ddot{\beta} \cos \beta + \dot{\beta}^2 \sin \beta \right) \quad (3.16c)$$

$$I_D \ddot{w}' - I_{D_o} \dot{\beta} \dot{v}' + EI w'' = 0 \quad (3.16d)$$

$$(I_{D_o} + me^2) \ddot{\beta} + I_{D_o} (\ddot{v}' w' + \dot{v}' \dot{w}') + GI_o \beta' = me (\ddot{v} \sin \beta - \ddot{w} \cos \beta) \quad (3.16e)$$

The boundary conditions at $x = 0$ are simply

$$v = 0, v' = 0 \quad (3.17a)$$

$$w = 0, w' = 0 \quad (3.17b)$$

$$\theta = 0 \quad (3.17c)$$

The system of partial differential equations given by equations (3.15)-(3.17) are then transformed to a system of ordinary differential equations by using a Galerkin projection. This is done by multiplying each equation of (3.15) by a respective trial function that is only a function of the spatial coordinate x and integrating over the length of the string. The quantities v , w , and θ are taken to be separable in space and time and may be expanded as follows:

$$v(x, t) = \sum_{i=0}^N V_i(t) \phi_{vi}(x) \quad (3.18a)$$

$$w(x, t) = \sum_{i=0}^N W_i(t) \phi_{wi}(x) \quad (3.18b)$$

$$\theta(x, t) = \sum_{i=0}^N \Theta_i(t) \phi_{\theta i}(x) \quad (3.18c)$$

The temporal functions V_i , W_i , and Θ_i are unknown quantities. On the other hand, the spatial functions $\phi_{vi}(x)$, $\phi_{wi}(x)$, and $\phi_{\theta i}(x)$ are chosen to satisfy the linear boundary conditions. These functions are also selected as the trial functions. In equations (3.18), i is the mode number and N is the total number of modes. The rotor is expected to dominate the inertia effects of the system, and the mass of the shaft is neglected as a first approximation. Equations (3.18) are substituted into equations (3.15)-(3.17) where a single mode is considered for each displacement directions. The rotor on the string acts as a lumped mass which further separates the natural frequencies between each mode; thus, the single mode assumption is a reasonable approximation. Linear viscous damping is added to the system, and the three coupled ordinary differential equations of motion for the system are obtained as

$$\begin{aligned}
a_1\ddot{V} + a_2\dot{V} + a_3\Omega\dot{W} + a_4V + a_5(\dot{\Theta}\dot{W} + \ddot{\Theta}W) - me\phi_\theta\phi_v\ddot{\Theta}\sin(\Theta\phi_\theta + \Omega t)\Big|_{x=L} \\
- me\phi_v\left(\dot{\Theta}\phi_\theta + \Omega\right)^2\cos(\Theta\phi_\theta + \Omega t)\Big|_{x=L} = \lambda\phi_vF_v\Big|_{x=L} \quad (3.19)
\end{aligned}$$

$$\begin{aligned}
b_1\ddot{W} + b_2\dot{W} + \Omega b_3\dot{V} + b_4W + b_5\dot{\Theta}\dot{V} + me\phi_w\phi_\theta\ddot{\Theta}\cos(\Theta\phi_\theta + \Omega t)\Big|_{x=L} \\
- me\phi_w\left(\dot{\Theta}\phi_\theta + \Omega\right)^2\sin(\Theta\phi_\theta + \Omega t)\Big|_{x=L} = \lambda\phi_wF_w\Big|_{x=L} \quad (3.20)
\end{aligned}$$

$$\begin{aligned}
c_1\ddot{\Theta} + c_2\dot{\Theta} + c_3\Theta + c_4(\ddot{V}W + \dot{V}\dot{W}) + me\ddot{W}\phi_w\phi_\theta\cos(\Theta\phi_\theta + \Omega t)\Big|_{x=L} \\
- me\ddot{V}\phi_v\phi_\theta\sin(\Theta\phi_\theta + \Omega t)\Big|_{x=L} = \lambda\phi_\theta F_{tan}\frac{D_R}{2}\Big|_{x=L} \quad (3.21)
\end{aligned}$$

3.3.2 Rotor-stator force-interaction model

In the context of rotor-stator interactions, there are various classifications of phenomena and dynamic behavior, which were discussed in Section 3.2. The contact between the rotor and stator are commonly described through either a switching model or an impact model. Difficulties in numerical integration arise when using impacting models for certain rotor motions, such as continuous stator contact or grazing impacts (zero velocity impact). In light of this, the current model is a switching model which allows for both rolling, rubbing, and impacting behavior, albeit this switching model is numerically stiff and computationally expensive. This force model has been adapted from Liao, Balachandran, Karkoub, and Abdel-Magid (2011); Leine, van Campen, Kraker, and van den Steen (1998); and Feng and Zhang (2002), and is non-smooth in nature due to both the contact condition and friction. A schematic of the rotor when in contact with the stator and parameter definitions are shown in Figure 3.8. In order to determine the presence of contact, the following definitions are used:

$$\delta = \frac{1}{2}(D_S - D_D) \quad (3.22)$$

$$\Gamma = \sqrt{w(L, t)^2 + v(L, t)^2} \quad (3.23)$$

$$\lambda = \begin{cases} 0 & \text{for } \Gamma \leq \delta \\ 1 & \text{for } \Gamma > \delta \end{cases} \quad (3.24)$$

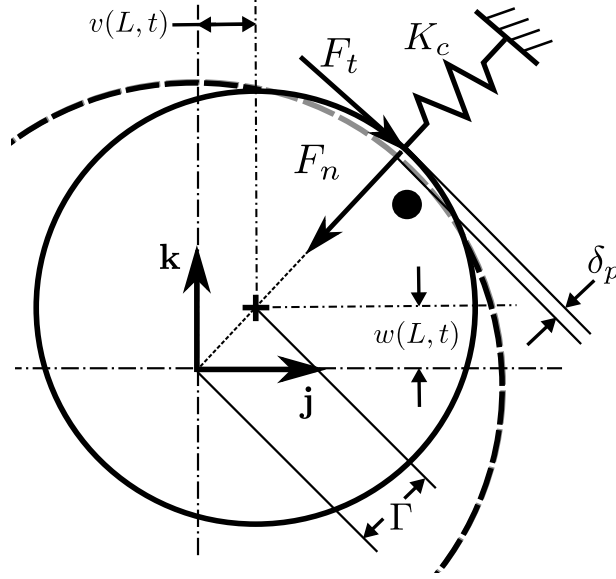


Figure 3.8: Schematic of forces when the rotor is in contact with the stator.

The coefficient of friction and the magnitude of the tangential force and normal force are given by

$$F_n = \begin{cases} 0 & \text{for } \Gamma \leq \delta \\ K_c(\Gamma - \delta) & \text{for } \Gamma > \delta \end{cases} \quad (3.25)$$

$$(3.26)$$

$$\mu = -\frac{2}{\pi} \arctan(\epsilon_f v_{rel}) \left[\frac{\mu_s - \mu_d}{1 + \delta_f |v_{rel}|} + \mu_d \right] \quad (3.27)$$

$$F_t = \mu \cdot F_n \quad (3.28)$$

In equation (3.27), the normalized arctan function is used to approximate the signum function to account for the change in the direction of friction as the relative speed changes sign. This was also implemented in Section 2.1.2. The parameter ϵ_f determines the steepness of the approximation of the vertical segment of signum function. Additionally, the parameter δ_f is a positive number that determines the rate at which the static friction coefficient approaches the dynamic friction coefficient

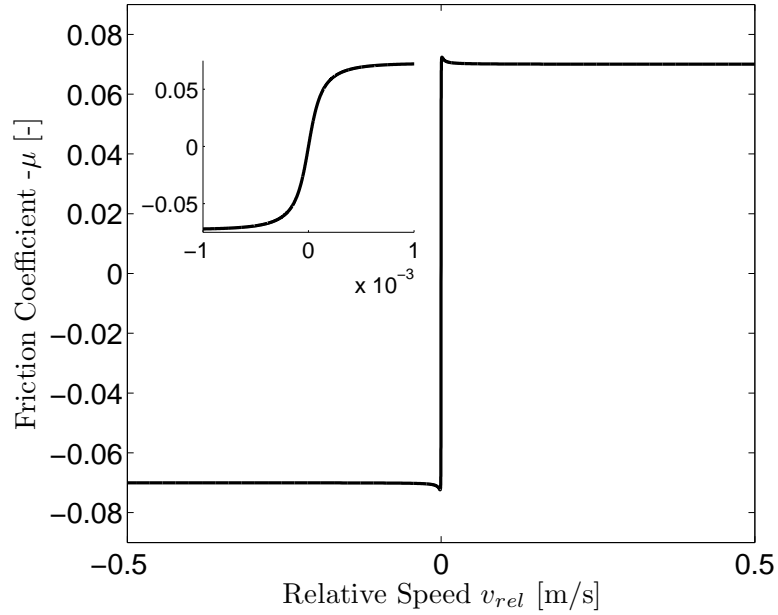


Figure 3.9: Coefficient of friction μ as a function of the relative speed for the model given by equation (3.27).

with respect to the relative velocity. For illustration purposes, the negative form of equation (3.27) is plotted in Figure 3.9 for the parameters given in Table 3.2. The frictional force acts to damp out vibrations when $|v_{rel}|$ is approximately less than $1e^{-3}$ (see the expanded section of Figure 3.9). However, when the relative speed is near zero, but $|v_{rel}|$ is greater than $1e^{-3}$, the frictional force effectively has negative damping and acts to excite vibrations. This type of friction can lead to Hopf instabilities (e.g., Leine and Nijmeijer (2004)). It is noted that the friction model presented here is different than the model presented in Section 2.1.2. Although both models are qualitatively similar, the model presented here was selected because it is one of the simplest models that can capture the difference between static and dynamic friction. The focus of this chapter is not on modeling the friction, but rather studying the response of the structure. The model selected here is able

to capture the dominate features of friction on the macroscopic scale, such as the difference between static and dynamic friction and its behavior at $v_{rel} = 0$. The normal and tangential forces may be transformed to accommodate the expression for external work and the equations of motion by using the transformations

$$F_v = \frac{-F_t w(L, t) - F_n v(L, t)}{\Gamma} \quad (3.29)$$

$$F_w = \frac{F_t v(L, t) - F_n w(L, t)}{\Gamma} \quad (3.30)$$

Table 3.2: Friction parameters used in simulations.

Parameter	Value	units
K_c	10^6	Nm^{-1}
μ_d	0.07	-
μ_s	$1.2\mu_d$	-
ϵ_f	10^4	-
δ_f	10^3	-

A schematic of the forces acting on the rotor during contact are shown in Figure 3.8. The direction of the normal force always starts at the point of contact and points towards the geometric center of the stator. The magnitude of the normal force is linearly proportional to the penetration depth $\delta_p = \Gamma - \delta$. The direction of the tangential force, by definition, acts to always oppose the direction of rotation. The magnitude of the tangential force determined by a combination of the normal force and the frictional force as given by equation (3.28).

3.4 Simulation Results

3.4.1 Characteristic whirl motions

The equations of motion are numerically integrated by using a modified second-order Rosenbrock solver that is better suited for solving stiff ordinary differential equations, such as the system at hand. The parameters used to generate the numerical results correspond to the experiments, and the associated values are given in Tables 3.1 and 3.2. The damping ratios for the bending and torsion motions were experimentally obtained from the free-response data of the system. The model predictions confirm the motion characteristics and phenomena observed in the experiments including dry-friction whirl, forward whirling with contact, and impacting motions. As a comparative example, experimental data and numerical predictions are shown in Figure 3.10 for the same system parameters and similar initial conditions. In both the experiments and simulations provided in Figure 3.10 the rotor makes several impacts with the stator and then starts to undergo backward dry-friction whirl.

From numerical simulations, it is observed that the presence of forward and backward whirling do not have a significant dependence upon the clearance between the rotor and the stator or the torsion stiffness. In general, the rotor is likely to undergo backward whirling motions for high values of friction and exhibit forward whirling motions for low values of friction. For friction values between the high and low values, the rotor may undergo either forward or backward whirling motions. For this range of friction, the steady-state response is found to be largely dependent

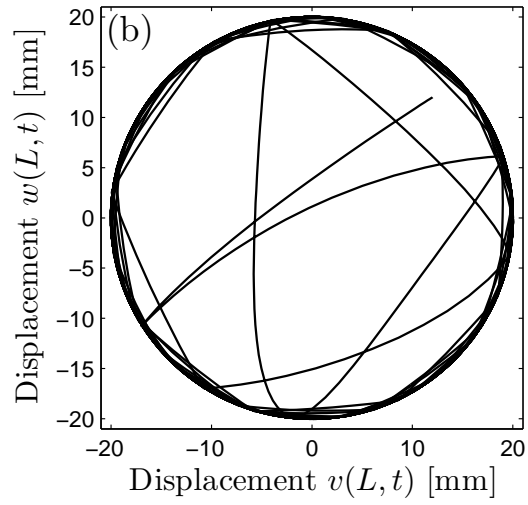
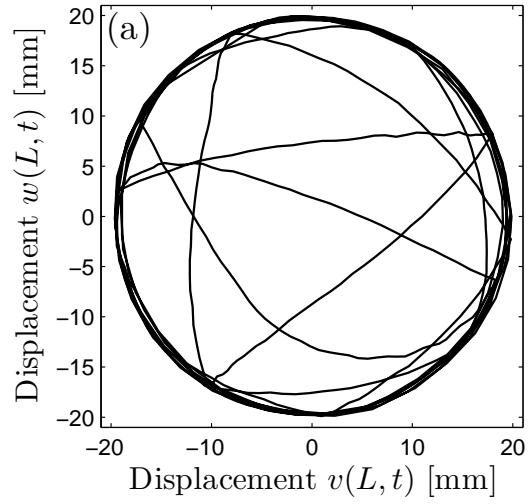


Figure 3.10: Comparisons for the same input parameters: (a) experimental results and (b) numerical results.

upon initial conditions for the lateral motions. Additional parametric studies related to initial conditions and friction of two different rotor-stator systems may be found in the works of Liao, Vlajic, Karki, and Balachandran (2012) and Li and Paidoussis (1994).

3.4.2 Torsional vibrations during forward and backward whirl motions

3.4.2.1 Forward whirling

The Fourier spectra of the torsional displacement generated through the numerical studies while the rotor undergoes forward whirling for a range of driving speeds are presented in Figure 3.11. Again, the spectra have been normalized using the scheme mentioned earlier. For low driving speeds, the amplitude of response is small and occurs at $2f_d$. However, as the driving speed is increased and nears the torsional natural frequency, the first resonance is excited and the response occurs at a combination of f_t and $2f_d$. It is noted that the current structure and force-interaction model do not capture the drive speed f_d component as well as the third order and higher harmonics. The f_d component in the experimental arrangement likely originates from non-ideal boundary conditions which are not considered in the system model, such as a small eccentricity of the chuck. Two segments of Figure 3.11 are provided in Figure 3.12 along with the relative speed time histories for 50 and 51 RPM drive speeds. The Fourier transforms of the data presented in Figure 3.12(a) and (b) are given in Figure 3.12(c) and (d), respectively. At a drive speed

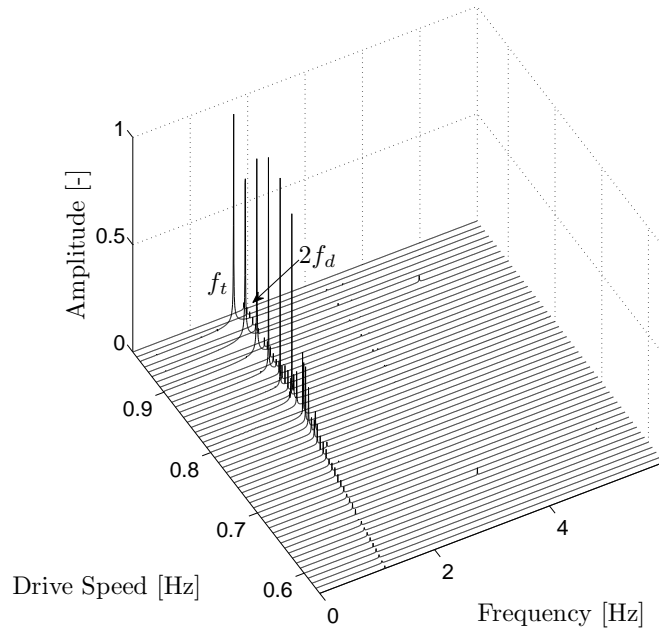


Figure 3.11: Normalized Fourier spectra of the simulated torsional displacement for forward whirling with stator contact.

of 50 RPM, the mean relative speed is approximately 0.5 m/s with a small peak-to-peak amplitude of 0.06 m/s, and oscillations occur at a frequency of $2f_d$. However, with increase of the speed to 51 RPM, the first torsional mode is excited and the amplitude of the torsional displacement and relative speed both become large. Here, the amplitude of the torsional displacement is bounded by the chosen friction force model, once the lower amplitude of the relative speed reaches 0 m/s.

3.4.2.2 Backward whirling

The normalized Fourier spectra of the torsional displacement generated through the numerical studies while the rotor undergoes backward whirling are shown in Figure 3.13. As with the experiments, the strongest component of response occurs at

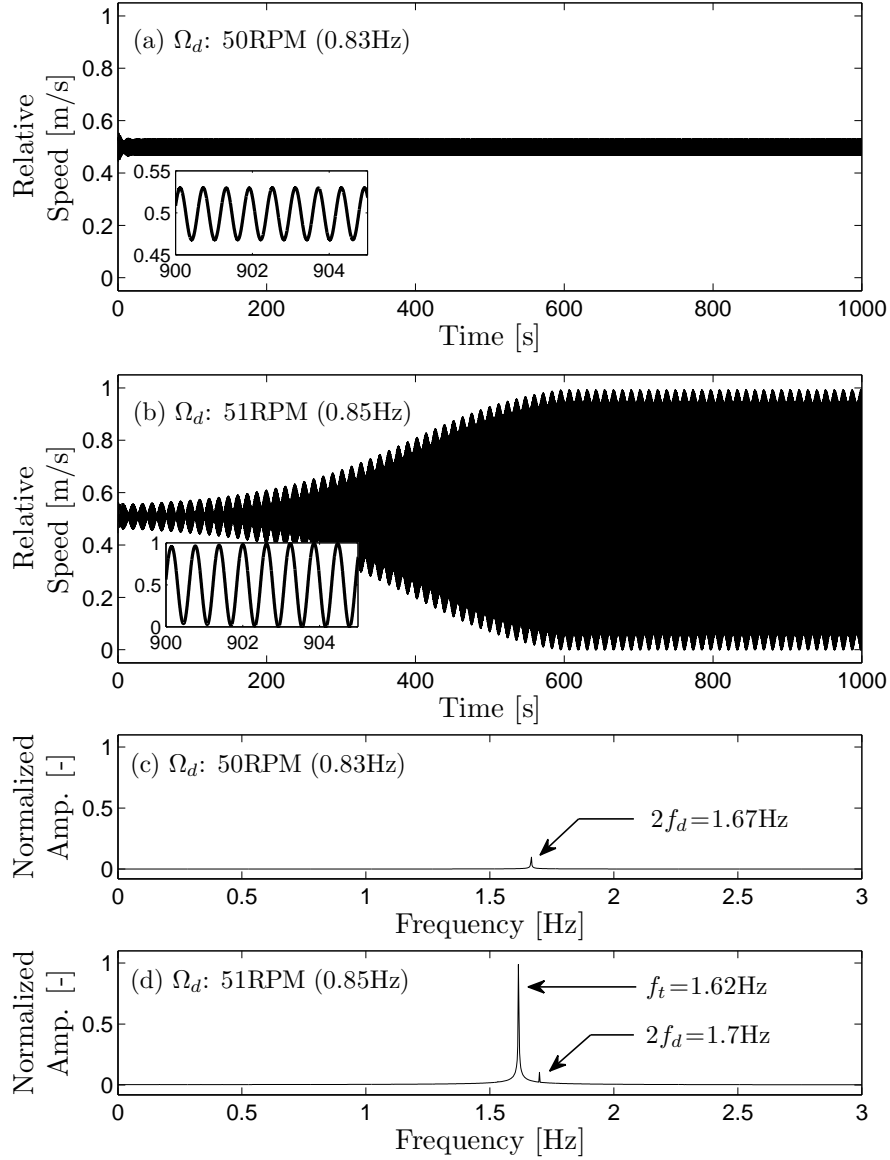


Figure 3.12: Two typical system responses for forward synchronous whirling: (a) Relative speed for 50 RPM, (b) relative speed for 51 RPM, (c) Fourier spectra of the steady-state torsion displacement for 50 RPM, and (d) Fourier spectra of the steady-state torsion displacement for 51 RPM.

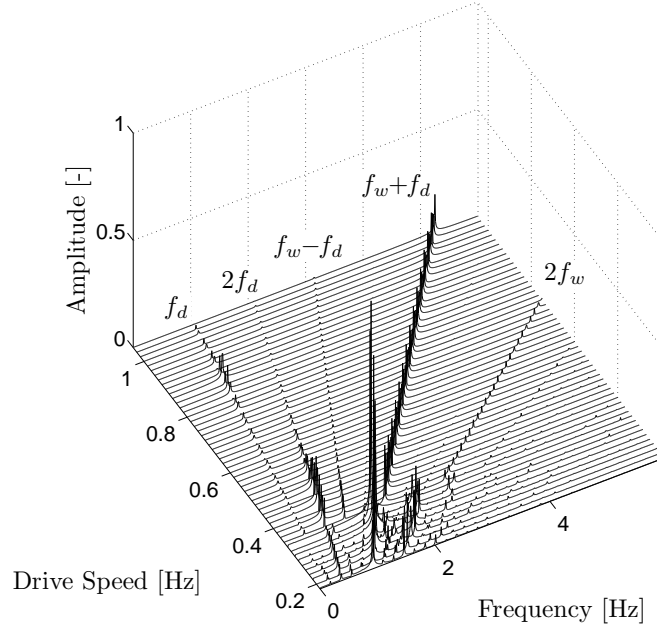


Figure 3.13: Normalized Fourier spectra of the simulated torsional displacement for backward whirling with stator contact.

$f_w + f_d$, and other contributions at f_d and $f_w - f_d$ also exist. The simulation results also indicate frequency components at $2f_w$ and $2f_d$, which are not seen in the experiments. The simulations are not able to capture the contributions of f_w , $f_w + 2f_d$, and $2(f_w + f_d)$ as seen in Figure 3.6.

Two segments at 13 RPM and 34 RPM of Figure 3.13 are given in Figure 3.14. Here, expanded sections between 900 and 910 seconds are provided to illustrate the nature of the response. It is noted that the approximate amplitudes of the relative speed for cases shown in Figure 3.14(a) and (b) are maintained for the entire duration of the simulation. As expected for dry-friction whirling, the mean of the relative speed is approximately zero. Stick-slip oscillations are visible in Figure 3.14(a) and (b); these motions excite several frequencies that are shown in Figure 3.14(c) and (d), respectively. The sticking phase occurs when the relative speed is approximately

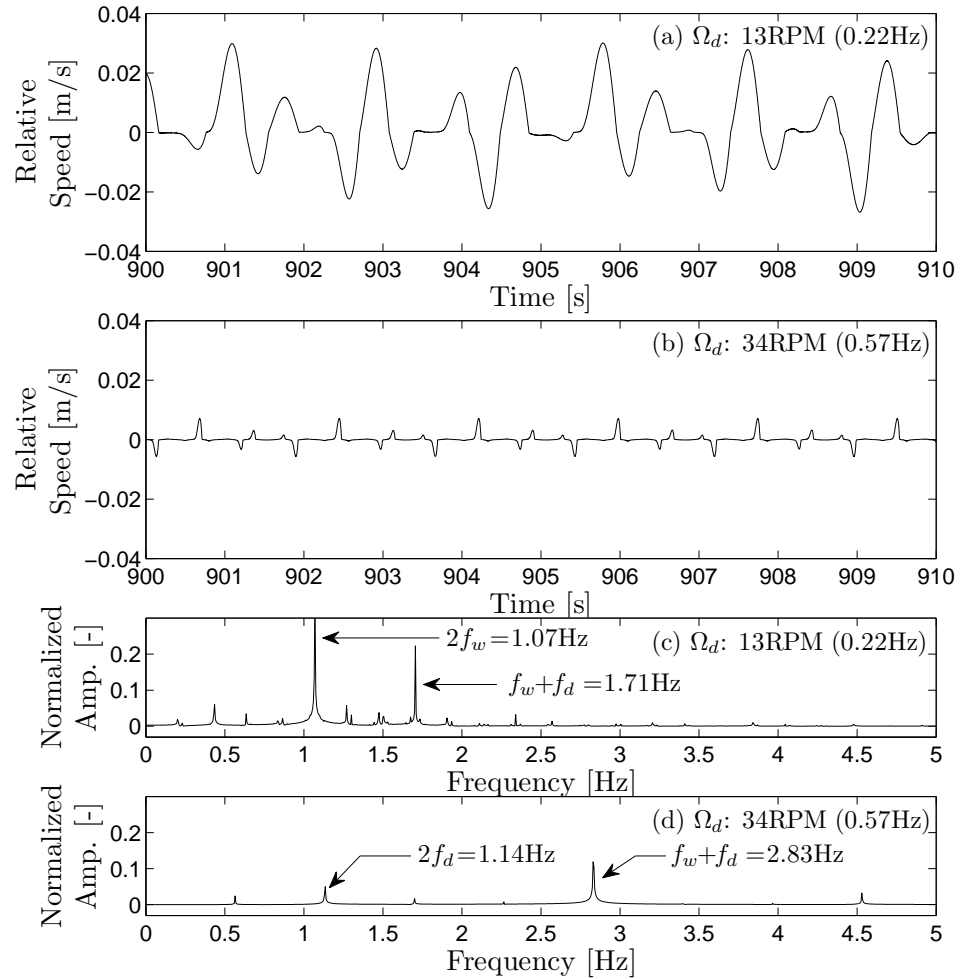


Figure 3.14: Two typical system responses for backward, dry-friction whirling: (a) Relative speed for 13 RPM, (b) relative speed for 34 RPM, (c) Fourier spectra of the steady-state torsion displacement for 13 RPM, and (d) Fourier spectra of the steady-state torsion displacement for 34 RPM.

zero, and the slip phase occurs when the relative speed is non-zero. At low speeds, the dominating components occur at $f_w + f_d$ and $2f_w$, while at high speeds major contributions occur at $f_w + f_d$ and $2f_d$.

3.5 Further reduced-order modeling and analysis

Following a procedure that was done in Section 2.3.2, and originally outlined in Vlajic, Liu, Karki, and Balachandran (2013); Vlajic, Karki, and Balachandran (2013), the system of equations given by equations (3.19)-(3.21) are reduced to a single nonlinear differential equation which is meant for studying the torsional motions during steady-state whirl. For constant whirl frequencies, the lateral motions of the rotor at $x = L$ may be prescribed as

$$v(L, t) = (\delta + \delta_p) \cos(\omega t + \phi_o) \approx \delta \cos \omega t \quad (3.31a)$$

$$w(L, t) = (\delta + \delta_p) \sin(\omega t + \phi_o) \approx \delta \sin \omega t \quad (3.31b)$$

where the penetration depth δ_p of the rotor into the stator is approximately zero. Considering small torsional deformations, the respective Taylor series expansions are carried out with the trigonometric terms in Θ , in a manner similar to that as equations (2.16) and (2.15). These expansions are substituted into the governing equations, and the following reduced-order equation is obtained to focus on the torsion dynamics:

$$c_1 \ddot{\Theta} + c_2 \dot{\Theta} + [c_3 + \phi_\theta(L) m \epsilon \delta \omega^2 \cos((\omega - \Omega)t)] \Theta = c_4 \omega^2 \sin(2\omega t) + \phi_\theta(L) m \epsilon \delta \omega^2 \sin((\omega - \Omega)t) + \phi_\theta(L) F_{tan} R \quad (3.32)$$

As was done earlier, the normal force is found in terms of the reaction force as the rotor whirls in contact with the stator. This approximate form is taken to be

$$F_{norm} \approx M\delta\omega^2 - K_{eq}\delta \quad (3.33)$$

where it has been assumed that $\delta(M + m) \gg me$ and K_{eq} is the equivalent stiffness of shaft. This equation is given consideration in the remaining sections for both forward and backward whirling.

3.5.1 Forward whirling

As previously mentioned, in the special case of forward whirling $\omega \approx \Omega$, equation (3.32) can be written as

$$c_1\ddot{\Theta} + c_2\dot{\Theta} + [c_3 + \phi_\theta(L)me\delta\omega^2] \Theta = c_4\omega^2 \sin(2\omega t) - \phi_\theta(L)F_{tan}R \quad (3.34)$$

Equation (3.34) has interesting features which are explained next. As discussed in Section 2.4, equation (3.34) has a centrifugal stiffening term. However, due to the low drive speeds in the given experiment, this effect is small and unmeasurable. In other experiments at high drive speeds, researchers have observed a stiffening effect during steady whirl with constant stator contact (Diangui, 2000). The reduced-order equation also has an external forcing frequency of $2\Omega = 2\omega$, which originates solely from the gyroscopic coupling terms in equations (3.19)-(3.21). In the absence of friction, $F_{tan} = 0$, equation (3.34) takes the form of a linear oscillator with harmonic forcing, associated with which a resonance will occur if $2\Omega \approx \omega_t = \sqrt{\frac{c_3 + \phi_\theta(L)me\delta\omega^2}{c_1}} \approx \sqrt{\frac{c_3}{c_1}}$. This resonance behavior is apparent in

both the experimental results shown in Figure 3.5 and in the results obtained from simulations of the full model (equations (3.19)-(3.21)) shown in Figure 3.11, as well as in the numerical results for the reduced-order model (equation (3.34)) provided in Figure 3.15. It is noted that near resonance, the original assumption of small angular deformations breaks down and equation (3.34) is no longer a reasonable approximation for the system dynamics in that region. Further, even in the absence of forcing originating from gyroscopic coupling (such as a planar rotor presented in Chapter 2, for instance), one can still obtain limit-cycle motions from the form of equation (3.34), as was found in Vljajic, Liu, Karki, and Balachandran (2013). Finally, a component at the torsional damped natural frequency is observed in the experiments shown in Figure 3.5, where the first torsion damped natural frequency is approximately equal to the undamped torsional frequency due to the light structural damping of the system. The response component at the first torsional natural frequency is not apparent in the simulations as the static coefficient of friction value was selected to be small. The response amplitude at this natural frequency is expected to be more prominent for other friction parameter values.

3.5.2 Backward whirling

During backward whirling, the whirl speed of the lateral vibrations is approximately $\omega \approx -\frac{R}{\delta}\Omega$, and equation (3.32) can be rewritten as

$$c_1\ddot{\Theta} + c_2\dot{\Theta} + [c_3 + \phi_\theta(L)m\epsilon\delta\omega^2 \cos(\alpha t)] \Theta = c_4\omega^2 \sin(2\omega t) - \phi_\theta(L)m\epsilon\delta\omega^2 \sin(\alpha t) + \phi_\theta(L)F_{tan}R \quad (3.35)$$

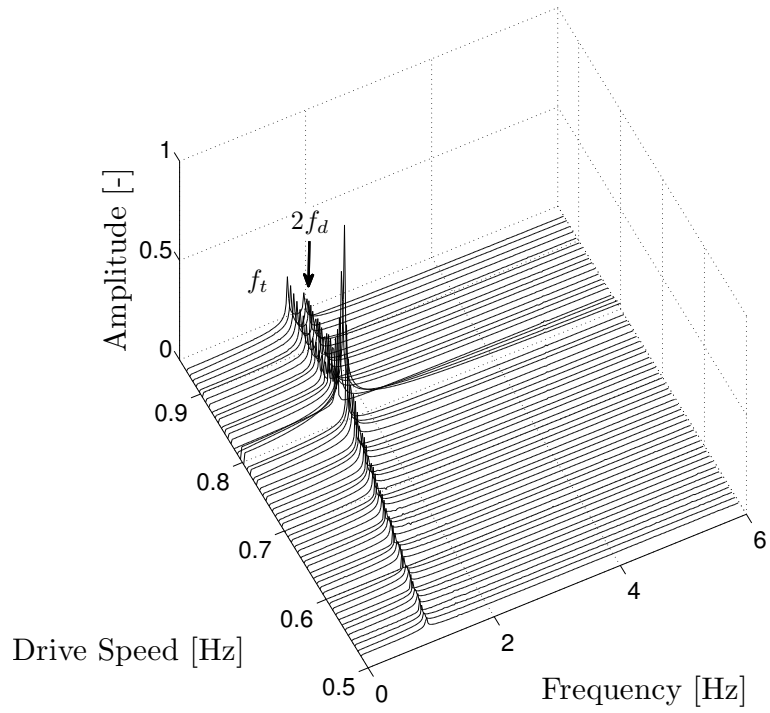


Figure 3.15: Torsion response spectra determined by equation (3.35) for forward whirling motions.

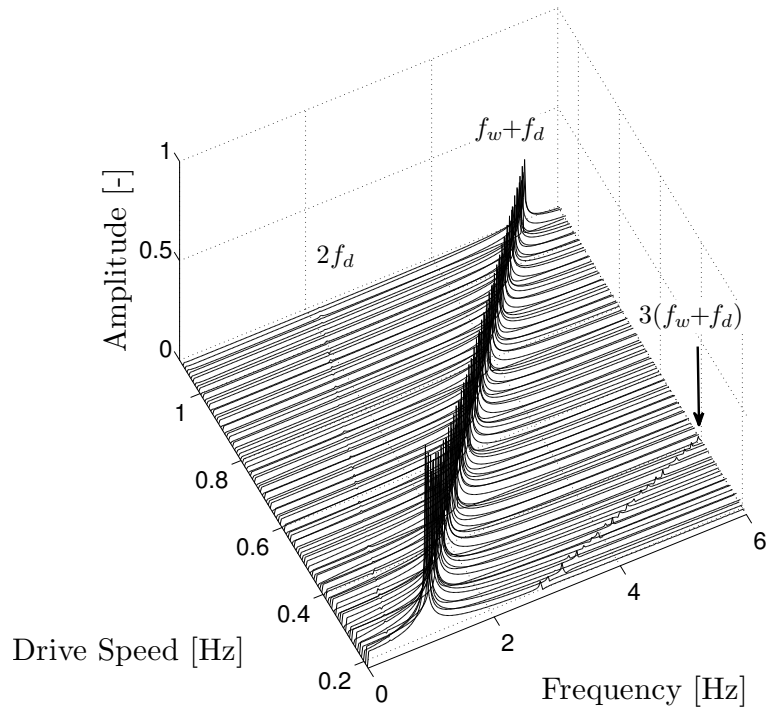


Figure 3.16: Torsion response spectra determined by equation (3.34) for forward whirling motions.

where

$$\alpha = (\omega - \Omega) = -\Omega\left(1 + \frac{R}{\delta}\right) \quad (3.36)$$

The frequency α physically represents the whirl speed, less the drive speed. This excitation frequency plays a role in equation (3.35) through external and parametric excitation terms. In both the experimental results shown in Figure 3.6, simulations of the full model (equations (3.19)-(3.21)) shown in Figure 3.13, and simulation results of the reduced-order model (equation (3.35)) provided in Figure 3.16, the response component at the whirl frequency plus the drive frequency is the dominant component (note that Fourier transforms presented here do not distinguish between positive and negative frequencies). Additionally, the external forcing at frequency 2ω from the gyroscopic coupling is still present in equation (3.35) and in the simulation results shown in Figure 3.13. However, this component is not discernibly large in the experimental results shown in Figure 3.6 (b), and in the numerical results obtained from the reduced-order equation and shown in Figure 3.16.

3.6 Summary

Within this chapter, a slender rotor with stator force-interactions has been studied. An experimental apparatus was able to demonstrate different rotor whirling motions, and the torsion response of the experimental structure was studied for continuous rotor-stator contact. A distributed-parameter structural model was derived

for the purpose of capturing phenomena observed in the experimental arrangement. The model presented in this chapter is able to account for more dynamic features (e.g. distributed parameter elements, gyroscopic coupling, gravitational effects) that were not considered in the simplified rotor model presented in Chapter 2. Numerical simulations of this model were able to predict the largest frequency components observed in the torsion response. Furthermore, under a given set of assumptions, the reduced-order model may be reduced to a single degree-of-freedom equation that is used to describe the torsional vibration response. Specific findings and contributions of this chapter are as follows:

1. The torsional motion is subject an external forcing frequency at twice the drive speed for non-planar rotors (i.e., rotors with gyroscopic effects) that are whirling at a constant rate. This external forcing effect has been found for both forward and backward whirling; therefore, a torsion resonance can occur when rotating the shaft at a frequency of half the torsional natural frequency.
2. When forward whirling with continuous stator contact, the effective external forcing and nonlinear friction may also excite response components at the first torsional natural frequency.
3. During backward whirling, the effective external forcing at twice the drive speed as well as external and parametric excitation at the whirl speed plus the drive speed can cause resonances in the torsional motions.

Chapter 4

Modal Analysis of Geometrically Exact Beams with Pre-stress and Curvature

In Chapters 2 and 3, the coupling between lateral and torsional motions of slender structures was explored. Within this chapter, the dynamics of slender structures with pre-stress and initial curvature are investigated. As pointed out earlier, slender structures are often manufactured in a straight configuration, but operate with an initial pre-stress in a deformation static configuration. This pre-stress and initial curvature can change the natural frequencies and mode shapes when in operation. For design and/or structural health monitoring purposes, it is desirable to predict the natural frequencies about this pre-stressed configuration. Previously in the literature, studies have focused on the dynamics of curved beams, such as arches or rings, with little or no pre-stress where the structure is restricted to special configurations (e.g., circular, elliptical, quadratic). Other studies have paid particular attention to the dynamics of buckled beams; however, the initial static displacement was relatively small (i.e., displacement on the order of the beam thickness). Within this chapter, the dynamics of curved beams are studied with large variable curvature and pre-stress in the static configuration. Additionally, the boundary conditions considered here allow for a broader class of static configurations than what has previously been published in the literature.

4.1 Geometrically exact model

The kinematics of the rod presented here follow the kinematic description that is outlined by Antman (2005). A graphical representation of the kinematics is provided in Figure 4.1. The rod is considered initially straight and unstressed in Euclidean space with mutually orthogonal unit vectors \mathbf{i} , \mathbf{j} , and \mathbf{k} . In the reference configuration, the rod spans the \mathbf{i} direction with arc length $s \in [0, L]$, where L is the length of the rod. Furthermore, at each point along the centerline of the rod let \mathbf{a} and \mathbf{b} be another set of mutually orthogonal unit vectors, where in the reference configuration $\mathbf{a} \equiv \mathbf{i}$ and $\mathbf{b} \equiv \mathbf{j}$. Let the vector \mathbf{r} describe the position of the centerline of the rod in the deformed configuration. The rod is allowed to undergo only deformations in the \mathbf{i} - \mathbf{j} plane, so that \mathbf{r} can be decomposed as

$$\mathbf{r}(s, t) \equiv \mathbf{r} = x \mathbf{i} + y \mathbf{j}. \quad (4.1)$$

The components of \mathbf{r} , $x(s, t) \equiv x$ and $y(s, t) \equiv y$, are the kinematic unknowns that define the position of the centerline of the rod in the \mathbf{i} and \mathbf{j} directions, respectively. Similarly, the position of the centerline of the rod may be determined by using another set of kinematic unknowns, namely the displacements from the reference configuration denoted by \mathbf{u} . The displacement field \mathbf{u} is comprised of the scalar quantities $u(s, t) \equiv u$ and $v(s, t) \equiv v$, which are the displacements of the centerline of the rod along the \mathbf{i} and \mathbf{j} directions. Hence,

$$\mathbf{r} = [s + u] \mathbf{i} + v \mathbf{j}. \quad (4.2)$$

Once the rod is deformed, the beam frame vectors \mathbf{a} and \mathbf{b} may be related back to the fixed frame by using the transformation

$$\mathbf{a}(s, t) \equiv \mathbf{a} = \cos \theta \mathbf{i} + \sin \theta \mathbf{j} \quad (4.3a)$$

$$\mathbf{b}(s, t) \equiv \mathbf{b} = -\sin \theta \mathbf{i} + \cos \theta \mathbf{j} \quad (4.3b)$$

where $\theta(s, t) \equiv \theta$ is the angle between \mathbf{a} and \mathbf{i} . It is convenient to decompose derivatives of \mathbf{r} with respect to the beam basis (\mathbf{a} - \mathbf{b} frame) as

$$\mathbf{r}_s \equiv \mathbf{r}' = \nu \mathbf{a} + \eta \mathbf{b}. \quad (4.4)$$

In equation (4.4) and others that follow, the prime superscript and s subscript are both used to denote the partial derivative with respect to s . The quantity $\eta(s, t) \equiv \eta$ is the shear strain. If the rod does not undergo shear, $\eta = 0$ and the axial strain of the rod is given by $\nu(s, t) \equiv \nu$. In the general case with the presence of shear, the axial strain of the rod is $\sqrt{\eta^2 + \nu^2}$. Additionally, the curvature of the beam is represented by $\mu \equiv \theta'$, which is the spatial rate of change of the rotation angle θ with respect to the arclength. It is noted that the curvature μ is not the mathematical curvature.

4.1.1 Governing equations of motion

As stated by Antman (2005), by carrying out force and moment balance, the governing equations of motion can be obtained as

$$\mathbf{n}_s + \mathbf{f} = \rho A \mathbf{r}_{tt} + \rho I \mathbf{b}_{tt} \quad (4.5a)$$

$$\mathbf{m}_s + \mathbf{r}_s \times \mathbf{n} + l \mathbf{k} = \rho I \mathbf{b} \times \mathbf{r}_{tt} + \rho J \mathbf{b} \times \mathbf{b}_{tt} \quad (4.5b)$$

Here, subscript t denotes the partial derivative with respect to time. Furthermore, the quantities ρA , ρI , and ρJ are the mass, first moment of mass, and second moment of mass, per unit reference length. These quantities are taken to be constant in this work along with a uniform cross-section and constant density. Since the centerline of the rod passes through the mass centers of the cross-section, then $\rho I = 0$. The vector \mathbf{n} is the resultant internal force, while \mathbf{m} is the resultant internal couple. Likewise, \mathbf{f} is the external force per unit reference length acting on the beam and l accounts for any external moments per unit reference length acting on the beam. As this is a planar beam, the internal force and internal couple take the form (Antman, 2005)

$$\mathbf{n}(s, t) \equiv \mathbf{n} = N \mathbf{a} + H \mathbf{b} \quad (4.6a)$$

$$\mathbf{m}(s, t) \equiv \mathbf{m} = M \mathbf{k}. \quad (4.6b)$$

In equation (4.6a), $H(s, t) \equiv H$ is the shear force (not necessarily the vertical shear), and $N(s, t) \equiv N$ is the resultant force in the \mathbf{a} direction. With this in mind, the component form of equations (4.5) in the inertial frame (i.e., projected onto the \mathbf{i} - \mathbf{j} - \mathbf{k} basis) with kinematic variables x , y , and θ yields the following:

$$(\partial_s N - \mu H) \cos \theta - (\partial_s H + \mu N) \sin \theta + \mathbf{f} \cdot \mathbf{i} = \rho A \partial_{tt} x \quad (4.7a)$$

$$(\partial_s N - \mu H) \sin \theta + (\partial_s H + \mu N) \cos \theta + \mathbf{f} \cdot \mathbf{j} = \rho A \partial_{tt} y \quad (4.7b)$$

$$\partial_s M + \nu H - \eta N + l \mathbf{k} = \rho J \partial_{tt} \theta. \quad (4.7c)$$

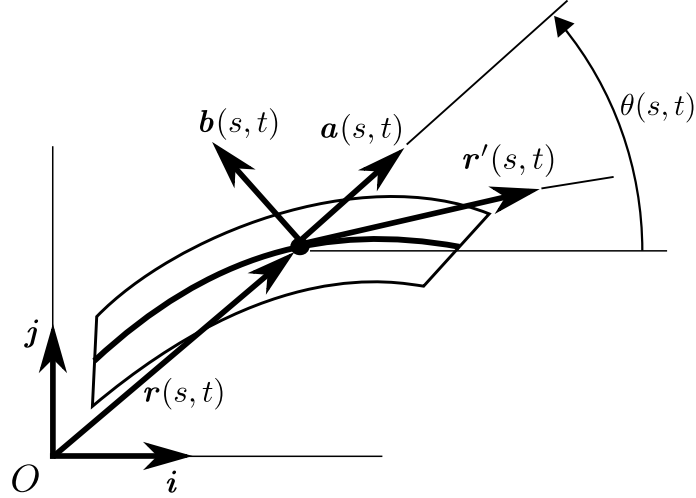


Figure 4.1: Description of the variables used to describe the motion of the rod structure.

4.1.2 Beam kinematics and governing equations

4.1.3 Static analysis

Dropping the time derivatives in equations (4.5), the equations governing the static configuration of the rod are given by

$$\mathbf{n}' + \mathbf{f} = \mathbf{o} \quad (4.8a)$$

$$\mathbf{m}' + \mathbf{r}' \times \mathbf{n} + l\mathbf{k} = \mathbf{o} \quad (4.8b)$$

Equation (4.8a) is an expression of force balance, while the equation (4.8b) is the expression for moment balance. The boundary conditions are prescribed as

$$\mathbf{r}(0) = \mathbf{o} \quad (4.9a)$$

$$\mathbf{r}(L) = x_L \mathbf{i} + y_L \mathbf{j} \quad (4.9b)$$

$$\theta(0) = 0 \quad (4.9c)$$

$$\theta(L) = \theta_L. \quad (4.9d)$$

Note, that either the force or the position may be prescribed in each direction at the boundary, but not both. Similarly, either the angle θ may be prescribed at the boundary or the moment, but not both. The boundary conditions presented here are different than those used in the previous work of Addessi, Lacarbonara, and Paolone (2005), where the forces were defined at $s = L$. In the absence of any external forces (including gravity) and external couples, $\mathbf{f} = \mathbf{o}$ and $l = 0$. Equations (4.8) reduce to

$$\mathbf{n}' = \mathbf{o} \quad (4.10a)$$

$$\mathbf{m}' + \mathbf{r}' \times \mathbf{n} = \mathbf{o} \quad (4.10b)$$

From equation (4.10a), it follows that the resultant internal force is a constant throughout the beam. After integration of the first of equations (4.10), the constant reaction forces are found to be

$$\mathbf{n} = N_1 \mathbf{i} + N_2 \mathbf{j}. \quad (4.11)$$

It follows by the transformation (4.3) that the resultant force components in the \mathbf{a} - \mathbf{b} frame are given by

$$N = N_1 \cos \theta + N_2 \sin \theta \quad (4.12a)$$

$$H = -N_1 \sin \theta + N_2 \cos \theta. \quad (4.12b)$$

The beams under consideration are assumed to be unshearable due to their slenderness and closed, uniform cross-section. This unshearability assumption is exercised through the constraint $\eta = 0$. Further, if the beam is also inextensible, then an additional constraint $\nu = 1$ may be imposed. It is noted that the boundary conditions

must be chosen judiciously when considering these assumptions and constraints. For instance, when exercising the inextensionality constraint, equations (4.8) and (4.10) may not have a physical solution for certain boundary conditions, such as $x_L > L$, $y_L = 0$, and $\theta_L = 0$; that is, boundary conditions that represent pure elongation of the beam.

The Bernoulli-Euler constitutive relation

$$M = EI\mu \tag{4.13}$$

where E is the Young's modulus and I is the area moment of inertia of the cross section of the rod, is assumed throughout this work. With this constitutive relation, and after substituting equation (4.11) into equation (4.10), assuming unshearability and inextensionality, and making use of the coordinate transformations given by equations (4.3), the following set of differential equations is obtained

$$M' - N_1 y' + N_2 x' = 0 \tag{4.14a}$$

$$M = EI\theta' \tag{4.14b}$$

$$x' = \cos \theta \tag{4.14c}$$

$$y' = \sin \theta. \tag{4.14d}$$

Equation (4.14a) is an expression of moment balance while (4.14b) is the Bernoulli-Euler constitutive relation. Similarly, (4.14c) and (4.14d) are constraints from the inextensionality and unshearability assumptions. Equations (4.14) constitute a fourth-order system with two unknown parameters, namely N_1 and N_2 . The fourth-order system with two unknowns is properly defined by the six boundary

conditions given by equations (4.9). This set of equations does not admit a trivial solution unless N_2 goes to zero as θ goes to zero. As such, this system is said to be *statically indeterminate*. Commonly, solutions to equations (4.14) with (4.9) are numerically determined. It will be shown later however, that for the circular and semi-circular boundary conditions, closed-form, algebraic solutions for x , y and θ are possible. For numerical purposes, it is convenient to integrate equation (4.14a). After performing this operation, the system of equations becomes

$$M - N_1 y + N_2 x + M_o = 0 \quad (4.15a)$$

$$M = EI\theta' \quad (4.15b)$$

$$x' = \cos \theta \quad (4.15c)$$

$$y' = \sin \theta \quad (4.15d)$$

Equations (4.15) now consist of a third order system with three kinematic unknown functions x , y , and θ along with three unknown constants N_1 , N_2 , and M_o . Here, there are three kinematic unknowns, and two constraints, thus making the problem properly determined using only one kinematic variable. Often in the literature, a linearization is performed so that $v' \approx \theta$ (Lacarbonara, 2013). However, this poses difficulties for circular trajectories where the slope becomes infinite. Therefore, θ is selected as the kinematic unknown.

To demonstrate the types of configurations the beam may exhibit, numerical solutions to equation (4.15) are provided in Figure 4.2 for four different boundary conditions. The rod is taken to have a uniform circular cross-section and the properties $R = 0.005m$, $EI = 0.625Nm^2$, $\rho A = 0.25kg/m$, and $L = 1m$. The solution

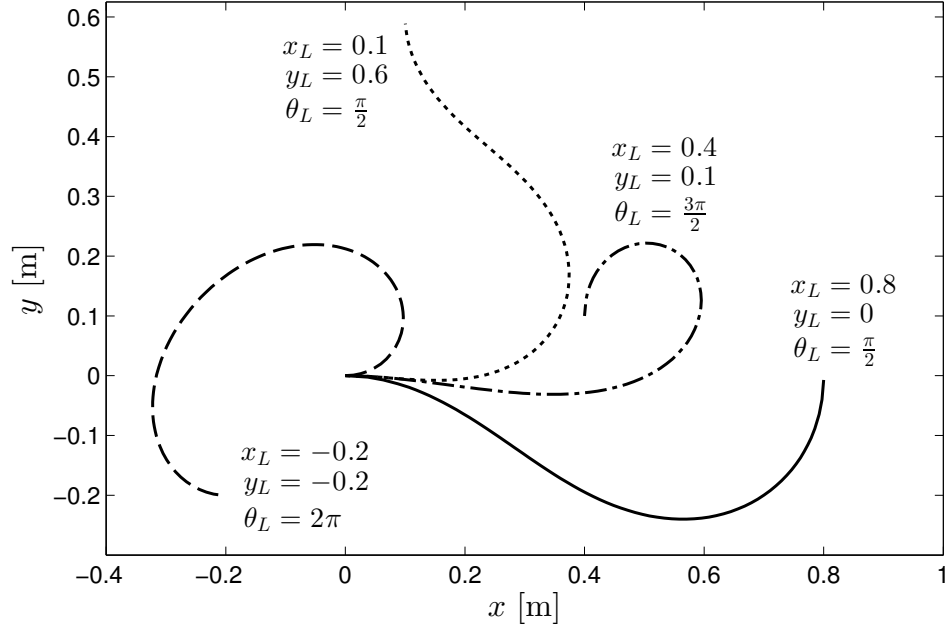


Figure 4.2: General static configurations admitted by equations (4.15). The solutions shown here have been numerically determined.

has been determined by numerically integrating the system (4.15) with boundary conditions (4.9) using `bvp4c` in MATLABTM. This routine makes use of a finite difference method with collocated polynomials that is suited for solving two-point boundary value problems with unknown parameters. Solutions are sought by iterating from an initial guess to the unknown functions and parameters; therefore, the configurations shown in Figure 4.2 for the given boundary conditions may not necessarily be unique. In the following section, a formulation is provided to determine the natural frequencies and mode shapes for motions about static solutions found from equations (4.15).

4.1.4 Modal analysis about the pre-stressed configuration

The dynamical system is cast into incremental form by using the static solution, denoted with superscript o , for the reference configuration. The incremental quantities are deviations from the static solution. The total displacement of the centerline is denoted $\check{\mathbf{r}}$, so that $\check{\mathbf{r}} = \mathbf{r}^o + \mathbf{u}$, where \mathbf{r}^o is the static solution obtained in the previous section and \mathbf{u} is the incremental displacement from the static configuration to the current configuration. Likewise, the total angular displacement may be decomposed as $\check{\theta} = \theta^o + \theta$. It is mentioned that incremental displacements of \mathbf{u} and θ should tend to zero as $s \rightarrow 0$ and $s \rightarrow L$, since the static configuration is prescribed at the boundaries. The unit vectors \mathbf{a}^o and \mathbf{b}^o are determined by the static configuration, while the unit vectors \mathbf{a} and \mathbf{b} are associated with the current configuration. Physical representations of these quantities are shown in Figure 4.3. In a similar manner, let $\mathbf{n} = N\mathbf{a} + H\mathbf{b}$ be the incremental force and M be the incremental moment. It follows that $\check{\mathbf{n}} = \mathbf{n} + \mathbf{n}^o$ is the total force, and $\check{M} = M + M^o$ is the total moment. After substituting the incremental expressions into the equations (4.5), the governing equations of motion for the incremental quantities accounting for pre-stress in the beam frame are given by (Lacarbonara, 2013)

$$\partial_s N - (\mu^o + \mu)H - \mu H^o + \mathbf{f}^o \cdot \Delta \mathbf{a} + \mathbf{f} \cdot \mathbf{a} = (\rho A \partial_{tt} \mathbf{u}) \cdot \mathbf{a} \quad (4.16a)$$

$$\partial_s H + (\mu^o + \mu)N + \mu N^o + \mathbf{f}^o \cdot \Delta \mathbf{b} + \mathbf{f} \cdot \mathbf{b} = (\rho A \partial_{tt} \mathbf{u}) \cdot \mathbf{b} \quad (4.16b)$$

$$\partial_s M + H + l = \rho J \partial_{tt} \theta \quad (4.16c)$$

where $\Delta \mathbf{a} = \mathbf{a} - \mathbf{a}^o$ and $\Delta \mathbf{b} = \mathbf{b} - \mathbf{b}^o$. If no external forces or external moments act on the rod, then $\mathbf{f} = \mathbf{o}$, $\mathbf{f}^o = \mathbf{o}$, and $l = 0$. Equation (4.16c) is used to solve for

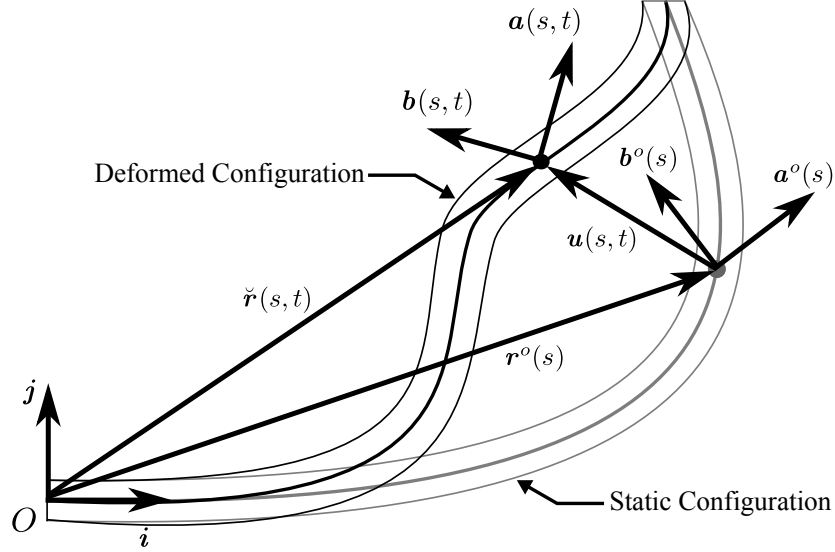


Figure 4.3: Description of the variables used to describe the motion of the beam about the pre-stressed configuration.

the incremental shear force H , and equation (4.16b) is used to solve for the force N . These quantities are substituted into equation (4.16a) to obtain the incremental dynamic equation of motion about the static configuration; that is,

$$\partial_s \left\{ \frac{1}{\mu + \mu^o} \left[(\rho A \partial_{tt} \mathbf{u}) \cdot \mathbf{b} - \partial_s (\rho J \partial_{tt} \theta - \partial_s M) - \mu N^o \right] \right\} - (\mu^o + \mu) (\rho J \partial_{tt} \theta - \partial_s M) - \mu H^o = (\rho A \partial_{tt} \mathbf{u}) \cdot \mathbf{a} \quad (4.17)$$

Governing Equations with Kinematic Variable θ

The variable θ is selected as the primary, kinematic unknown quantity, as was done to find the static solution. In this formulation, the components of $\check{\mathbf{u}}$ are decomposed with respect to the inertial frame by using the relation $\mathbf{u} = \check{u}\mathbf{i} + \check{v}\mathbf{j}$. It follows that \check{u} and \check{v} may be expressed as a function of θ from the unshearability

and inextensionality assumptions, $\partial_s \check{\mathbf{r}} = \mathbf{a}$, resulting in

$$\check{u}(s, t) = u^o(s) + u(s, t) = \int_0^s [-1 + \cos(\theta^o(\zeta) + \theta(\zeta))] d\zeta \quad (4.18a)$$

$$\check{v}(s, t) = v^o(s) + v(s, t) = \int_0^s \sin(\theta^o(\zeta) + \theta(\zeta)) d\zeta. \quad (4.18b)$$

The scalar form of equation (4.17) is

$$\begin{aligned} \partial_s \left\{ \frac{1}{\mu + \mu^o} \left[-\sin(\theta^o + \theta) \rho A \partial_{tt} u + \cos(\theta^o + \theta) \rho A \partial_{tt} v - \partial_s (\rho J \partial_{tt} \theta - \partial_s M) - \mu N^o \right] \right\} \\ - (\mu^o + \mu) (\rho J \partial_{tt} \theta - \partial_s M) - \mu H^o = \cos(\theta^o + \theta) \rho A \partial_{tt} u + \sin(\theta^o + \theta) \rho A \partial_{tt} v. \end{aligned} \quad (4.19)$$

On substituting equations (4.18a) and (4.18b) into equation (4.17), the following nonlinear integro-partial differential equation of motion is obtained:

$$\begin{aligned} \partial_s \left\{ \frac{1}{\mu + \mu^o} \left[-\rho A \left(\partial_{tt} \int_0^s \cos(\theta^o + \theta) d\zeta \right) \sin(\theta^o + \theta) \right. \right. \\ \left. \left. + \rho A \left(\partial_{tt} \int_0^s \sin(\theta^o + \theta) d\zeta \right) \cos(\theta^o + \theta) - \partial_s (\rho J \partial_{tt} \theta - \partial_s M) - \mu N^o \right] \right\} \\ - (\mu^o + \mu) (\rho J \partial_{tt} \theta - \partial_s M) - \mu H^o = \rho A \left(\partial_{tt} \int_0^s \cos(\theta^o + \theta) d\zeta \right) \cos(\theta^o + \theta) \\ + \rho A \left(\partial_{tt} \int_0^s \sin(\theta^o + \theta) d\zeta \right) \sin(\theta^o + \theta) \quad (4.20) \end{aligned}$$

with boundary conditions

$$\theta(0) = 0 \quad (4.21a)$$

$$\theta(L) = 0 \quad (4.21b)$$

and constraints

$$\int_0^L [-1 + \cos(\theta^o(\zeta) + \theta(\zeta))] d\zeta = 0 \quad (4.22a)$$

$$\int_0^L \sin(\theta^o(\zeta) + \theta(\zeta)) d\zeta = 0. \quad (4.22b)$$

If M is only a function of θ' and not of any higher-order derivatives, then equation (4.19) is a fourth-order system that is properly posed with two initial conditions for θ , and four spatial pieces of information given by boundary conditions (4.21) and nonlinear constraints (4.22). In general, the rotary inertia ρJ can be neglected since it is orders of magnitude smaller than the translational inertia terms dominated by ρA , and on the fact that solutions are small. This is justified on the basis that J is a function of the cross section radius to the fourth power, while the area A is function of the radius to the second power. The incremental quantity θ is assumed to be much smaller than the initial configuration θ_o and equation (4.19) is linearized with respect to θ after using the transformation $\theta \mapsto \epsilon\theta$ and the derivative $\frac{df(\epsilon\theta)}{d\epsilon}|_{\epsilon=0}$. Performing these operations leads to the following linear partial integro-differential equation of motion:

$$\begin{aligned} \partial_s \left\{ \frac{1}{\mu^o} \left[\rho A \left(\partial_{tt} \int_0^s \sin(\theta^o) \theta d\zeta \right) \sin(\theta^o) + \rho A \left(\partial_{tt} \int_0^s \cos(\theta^o) \theta d\zeta \right) \cos(\theta^o) \right. \right. \\ \left. \left. + \partial_{ss} \hat{M} - \mu N^o \right] \right\} + \mu^o \partial_s \hat{M} - \mu H^o = -\rho A \left(\partial_{tt} \int_0^s \sin(\theta^o) \theta d\zeta \right) \cos(\theta^o) \\ + \rho A \left(\partial_{tt} \int_0^s \cos(\theta^o) \theta d\zeta \right) \sin(\theta^o). \end{aligned} \quad (4.23)$$

In equation (4.23), \hat{M} is the linearized moment or couple, which is prescribed through the constitutive relations. The boundary conditions are given by equation (4.21) and the linearized constraints are

$$\int_0^L \sin(\theta^o(\zeta)) \cdot \theta(\zeta) d\zeta = 0 \quad (4.24a)$$

$$\int_0^L \cos(\theta^o(\zeta)) \cdot \theta(\zeta) d\zeta = 0. \quad (4.24b)$$

Although the system of equations given by equations (4.21), (4.23) and (4.24) is linear, finding an exact or approximate solutions poses several challenges. Equation (4.23) may be cast into weak-form, but trial functions should be selected that satisfy the mechanical data given by equations (4.21) and (4.24).

Equation of Motion with Kinematic Variable \bar{u}

To circumvent the system of partial integro-differential equations, a different kinematic unknown is selected at the primary variable. Here, the incremental displacement is defined with respect to the static configuration, and the displacement field is expressed by

$$\mathbf{u} = \bar{u}\mathbf{a}^o + \bar{v}\mathbf{b}^o. \quad (4.25)$$

If the amplitude of oscillation about the static equilibrium is small, the following dot products can be approximated as

$$\begin{aligned} \mathbf{a}^o \cdot \mathbf{a} &\approx 1, & \mathbf{a}^o \cdot \mathbf{b} &\approx -\theta, \\ \mathbf{b}^o \cdot \mathbf{a} &\approx \theta, & \mathbf{b}^o \cdot \mathbf{b} &\approx 1. \end{aligned} \quad (4.26)$$

Equations (4.25) and (4.26) are substituted into equation (4.17) in order to obtain the governing equation

$$\begin{aligned} \partial_s \left\{ \frac{1}{\mu^o + \mu} \left[\rho A \partial_{tt}(\bar{v} - \theta \bar{u}) - \partial_s(\rho J \partial_{tt}\theta - \partial_s M) - \mu N^o \right] \right\} \\ - (\mu^o + \mu)(\rho J \partial_{tt}\theta - \partial_s M) - \mu H^o = \rho A \partial_{tt}(\bar{u} + \theta \bar{v}). \end{aligned} \quad (4.27)$$

Furthermore, with the description of the displacement field while imposing the un-shearability assumption, it follows that the total stretch can be obtained as (Lacar-

bonara, 2013)

$$\check{\nu} = [(\nu^o + \bar{u}_s - \mu^o \bar{v})^2 + (\bar{v}_s + \mu^o \bar{u})^2]^{1/2}. \quad (4.28)$$

Similarly, the incremental angular displacement θ is then determined as

$$\theta = \arctan \left(\frac{\bar{v}_s + \mu^o \bar{u}}{\nu^o + \bar{u}_s - \mu^o \bar{v}} \right). \quad (4.29)$$

Under the assumption of small oscillations about the static equilibrium, and considering an inextensible beam ($\check{\nu} = 1$), equations (4.28) and (4.29) can be linearized to obtain

$$\bar{v} \approx \frac{1}{\mu^o} \partial_s \bar{u} \quad (4.30a)$$

$$\theta \approx \partial_s \bar{v} + \mu^o \bar{u}. \quad (4.30b)$$

It follows that the curvature may then be approximated in the form

$$\mu \approx \partial_s \left[\partial_s \left(\frac{1}{\mu^o} \partial_s \bar{u} \right) + \mu^o \bar{u} \right]. \quad (4.31)$$

On substituting equation (4.30) into equation (4.27), the following differential equation is obtained

$$\begin{aligned} \partial_s \left\{ \frac{1}{\mu^o + \mu} \left[\rho A \partial_{tt} \left(\frac{1}{\mu^o} \partial_s \bar{u} - \partial_s \left(\frac{1}{\mu^o} \partial_s \bar{u} \right) \bar{u} - \mu^o \bar{u}^2 \right) - \mu N^o \right. \right. \\ \left. \left. - \partial_s \left(\rho J \partial_{tt} \left(\partial_s \left(\frac{1}{\mu^o} \partial_s \bar{u} \right) + \mu_o \bar{u} \right) - \partial_s M \right) \right] \right\} \\ - (\mu^o + \mu) \left\{ \rho J \partial_{tt} \left[\partial_s \left(\frac{1}{\mu^o} \partial_s \bar{u} \right) + \mu_o \bar{u} \right] - \partial_s M \right\} - \mu H^o = \\ \rho A \partial_{tt} \left[\bar{u} + \frac{1}{\mu^o} (\partial_s \bar{u}) \partial_s \left(\frac{1}{\mu^o} \partial_s \bar{u} \right) + \bar{u} (\partial_s \bar{u}) \right]. \quad (4.32) \end{aligned}$$

If the material constitutive law that governs M is a function of μ , and no other higher spatial derivatives are involved, then equation (4.32) is a sixth-order partial differential equation which is properly defined with two initial conditions and

six boundary conditions. The boundary conditions may be determined from the kinematic approximations (4.30). They are given by

$$\begin{aligned}
\bar{u}(s=0) &= 0, & \bar{u}(s=L) &= 0 \\
\partial_s \bar{u}(s=0) &= 0, & \partial_s \bar{u}(s=L) &= 0 \\
\partial_{ss} \bar{u}(s=0) &= 0, & \partial_{ss} \bar{u}(s=L) &= 0
\end{aligned} \tag{4.33}$$

Linearizing equation (4.32) as discussed previously, the following linear, partial differential equation of motion is obtained.

$$\begin{aligned}
& \partial_s \left\{ \frac{1}{\mu^o} \left[\rho A \partial_{tt} \left(\frac{1}{\mu^o} \partial_s \bar{u} \right) - \partial_s \left[\partial_s \left(\frac{1}{\mu^o} \partial_s \bar{u} \right) + \mu^o \bar{u} \right] N^o \right. \right. \\
& \quad \left. \left. - \partial_s \left(\rho J \partial_{tt} \left(\partial_s \left(\frac{1}{\mu^o} \partial_s \bar{u} \right) + \mu_o \bar{u} \right) - \partial_s \hat{M} \right) \right] \right\} \\
& - \mu^o \left(\rho J \partial_{tt} \left(\partial_s \left(\frac{1}{\mu^o} \partial_s \bar{u} \right) + \mu_o \bar{u} \right) - \partial_s \hat{M} \right) - \partial_s \left[\partial_s \left(\frac{1}{\mu^o} \partial_s \bar{u} \right) + \mu_o \bar{u} \right] H^o = \rho A \partial_{tt} \bar{u}.
\end{aligned} \tag{4.34}$$

In order to determine the natural frequencies and mode shapes, the solution to equation (4.34) is assumed to be separable in space and time, with periodic temporal amplitude; that is,

$$\bar{u}(s, t) = U(s) e^{i\omega t}. \tag{4.35}$$

After substituting equation (4.35) into equation (4.34), assuming Bernoulli-Euler constitutive relations with constant EI , and neglecting rotary inertia ($\rho J = 0$), the

following ordinary differential equation is obtained.

$$\frac{d}{ds} \left\{ \frac{1}{\mu^o} \left[\frac{-\rho A \omega^2 dU}{\mu^o ds} - \frac{d}{ds} \left[\frac{d}{ds} \left(\frac{1}{\mu^o} \frac{dU}{ds} \right) + \mu^o U \right] N^o + EI \frac{d^3}{ds^3} \left[\frac{d}{ds} \left(\frac{1}{\mu^o} \frac{dU}{ds} \right) + \mu^o U \right] \right] \right\} + \mu^o EI \frac{d^2}{ds^2} \left[\frac{d}{ds} \left(\frac{1}{\mu^o} \frac{dU}{ds} \right) + \mu^o U \right] - \frac{d}{ds} \left[\frac{d}{ds} \left(\frac{1}{\mu^o} \frac{dU}{ds} \right) + \mu^o U \right] H^o = -\rho A \omega^2 U \quad (4.36)$$

Equation (4.36) is a sixth-order differential eigenvalue problem with unknown parameter ω , and six boundary conditions given by (4.33). Solutions to equation (4.36) are numerically determined in MATLAB by using the function `bvp4c`. Since equation (4.36) represents a homogeneous eigenvalue problem, the amplitude cannot be uniquely determined. In the numerical scheme, a moment proportional to the fourth-spatial derivative of U is prescribed to make the amplitude unique.

4.2 Experimental studies

The modeling presented earlier is validated in this section with the experimental arrangement, which is shown in Figure 4.4. A schematic of the experiment with coordinates is provided in Figure 4.5. The beam is made from aluminum (6061-T6) material, has a length of $1.506m$ and a circular cross-section with a $1.59mm$ radius. The top end of the beam (taken as the origin) is vertically secured at one end by using a three-jaw chuck. The opposite end of the rod (represented by coordinates x_L , y_L and θ_L) is secured horizontally with a clamping mechanism, such that the angle of the rod between each end is 90^0 . A complete list of experimental parameters along with their values is provided in Table 4.1. The clamping mechanism is mounted onto a linear bearing, which is actuated with an electro-dynamic shaker.

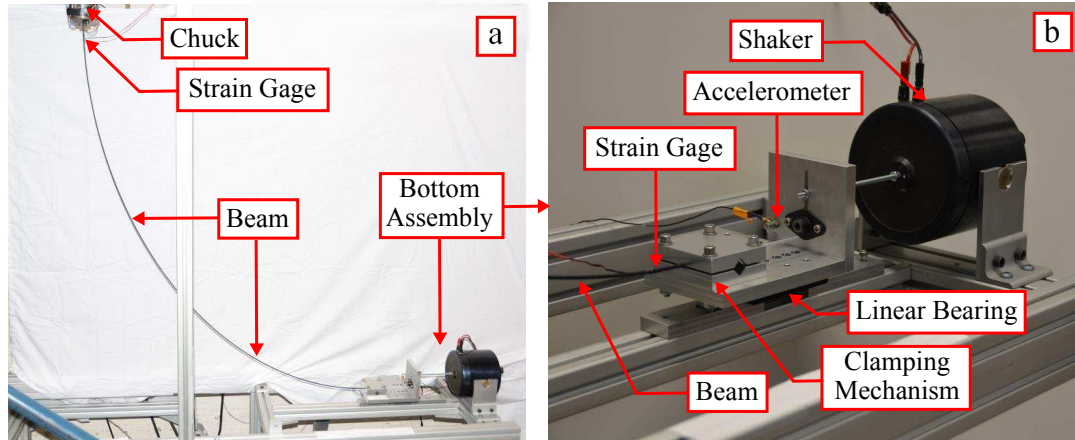


Figure 4.4: (a) Experimental arrangement used to determine the natural frequencies of a pre-stressed beam. (b) Detailed view of the bottom assembly.

The clamping mechanism is much stiffer than the beam, and is assumed to be rigid. Since the motions of the rigid clamping mechanism are prescribed, its inertial properties are not included in the modeling. Strain gages are mounted at both ends of the rod, along with an accelerometer that is mounted onto the clamping mechanism. The time histories of the strain gages and accelerometer are recorded by using a data acquisition system and personal computer. In order to determine the natural frequencies of the beam, white Gaussian noise is input into the shaker while the strain gage and accelerometer responses are recorded. Discrete Fourier transforms are performed on the strain and acceleration data that were collected over a period of 600 seconds at a sampling frequency of 5kHz. The resulting Fourier-transforms of the strain and acceleration responses were divided in order to obtain the strain response to the acceleration input frequency-response. The damped natural frequencies of the structure were then determined from the response spectrum, which is provided in Figure 4.6.

Once the damped natural frequencies were determined, the associated mode

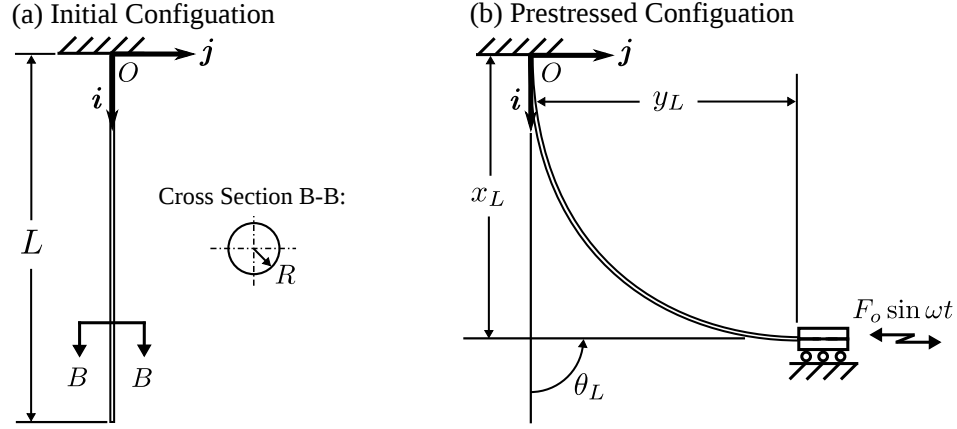


Figure 4.5: Schematic of the experimental arrangement used to study the dynamics of slender structures.

shapes were extracted with high-speed videography. The beam was excited at the desired frequency, and the response was recorded at 3000 frames per second (FPS) with a resolution of 1280×800 pixels. Each frame of the video was later post-processed in MATLAB to determine the displacement time histories of the beam by using a procedure that is briefly outlined here. First, an image is captured of the experimental arrangement without the beam, which is referred to as the *background image* in this section. In each frame of the video, the beam is accentuated by performing an image subtraction with the background image. The edges of the beam structure were determined with a gradient-based edge detection technique. Note that the mid-span of the beam was obstructed by a post which is necessary for the experimental apparatus. This obstructed portion of the beam structure is determined by converting the left and right-hand portions of the structure into polar coordinates, and curve fitting the result with a polynomial in the polar domain. The static configuration was fit with a fifth-order polynomial, while a sixth-order polynomial was chosen for the first mode. The order of the polynomial was increased by

one for each higher mode. The data were converted back into Cartesian coordinates and the pixel information was then converted into units of meters. In Figure 4.7, one image from the high-speed video with the tracked position of the beam (in red dots) determined by the image processing algorithm is shown.

4.3 Comparison of experimental results, theory, and finite element analysis

The list of natural frequencies obtained for the first eight modes of vibration from the data shown in Figure 4.6 are provided in Table 4.2 along with the predicted values from the model and the finite element method software ANSYSTM. In the finite element implementation, 500 quadratic beam elements (BEAM189) were selected to discretize the structure. The nonlinear geometry (NLGEOM) option was also activated. This option setting allows for large deformations, by using an updated corotational frame as outlined by Rankin and Brogan (1986). After the static configuration is determined, the results are used for an eigen-analysis with the PSTRESS option active to account for static pre-stress. The natural frequencies were determined by using a Block-Lanczos algorithm. It is noted that a convergence study was performed, and the natural frequencies calculated with 500 elements had less than 0.1% difference when the analysis was performed with 1000 elements. In the constitutive relation used in the model, the resultant couple is proportional to the curvature, through the Bernoulli-Euler constitutive relation $M = EI\mu$. This constitutive relation cannot be implemented in this finite element formulation; therefore a

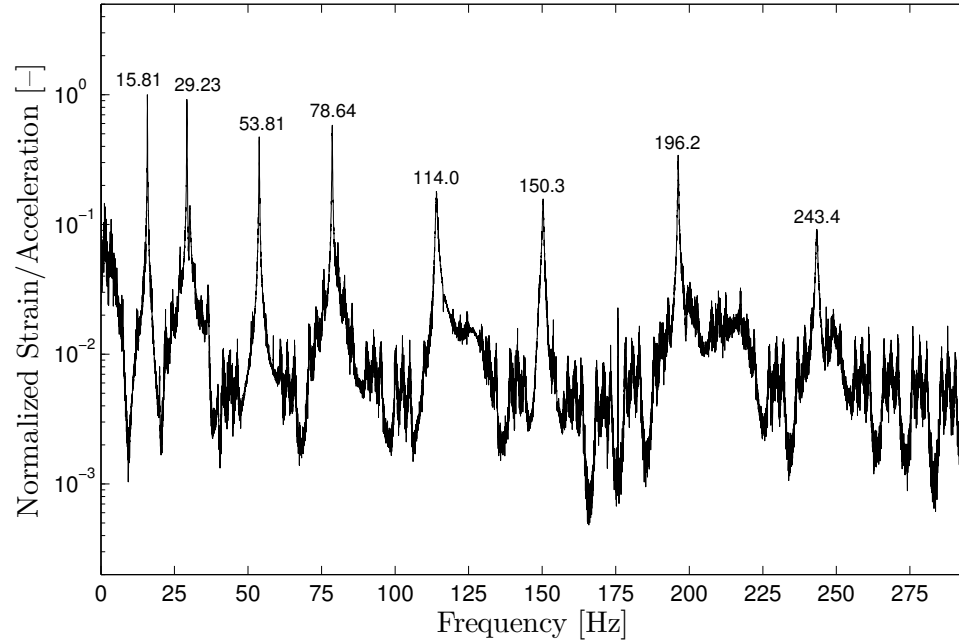


Figure 4.6: Normalized strain-acceleration response for the curved structure shown in Figure 4.4.

linear-isotropic material was chosen as the constitutive relation with properties that are provided in Table 4.1. The three assumptions of unshearability, inextensionality, and negligible rotary inertia have not been implemented in the finite element formulation; rather, they are only considered in the model. The experimental results, model and finite element predictions are in good agreement. The model and finite element predictions for the first natural frequency are below the experimental natural frequency by approximately 2%. For the remaining modes, the errors for both model and finite elements remain less than 2%. However, it is mentioned that this trend would not continue for all higher mode numbers and frequencies, since the effects of centerline or axial stretching will decrease certain natural frequencies. The effect of centerline stretching has not been considered in the current modeling since the body is assumed to be inextensible.

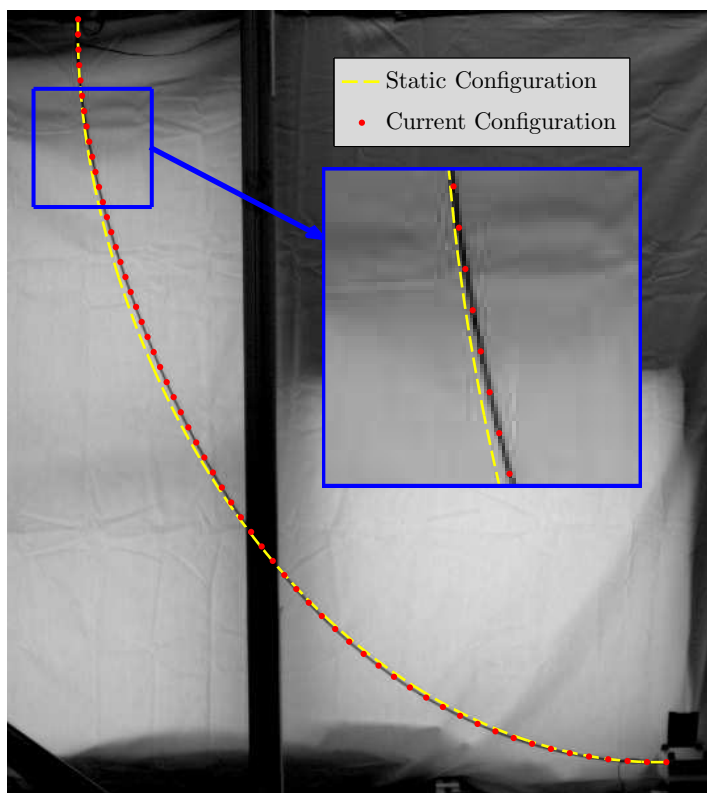


Figure 4.7: One frame of the video with the backlit structure in black, the static configuration (dashed line), and the estimated current configuration (dots) from the image processing.

Table 4.1: Experimental dimensions and parameters used in the model and finite element analysis. Superscript asterisks (*) denote tabulated parameters, while the remaining parameters and dimensions are measured quantities.

Parameter	Symbol	Value	Units
Modulus of Elasticity*	E	70	GPa
Possion's Ratio* (for ANSYS)	-	0.33	$[-]$
Mass Density*	ρ	2700	Kg/m^3
Length of Rod	L	1.506	m
Radius of Rod	R	1.59	mm
x Location of Rod End	x_L	1.09	m
y Location of Rod End	y_L	0.833	m
Angle of Rod End about \mathbf{k}	θ_L	$\pi/2$	rad

Table 4.2: Experimentally observed natural frequencies of the curved structure compared with predictions from the model and finite element model.

Mode	Experiment [Hz]	Theory [Hz]	Difference [%]	FEA [Hz]	Difference [%]
1	15.81	15.55	-1.64	16.08	1.71
2	29.23	29.25	0.07	29.79	1.92
3	53.81	54.21	0.74	54.69	1.64
4	78.64	79.64	1.27	80.03	1.77
5	114.0	115.6	1.40	116.0	1.76
6	150.3	152.4	1.40	152.6	1.55
7	196.2	199.6	1.73	199.8	1.83
8	243.4	247.7	1.77	247.5	1.67

The static configuration and the first three mode shapes of the experiment are compared in Figure 4.8, where the experimental mode shapes and static configuration have been determined by using the image processing algorithm discussed previously. The displacements of the fourth and higher modes are small, and tracking the displacement of the string with the image processing algorithm became unreliable. The experimentally determined mode shapes, model and finite element predictions are in good agreement for the static configuration shown in Figure 4.8(a). There are some discrepancies between the experimentally observed mode shapes and predictions. These discrepancies may originate from a variety of different sources. For instance, the physical beam also has some intrinsic damping, which was not considered in the modeling and analysis, and perfectly clamped-clamped boundary conditions are difficult to realize experimentally. Furthermore, differences may be attributed to errors in the measurement, since optical lenses can distort planar objects.

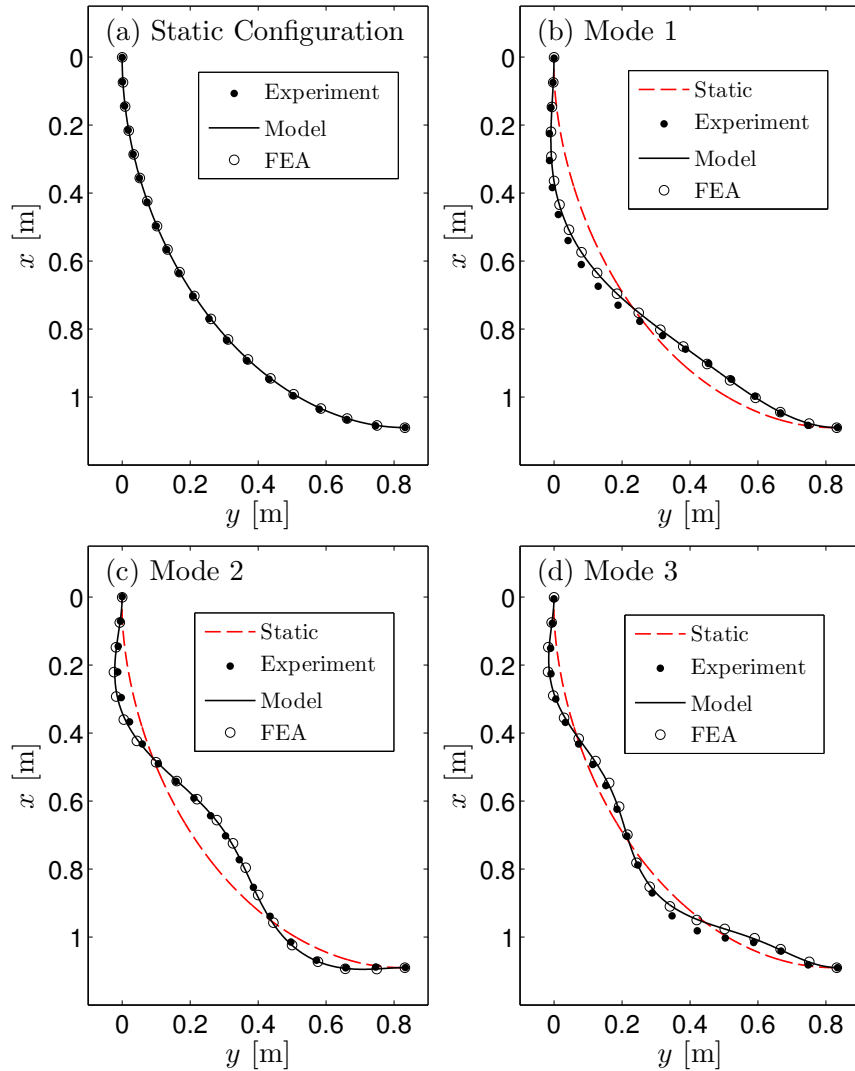


Figure 4.8: Static configuration and mode shapes from the experiments (black dots), the model formulation (solid black line) and finite element results. (a) Static configuration, (b) mode 1, (c) mode 2, and (d) mode 3.

4.4 Summary

Within this chapter, a geometrically exact modeling approach has been outlined in order to predict the natural frequencies of slender beams with prescribed boundary conditions. The configurations of the beam are able to undergo large deformations with variable curvature. The boundary conditions considered here allow for a broader class of static configurations for the deformed rod than what has previously been studied. The predictions from the model have been validated by using an experimental apparatus. Comparisons have also been made with predictions from nonlinear finite element software.

Chapter 5

Summary of Contributions and Recommendations for Future Studies

5.1 Coupled motions in rotor systems

Contributions

Coupled torsional and lateral motions of slender structures were explored in Chapters 2 and 3 with emphasis on slender rotating structures. In Chapter 2, the modified Jeffcott rotor with continuous stator contact and torsional deformations was studied for constant whirling motions. A reduced-order equation was derived, with the aim of capturing the torsional motions for a constant rotor whirl rate and amplitude. Particular attention was given to torsional vibrations while a rotor was in continuous contact with a stator. Analysis of this reduced-order equation indicates the presence of a centrifugal stiffening effect on the torsional motion, and reveals that torsional vibrations are unlikely to exist during forward synchronous whirl with stator contact. If torsional oscillations are present during forward synchronous whirl, they are likely excited through a Hopf instability. Furthermore, the reduced-order equation was analyzed for both “low-speed” and “high-speed” whirling motions. During high-speed backward whirling, analysis indicates that high-frequency forcing effectively acts to smoothen out discontinuous friction forces arising from stator contact and contributes to a centrifugal stiffening effect on the slow scale motion.

In Chapter 3, slender rotating structures were investigated experimentally, numerically and analytically. The experimental arrangement was able to demonstrate characteristic whirling motions, and the torsion response was studied for whirling motions during continuous stator contact. A distributed-parameter structural model along with a rotor-stator force-interaction model was developed with the intent of capturing the phenomena observed in the experimental arrangement. Comparisons were made between the torsion response during whirling for the experiment and the model. It was shown that the numerical model was able to predict the strongest response components of the torsion response. Furthermore, a single degree-of-freedom reduced-order model was derived that gave insight into the physics and origins of the components observed in the frequency of the torsion response. Numerical simulations of this reduced-order equation were in good agreement with experimental observations and numerical simulations of the higher-order system. During forward whirling, analysis showed an autonomous forcing component at twice the drive frequency for forward whirling originating from gyroscopic coupled terms with lateral motions, as well as the centrifugal stiffening effect found in the simplified system in Chapter 2. During backward whirling motion, an external and parametric excitation component exists at the whirl speed plus the drive speed.

Future studies

The coupling between torsional and lateral motions was explored in Chapters 2 and 3 under the assumption that only one mode of vibration contributed to the

displacement in each lateral and torsional direction. The effects of coupling between higher-order lateral and torsional vibration modes have yet to be addressed. When combination frequencies of higher-order modes coincide with a lower-mode natural frequency, certain resonances may occur (Anderson, Nayfeh, and Balachandran, 1996). Additionally, few researchers have studied the effects of axial, torsional, and later coupling in slender structures. The inclusion of high-order modes and axial motions into the coupling of the structure is still an open area of research that is not yet fully understood. The effects of these two areas become more pronounced as the aspect ratio of the structure increases further.

In both Chapters 2 and 3, the rotor was assumed to whirl at a constant speed. If the rotor does not whirl at a constant rate (for instance, due to stick-slip vibrations), then the torsion response will change. The high-frequency analysis presented in Chapter 2 can be extended to include the time scales of the lateral motions. However, because of the large number of states of the system, numerical methods should be employed.

During forward whirling motions, the point of contact on the rotor is constant for a fixed drive speed. However, during backward whirling the location of the point of contact moves to different locations along the periphery of the rotor. This type of physical behavior may be suitable for hybrid dynamical models. These types of models have not been given large consideration in the area of rotor dynamics.

5.2 Geometrically exact structures

Contributions

In Chapter 4 of this dissertation, the static configuration and dynamic modal analysis of geometrically exact beams subject to large pre-stress and curvature were studied experimentally, numerically, and analytically. The boundary conditions for the beams under consideration within Chapter 4 allow for a broad class of static configurations in comparison to what has previously been presented in the literature. The static configuration, natural frequencies, and mode shapes predicted by the theory were verified with an experimental arrangement. Predictions of these quantities were also compared to a nonlinear finite element formulation. The differences between the predicted natural frequencies for the theoretical model, finite elements, and experiments were less than 2%. Furthermore, under special boundary conditions, the governing beam equations presented in Chapter 4 may be cast into the classical equations for circular arches as was shown in Appendix D. For this special case of semi-circular and circular configurations, a closed form solution for the static configuration, mode shapes and natural frequencies are possible.

Future studies

The three main assumptions employed within the geometrically exact beam model presented in Chapter 4 are inextensibility (i.e., no centerline stretching or contraction), unshearability, and negligible rotary inertia. For the slender structures and the boundary conditions considered here, these assumptions are justified

and reasonable; however, for smaller aspect ratios and other boundary conditions, these assumptions may no longer be valid. For instance, if the beam or rod has boundary conditions which exert tension throughout the structure, then the effects of centerline stretching play a large role in the system response. Additionally, some researchers have shown that the effects of centerline stretching can lower the natural frequencies of higher-order modes in ring and arch structures. This centerline stretching effect has not yet been studied for the boundary conditions presented here. In regard to shear and rotary inertia, as the aspect ratio of the beam *decreases* (i.e., as the length to diameter ratio becomes smaller), these two effects will have a larger impact on the natural frequencies of the system. Although, the contributions of these three effects have been studied for arches and rings, few efforts have studied their effects for beams with large pre-stress and variable curvature, such as the beams considered in Chapter 4. Additionally, in scenarios where lumped masses are placed along the curved structure, such as stabilizer collars used in horizontal drilling, the rotary inertia effects will become more pronounced. The validity of these three assumptions for the boundary conditions considered within this dissertation is still an unaddressed area of research.

Appendix A

Derivation of 1-2-3 Euler Angles and Angular Velocity

The relationship between the orientation of the local coordinate frame to the fixed coordinate frame in Section 3.3.1 is given by the use of 1-2-3 Euler angles as follows. In order to transform from the local frame to the fixed frame, the fixed frame is rotated an amount β about the \mathbf{i} direction, yielding an intermediate frame $\mathbf{i}_1\mathbf{j}_1\mathbf{k}_1$. The 3×3 special orthogonal matrix for this transformation is

$$\begin{Bmatrix} \mathbf{i}_1 \\ \mathbf{j}_1 \\ \mathbf{k}_1 \end{Bmatrix} = [R_\beta] \begin{Bmatrix} \mathbf{i} \\ \mathbf{j} \\ \mathbf{k} \end{Bmatrix} \quad \text{where } [R_\beta] = \begin{bmatrix} 1 & 0 & 0 \\ 0 & C_\beta & -S_\beta \\ 0 & S_\beta & C_\beta \end{bmatrix} \quad (\text{A.1})$$

The notations $C_{(\cdot)}$ and $S_{(\cdot)}$ denote the $\sin(\cdot)$ and $\cos(\cdot)$ functions, respectively. Likewise, the $\mathbf{i}_1\mathbf{j}_1\mathbf{k}_1$ frame is then rotated by ψ about the \mathbf{j}_1 direction to give the second intermediate frame $\mathbf{i}_2\mathbf{j}_2\mathbf{k}_2$. This transformation is given by the following matrix operation

$$\begin{Bmatrix} \mathbf{i}_2 \\ \mathbf{j}_2 \\ \mathbf{k}_2 \end{Bmatrix} = [R_\psi] \begin{Bmatrix} \mathbf{i}_1 \\ \mathbf{j}_1 \\ \mathbf{k}_1 \end{Bmatrix} \quad \text{where } [R_\psi] = \begin{bmatrix} C_\psi & 0 & S_\psi \\ 0 & 1 & 0 \\ -S_\psi & 0 & C_\psi \end{bmatrix} \quad (\text{A.2})$$

Last, a rotation of α about the \mathbf{k}_2 direction gives the orientation of the local coordinate frame $\mathbf{i}_3\mathbf{j}_3\mathbf{k}_3$. This rotation is given by

$$\begin{Bmatrix} \mathbf{i}_3 \\ \mathbf{j}_3 \\ \mathbf{k}_3 \end{Bmatrix} = [R_\alpha] \begin{Bmatrix} \mathbf{i}_2 \\ \mathbf{j}_2 \\ \mathbf{k}_2 \end{Bmatrix} \quad \text{where } [R_\alpha] = \begin{bmatrix} C_\alpha & S_\alpha & 0 \\ -S_\alpha & C_\alpha & 0 \\ 0 & 0 & 1 \end{bmatrix} \quad (\text{A.3})$$

Therefore, the total transformation from the \mathbf{ijk} frame to the $\mathbf{i_3j_3k_3}$ frame is then the multiplication of each individual rotation as

$$\begin{Bmatrix} \mathbf{i_3} \\ \mathbf{j_3} \\ \mathbf{k_3} \end{Bmatrix} = [R_\alpha][R_\psi][R_\beta] \begin{Bmatrix} \mathbf{i} \\ \mathbf{j} \\ \mathbf{k} \end{Bmatrix} \quad (\text{A.4})$$

In contrast, the transformation from $\mathbf{i_3j_3k_3}$ frame to the \mathbf{ijk} frame is then

$$\begin{Bmatrix} \mathbf{i} \\ \mathbf{j} \\ \mathbf{k} \end{Bmatrix} = ([R_\alpha][R_\psi][R_\beta])^T \begin{Bmatrix} \mathbf{i_3} \\ \mathbf{j_3} \\ \mathbf{k_3} \end{Bmatrix} = [R_\beta]^T [R_\psi]^T [R_\alpha]^T \begin{Bmatrix} \mathbf{i_3} \\ \mathbf{j_3} \\ \mathbf{k_3} \end{Bmatrix} \quad (\text{A.5})$$

The superscript T denotes the matrix transpose operation. In order to generate an expression for the kinetic energy, the angular velocity of the $\mathbf{i_3j_3k_3}$ frame is needed.

The angular velocity of each of the intermediate frames is

$$\boldsymbol{\omega} = \dot{\beta}\mathbf{i} + \dot{\psi}\mathbf{j}_1 + \dot{\alpha}\mathbf{k}_2 \quad (\text{A.6})$$

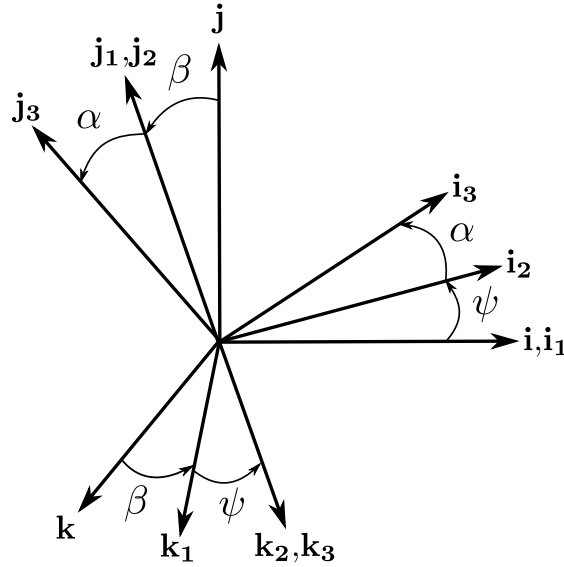


Figure A.1: Euler angles used to express the angular velocity of the structure.

Transforming the angular velocity into the $x_3y_3z_3$ coordinate frame, by using the rows of equations (A.1), (A.2), and (A.3) leads to

$$\begin{aligned}
 \boldsymbol{\omega} &= \omega_1 \mathbf{i}_3 + \omega_2 \mathbf{j}_3 + \omega_3 \mathbf{k}_3 \\
 &= (\dot{\beta} - \dot{\alpha} S_\psi) \mathbf{i}_3 + (\dot{\psi} C_\beta - \dot{\alpha} S_\beta) \mathbf{j}_3 + (\dot{\psi} S_\beta + \dot{\alpha} C_\beta) \mathbf{k}_3
 \end{aligned} \tag{A.7}$$

Appendix B

Kinetic Energy for Coupled Bending and Torsion Model

A schematic, which depicts the rotating string and disk assembly is given in Fig. 3.7. Let the fixed xyz coordinate frame associated with mutually orthogonal unit vectors $\mathbf{i}, \mathbf{j}, \mathbf{k}$ describe the undeformed geometry of the initially straight string. Additionally, let $x_3y_3z_3$ be the coordinate frame in the deformed configuration with mutually orthogonal unit vectors $\mathbf{i}_3, \mathbf{j}_3, \mathbf{k}_3$ whose origin is located along the centerline of the string. The position vector from the origin of the xyz frame, point O , to an arbitrary material point on the cross-section of the string in the deformed configuration is given by the summation of the position vector from point O to the center of the shaft, plus the distance from the centerline to the material point, which is written as

$$\mathbf{r}_{\mathbf{P}/\mathbf{O}} = \mathbf{r}_{\mathbf{C}/\mathbf{O}} + \mathbf{r}_{\mathbf{P}/\mathbf{C}} \quad (\text{B.1})$$

where

$$\mathbf{r}_{\mathbf{C}/\mathbf{O}} = (x + u(x, t))\mathbf{i} + v(x, t)\mathbf{j} + w(x, t)\mathbf{k} \quad (\text{B.2})$$

$$\mathbf{r}_{\mathbf{P}/\mathbf{C}} = y_3\mathbf{j}_3 + z_3\mathbf{k}_3 \quad (\text{B.3})$$

The scalar quantities $u(x, t)$, $v(x, t)$, and $w(x, t)$ are the displacements of the centerline of the string along the \mathbf{i} , \mathbf{j} , and \mathbf{k} directions, respectively. Next, assuming an initially straight string in the xyz frame and also using Bernoulli-Euler beam theory (i.e., the centerline of the string is always normal to the cross-sectional area and

neglecting shear), the following relations between the initial and local frame can be shown.

$$y_3 = y, \quad z_3 = z \quad (\text{B.4})$$

On substituting equations (B.2), (B.3), and (B.4) into (B.1), the position vector from the origin of the xyz frame to an arbitrary material point is then given by

$$\mathbf{r}_{\mathbf{P}/\mathbf{O}} = (x + u(x, t))\mathbf{i} + v(x, t)\mathbf{j} + w(x, t)\mathbf{k} + y\mathbf{j}_3 + z\mathbf{k}_3 \quad (\text{B.5})$$

The velocity of an the material point may then be expressed as

$$\frac{\partial}{\partial t}\mathbf{r}_{\mathbf{P}/\mathbf{O}} \equiv {}^N\frac{\partial}{\partial t}\mathbf{r}_{\mathbf{P}/\mathbf{O}} = {}^N\frac{\partial}{\partial t}\mathbf{r}_{\mathbf{C}/\mathbf{O}} + {}^L\frac{\partial}{\partial t}\mathbf{r}_{\mathbf{P}/\mathbf{C}} + \boldsymbol{\omega} \times \mathbf{r}_{\mathbf{P}/\mathbf{C}} \quad (\text{B.6})$$

In the above expression, the pre-superscript N denotes the time derivative in the inertial frame xyz and the pre-superscript L denotes the time derivative in the local frame $x_3y_3z_3$, and $\boldsymbol{\omega} = \omega_1\mathbf{i}_3 + \omega_2\mathbf{j}_3 + \omega_3\mathbf{k}_3$ is the angular velocity vector; the different components are determined through a series of 1-2-3 Euler angles given in Appendix

A. Upon substitution into equation (B.6), the result is

$$\frac{\partial}{\partial t}\mathbf{r}_{\mathbf{P}/\mathbf{O}} = \begin{Bmatrix} u(x, t) \cdot \mathbf{i} \\ v(x, t) \cdot \mathbf{j} \\ w(x, t) \cdot \mathbf{k} \end{Bmatrix} + \begin{Bmatrix} 0 \cdot \mathbf{i}_3 \\ 0 \cdot \mathbf{j}_3 \\ 0 \cdot \mathbf{k}_3 \end{Bmatrix} + \begin{Bmatrix} \omega_1 \cdot \mathbf{i}_3 \\ \omega_2 \cdot \mathbf{j}_3 \\ \omega_3 \cdot \mathbf{k}_3 \end{Bmatrix} \times \begin{Bmatrix} 0 \cdot \mathbf{i}_3 \\ y \cdot \mathbf{j}_3 \\ z \cdot \mathbf{k}_3 \end{Bmatrix} \quad (\text{B.7})$$

$$= \begin{Bmatrix} u(x, t) \cdot \mathbf{i} \\ v(x, t) \cdot \mathbf{j} \\ w(x, t) \cdot \mathbf{k} \end{Bmatrix} + \begin{Bmatrix} (z\omega_2 - y\omega_3) \cdot \mathbf{i}_3 \\ -z\omega_1 \cdot \mathbf{j}_3 \\ y\omega_1 \cdot \mathbf{k}_3 \end{Bmatrix} \quad (\text{B.8})$$

The kinetic energy of the entire string is then the kinetic energy of all material points on the string, and this energy can be expressed as the following integral

$$\mathcal{T} = \frac{1}{2} \int_{Vol} \rho (\mathbf{r}_{\mathbf{P}/\mathbf{O},t} \cdot \mathbf{r}_{\mathbf{P}/\mathbf{O},t}) dVol \quad (\text{B.9})$$

$$= \frac{1}{2} \int_0^L \int_A \rho (\mathbf{r}_{\mathbf{P}/\mathbf{O},t} \cdot \mathbf{r}_{\mathbf{P}/\mathbf{O},t}) dA dx \quad (\text{B.10})$$

In the above expression, ρ is the mass density of the string, A is the cross sectional area, and Vol is the volume of the string. It proves useful to cast equation (B.10) into matrix-vector notation as follows:

$$\mathcal{T} = \frac{1}{2} \int_0^L \int_A \rho \begin{Bmatrix} \dot{u} \cdot \mathbf{i} \\ \dot{v} \cdot \mathbf{j} \\ \dot{w} \cdot \mathbf{k} \end{Bmatrix}^T \begin{bmatrix} 1 & 0 & 0 \\ 0 & 1 & 0 \\ 0 & 0 & 1 \end{bmatrix} \begin{Bmatrix} \dot{u} \cdot \mathbf{i} \\ \dot{v} \cdot \mathbf{j} \\ \dot{w} \cdot \mathbf{k} \end{Bmatrix} dA dx + \quad (\text{B.11})$$

$$\frac{1}{2} \int_0^L \int_A \rho \begin{Bmatrix} \omega_1 \cdot \mathbf{i}_3 \\ \omega_2 \cdot \mathbf{j}_3 \\ \omega_3 \cdot \mathbf{k}_3 \end{Bmatrix}^T \begin{bmatrix} y^2 + z^2 & 0 & 0 \\ 0 & z^2 & -zy \\ 0 & -zy & y^2 \end{bmatrix} \begin{Bmatrix} \omega_1 \cdot \mathbf{i}_3 \\ \omega_2 \cdot \mathbf{j}_3 \\ \omega_3 \cdot \mathbf{k}_3 \end{Bmatrix} dA dx \quad (\text{B.12})$$

The explicit functional dependence on x and t have been dropped for notational convenience. Additionally, the quantity

$$\mathbb{I} = \rho \begin{bmatrix} y^2 + z^2 & 0 & 0 \\ 0 & z^2 & -zy \\ 0 & -zy & y^2 \end{bmatrix} \quad (\text{B.13})$$

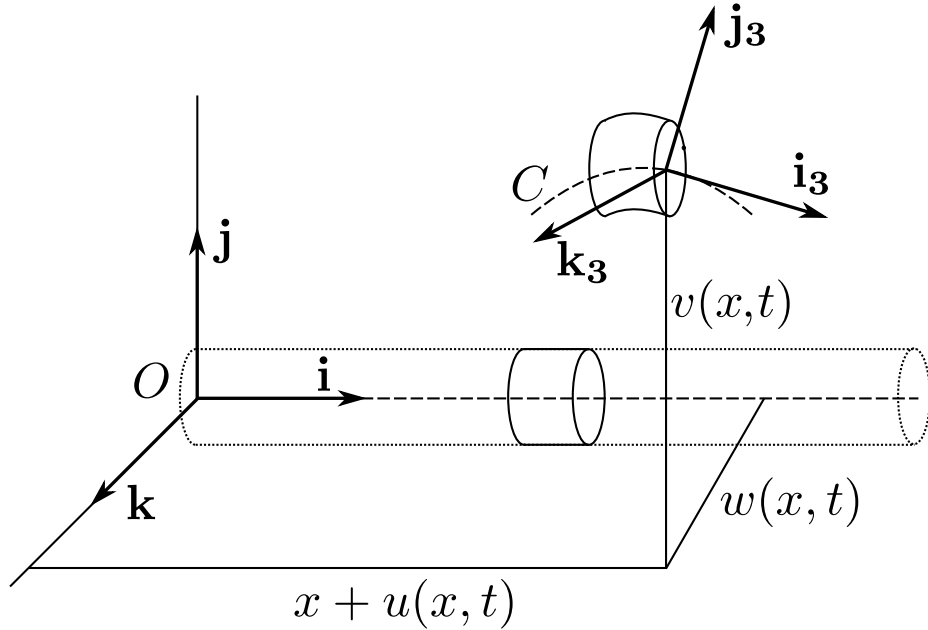


Figure B.1: Segment of the shaft in both the undeformed and deformed configuration.

is recognized as the mass moment of inertia tensor of the cross-sectional area. If the local coordinate frame aligns with the principal axes of inertia of the string, then the off diagonal quantities $\int_A zy dA = 0$. Also,

$$I_o = \int_A (z^2 + y^2) dA \quad (\text{B.14})$$

and for a symmetric cross-sectional area

$$I = \int_A y^2 dA = \int_A z^2 dA \quad (\text{B.15})$$

In the above two expressions I_o is the polar moment of inertia and I is the moment of inertia about the z and y axes, which is referred to as the diametral moment of inertia. Performing the necessary matrix operations the scalar quantity (B.12) may be written as

$$\mathcal{T}_{shaft} = \frac{1}{2} \int_0^L [\rho A(\dot{u}^2 + \dot{v}^2 + \dot{w}^2) + \rho I_o \omega_1^2 + \rho I(\omega_2^2 + \omega_3^2)] dx \quad (\text{B.16})$$

Appendix C

Coefficients for Coupled Bending and Torsional Model

The coefficients used in equation (3.19) are as follows:

$$a_1 = [(M + m)\phi_v^2 + I_D\phi_v'^2] \Big|_{x=L} \quad (\text{C.1})$$

$$a_2 = 2\zeta_b\sqrt{a_1a_4} \quad (\text{C.2})$$

$$a_3 = I_{Do}\phi_v'\phi_w' \Big|_{x=L} \quad (\text{C.3})$$

$$a_4 = \int_0^L (EI\phi_v''^2 - S\phi_v''\phi_v) dx + S\phi_v'\phi_v \Big|_{x=L} \quad (\text{C.4})$$

$$a_5 = I_{Do}\phi_v'\phi_\theta\phi_w' \Big|_{x=L} \quad (\text{C.5})$$

The coefficients that appear in equation (3.20) are given by

$$b_1 = [(M + m)\phi_w^2 + I_D\phi_w'^2] \Big|_{x=L} \quad (\text{C.6})$$

$$b_2 = 2\zeta_b\sqrt{b_1b_4} \quad (\text{C.7})$$

$$b_3 = -I_{Do}\phi_w'\phi_v' \Big|_{x=L} \quad (\text{C.8})$$

$$b_4 = \int_0^L (EI\phi_w''^2 - S\phi_w''\phi_w) dx + S\phi_w'\phi_w \Big|_{x=L} \quad (\text{C.9})$$

$$b_5 = -I_{Do}\phi_w'\phi_\theta\phi_v' \Big|_{x=L} \quad (\text{C.10})$$

The coefficients in equation (3.21) take the form

$$c_1 = (I_{Do} + me^2)\phi_\theta^2 \Big|_{x=L} \quad (\text{C.11})$$

$$c_2 = 2\zeta_t\sqrt{c_1c_3} \quad (\text{C.12})$$

$$c_3 = GI_o \int_0^L \phi_\theta'^2 dx \quad (\text{C.13})$$

$$c_4 = I_{Do} \phi_\theta \phi_v' \phi_w' |_{x=L} \quad (\text{C.14})$$

Appendix D

Modal Analysis of Pre-stressed Semi-circular Configurations

Within this appendix, a special case is considered where an initially straight beam is bent to form various semi-circular configurations. The natural frequencies are then determined about this semi-circular static configuration. First, consider an initially straight undeformed and unstressed rod, that sits along the \mathbf{i} direction with arclength $s \in [0, L]$. In order to realize the semi-circular configuration, the boundary conditions are selected to be

$$\mathbf{r}(0) = 0\mathbf{i} + 0\mathbf{j} \tag{D.1a}$$

$$\theta(0) = 0 \tag{D.1b}$$

$$\mathbf{r}(L) = \frac{L}{2\pi\xi} \sin(2\pi\xi) \mathbf{i} + \frac{L}{2\pi\xi} [1 - \cos(2\pi\xi)] \mathbf{j} \tag{D.1c}$$

$$\theta(L) = 2\pi\xi. \tag{D.1d}$$

Here, $\xi \in (0, 1]$ is a constant and determines the formation of the circle. Representative curves are as follows: $\xi = 1/4$ represents a quarter-circle, $\xi = 1/2$ represents a half-circle, and $\xi = 1$ represents a complete circle. Note that when $\xi = 0$, the initially straight rod is subject to fixed-fixed boundary conditions. Since the rod is assumed to be inextensible, then it cannot vibrate.

Static Analysis

A solution which satisfies equations (4.15) and the boundary conditions given by equations (D.1) is $\theta = \frac{2\pi\xi s}{L}$. This form for the angle has been heuristically chosen and satisfies the governing equation as well as the boundary conditions. After substitution into equation (4.15), the Lagrange Multipliers, namely the reaction forces N_1 and N_2 , become zero. Therefore, only the constant couple $M_o = \frac{-EI2\pi\xi}{L}$ exists throughout the rod. Solving for the position of the centerline of the rod by integrating the second and third equations of (4.15), leads to the total solution

$$\theta = \frac{2\pi\xi}{L}s \quad (\text{D.2a})$$

$$x = \frac{L}{2\pi\xi} \sin\left(\frac{2\pi\xi}{L}s\right) \quad (\text{D.2b})$$

$$y = \frac{L}{2\pi\xi} \left[1 - \cos\left(\frac{2\pi\xi}{L}s\right)\right]. \quad (\text{D.2c})$$

The static configuration of a rod for $\xi = 1/4, 1/2, 3/4$, and 1 are shown in Fig. D.1. In Figure D.1, the analytical solution is given by (D.2), while the numerical solutions have been determined from equations (4.36) and (D.1) by using the scheme mentioned in Section 4.1.3. The static configuration of the curved beam was also determined with finite elements as described in Section 4.3. In the following subsection, the natural frequencies and mode shapes of the structure about these static configurations are presented.

Modal Analysis: Natural Frequencies and Mode Shapes

As mentioned in the previous subsection, for semi-circular and circular configurations, the reaction forces N^o and H^o are zero and the curvature μ^o is a constant.

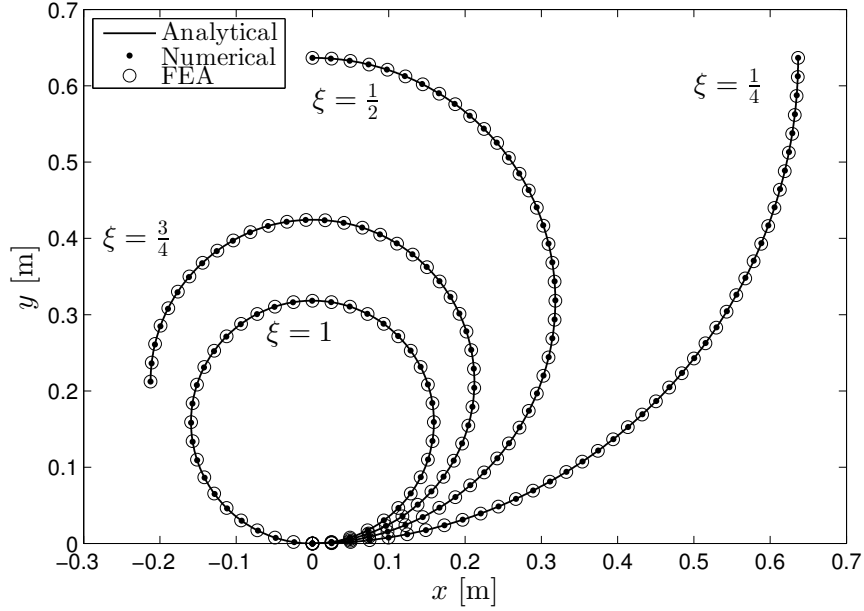


Figure D.1: Four different configurations for the semi-circle parameter ξ that satisfies equations (4.15) with boundary conditions (D.1). The analytical solution is given by equations (D.2), and numerical solutions are obtained through direct integration of equations (4.15) with boundary conditions (D.1).

With this in mind, and in consonance with the earlier assumption of Bernoulli-Euler constitutive relations, equation (4.34) reduces to the following form

$$\rho A \partial_{tt} \bar{u} - \frac{\rho A}{\mu_o^2} \partial_{ttss} \bar{u} - \mu_o^2 EI \partial_{ss} \bar{u} - 2EI \partial_s^{IV} \bar{u} - \frac{EI}{\mu_o^2} \partial_s^{VI} \bar{u} = 0. \quad (\text{D.3})$$

It is noted that the superscript o on the static curvature has been moved to a subscript for notational convenience, and the quantities ∂_s^{IV} and ∂_s^{VI} denote the fourth and sixth partial derivatives with respect to s , respectively. This sixth-order differential equation is properly defined for two initial conditions in time and the six boundary conditions given by equations (4.33). The solution to equation (D.3) is assumed to be separable in space and time and decomposable as $\bar{u} = e^{i\omega t} U(s)$. After substituting the assumed solution into (D.3), the following ordinary differential

equation is obtained

$$\frac{d^6 U}{ds^6} + 2\mu_o^2 \frac{d^4 U}{ds^4} + \left(\mu_o^4 - \frac{\rho A \omega^2}{EI} \right) \frac{d^2 U}{ds^2} + \frac{\mu_o^2 \rho A \omega^2}{EI} U = 0. \quad (\text{D.4})$$

A note of historical context is briefly addressed here. Equation (D.4) represents the spatial displacement U from the static, circular configuration as a function of the initial arc length s . Taking advantage of the fact that the static configuration is circular, the system (D.4) can be transformed into polar coordinates (with independent angular variable α) through the transformation $\alpha = \mu_o s$. After this transformation, and noting that the radius of the circular static configuration is $R_o = 1/\mu_o$, equation (D.4) may be expressed as

$$\frac{d^6 U}{d\alpha^6} + 2 \frac{d^4 U}{d\alpha^4} + \left(1 - \frac{\rho A R_o^4 \omega^2}{EI} \right) \frac{d^2 U}{d\alpha^2} + \frac{\rho A R_o^4 \omega^2}{EI} U = 0. \quad (\text{D.5})$$

Equation (D.5) is the classical differential equation used to determine the natural frequencies and mode shapes of unshearable, inextensible rings found in textbooks such as that by Love (1944). However, it is noted that the solutions of equation (D.4) are not, in general, the same as those exhibited by that of the classical problem of free-vibration of a ring, given by (D.5). This difference can be discerned from the roots of the characteristic polynomial, and implementation of the boundary conditions.

The remaining analysis is carried out by using the initial arc length s as the independent variable. The system (D.4) has an algebraic equivalent solution of the exponential form

$$U(s) = C_1 e^{\lambda_1 s} + C_2 e^{\lambda_2 s} + C_3 e^{\lambda_3 s} + C_4 e^{\lambda_4 s} + C_5 e^{\lambda_5 s} + C_6 e^{\lambda_6 s}. \quad (\text{D.6})$$

The eigenvalues, denoted by λ_i (for $i = 1, 2, \dots, 6$), are determined through the characteristic polynomial

$$\begin{aligned} \sigma^3 + 2a\sigma^2 + (a^2 - b)\sigma + ab &= 0 \\ \lambda &= \pm\sqrt{\sigma} \end{aligned} \tag{D.7}$$

where

$$a = \mu_o^2, \text{ and} \quad b = \frac{\rho A \omega^2}{EI}. \tag{D.8}$$

The quantity a physically represents the square of the initial curvature and the quantity b is the eigenvalue of the classic linear beam equation. Equation (D.4) represents a differential eigenvalue problem, with six unknown coefficients C_i (for $i = 1, 2, \dots, 6$), and one unknown parameter, namely the natural frequency ω . Five of the unknown coefficients are obtained by implementing the boundary conditions given by equations (4.33). The sixth boundary condition of (4.33) is then used to find the system characteristic equation. The roots of the system characteristic equation are used to find the natural frequencies ω . Since the system (D.4) is homogeneous, the amplitude cannot be uniquely determined and the last coefficient may be selected arbitrarily or through a normalization process. Algebraic forms of the coefficients C_i are very large and must either be solved for by symbolic computation (e.g. MathematicaTM) or through numerical methods.

The first seven natural frequencies determined for four different semi-circular and circular trajectories ($\xi = 1/4, 1/2, 3/4,$ and 1) are provided in Table D.1. The corresponding mode shapes are provided in Fig. D.2. The rod is assumed

to have a uniform circular cross-section and properties such that $R = 0.005$ m, $L = 1$ m, $EI = 0.625$ Nm², and $\rho A = 0.25$ kg/m, which are the same values as that chosen for the rod presented in Section 4.1.3. The natural frequencies predicted by the model are also compared to results obtained from the finite element software ANSYS, as described in Section 4.3. Here, 2000 beam elements are used to discretize the structure. The difference in the predicted natural frequencies in going from 1000 to 2000 elements was found to be negligible. The modeling predictions are sufficient for predicting the lower natural frequencies of the structures; however, the model cannot predict certain higher-order frequencies and modes with coupled axial-bending motions. The formulation outlined here cannot predict these frequencies because of the imposed inextensionality assumption. This is highlighted in Table D.1, where the difference between the model predictions and FEA for the mode 6 and $\xi = 1/4$ is higher in comparison to the other predictions. Furthermore, between mode 6 and mode 7, the FEA predicted another natural frequency at 157.64 Hz. As observed in ANSYS, this mode exhibits strong axial-bending coupling, and has been omitted from Table D.1. For slender structures, the formulation is capable of predicting the lower-order natural frequencies and mode shapes.

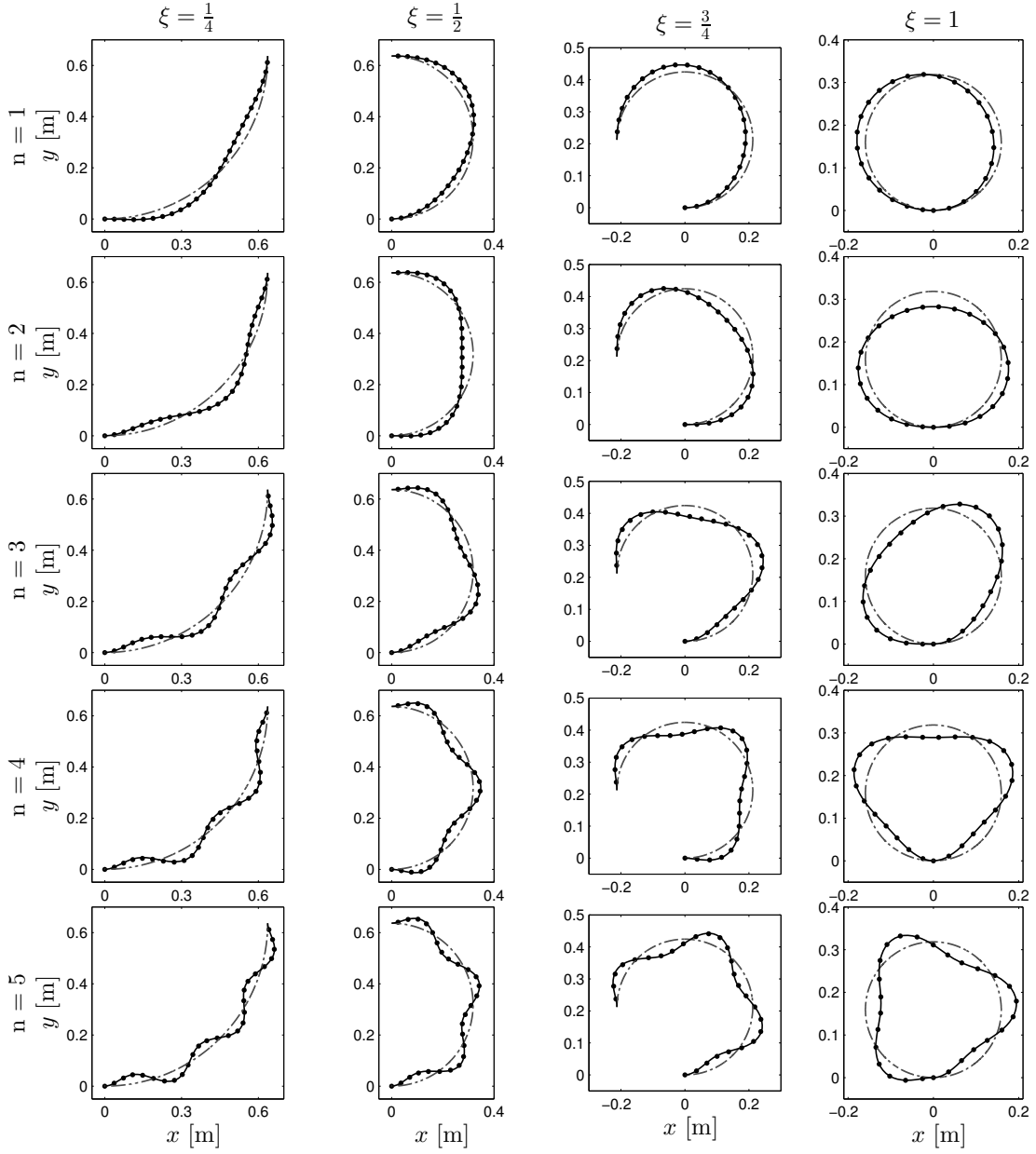


Figure D.2: Comparisons of the mode shapes determined from the model and the finite element modeling. Thin dashed lines represent the static configuration. Solid black lines are the mode shapes determined by the model, given by the differential eigenvalue problem (D.4) and spatial solution, equation (D.6).

Table D.1: Natural frequencies for different semi-circular configurations predicted by the model and found with finite elements. *The finite element analysis also includes a prediction of a natural frequency at 157.64 Hz, which is omitted because it is associated with a combination of bending and centerline stretching.

Mode	$\xi = 1/4$		$\xi = 1/2$		$\xi = 3/4$		$\xi = 1$	
	Theory [Hz]	FEA [Hz]	Theory [Hz]	FEA [Hz]	Theory [Hz]	FEA [Hz]	Theory [Hz]	FEA [Hz]
1	14.05	14.02	10.88	10.87	7.195	7.780	5.627	5.168
2	26.86	26.68	23.97	23.88	20.03	19.97	15.85	15.80
3	48.58	48.37	44.51	44.30	39.35	39.16	33.62	33.47
4	71.67	70.59	68.36	67.83	63.36	62.93	57.17	56.80
5	103.1	102.3	98.84	98.00	93.13	92.34	86.33	85.60
6	136.3	*129.1	132.8	131.0	127.4	126.0	120.5	119.2
7	177.6	175.4	173.2	170.8	167.3	165.0	160.0	157.9

Appendix E

ANSYS Input File for Experimental Parameters

```
!Nick Vlajic
!April 23, 2013
!Modal analysis of a prestress curved beam in ANSYS using beam
!elements.
!Finish
!/clear

fileNameToSave = 'CurvedExperiment'
/filename,fileNameToSave
/PREP7
Pi = acos(-1)
YoungsModulus = 70e9 !Young's modulus of elasticity [Pa]
PoissonsRatio = 0.33 !Poisson's ratio [-]
Radius = 0.001588 ![meters]
Length = 1.5057 ![meters]
zRotation = Pi/2 ![radians]
xDisp = -0.4157 ![meters]
yDisp = 0.833 ![meters]
zDisp = 0 ![meters]
NumberOfModes = 16 ![-]

ET,1,BEAM189 !3 node beam element
SECTYPE, 1, BEAM, CSOLID, , 0 !Defining beam cross-section
SECOFFSET, CENT !Defining beam cross-section
SECDATA,Radius,0,0,0,0,0,0,0,0,0,0,0,0 !Defining beam cross-section

MPTEMP,,,,,,,, !Defining material properties
MPTEMP,1,0 !Defining material properties
MPDATA,EX,1,,YoungsModulus !Defining material properties
MPDATA,PRXY,1,,PoissonsRatio !Defining material properties
MPDATA,DENS,1,,2700 !Defining material properties
```

```

K,1,0,0,0 !Keypoint for end of the rod at the origin
K,2,Length,0,0 !Keypoint for end of the rod at the length

LSTR, 1, 2 !Connect the key points
lesize, 1,,1000 !Define the number of elements between points
LMESH, 1 !Mesh the line

!-----!
!   Static analysis
!-----!

/SOL
ANTYPE,STATIC !Static analysis
numSteps = 10 !Total number of load steps for static analysis
startAxialDisp = 3 !Beam will buckle (zero-stiffness), so need
!to start the beam in bending, then apply axial disp.
*DO,icount,1,numSteps,1
/prep7

!Applying the boundary conditions at one end of the rod
nselect,s,node,,1
d,all,ux,0 !Fix displacement in the x-direction
d,all,uy,0 !Fix displacement in the y-direction
d,all,uz,0
d,all,rotx,0
d,all,roty,0
d,all,rotz,0

!Calculating the boundary conditions to apply at the other end
of the rod
zRotationStep = zRotation*(icount/numSteps)
yDispStep = (icount/numSteps)*yDisp

*IF,icount,le,startAxialDisp,THEN
xDispStep = 0
*ELSE

```

```
xDispStep=(icount-startAxialDisp)/(numSteps-startAxialDisp)*xDisp
*ENDIF
```

```
!Applying the boundary conditions at the other end of the rod
nselect,s,node,,2
d,all,ux,xDispStep
d,all,uy,yDispStep
d,all,uz,0
d,all,rotx,0
d,all,roty,0
d,all,rotz,zRotationStep
```

```
neqit, 10 !Number of equilibrium points
nlgeom, on !Nonlinear geometry on or off
pstres, on !Prestress needed for modal analysis -- needs to
!be called twice, once for the static case and once for
!the dynamic case
```

```
FINISH
/config,nres,1e5
```

```
/sol
nsubst,20,500,10 !Number of substeps between each load
time,icount !Update the "time"
```

```
nselect,all !Select all nodes
solve !Solve
```

```
FINISH
/sol
antype,,rest !Restart for next step of the analysis
```

```
*ENDDO
```

```
!-----!
! Save the static solution
!-----!
```

```

/post1
SET,,, ,,, ,numSteps
nsel,all !Select all the nodes
/HEADER, OFF, OFF, OFF, OFF
/PAGE,5000,500,5000,500
/FORMAT,3,,15,7

fileNameToSave2 = 'CurvedExpStaticConfig'

/output,fileNameToSave2,txt
/HEADER,OFF,OFF,OFF,OFF

prnsol,u !Write displacements for each node
/out

/post1
SET,,, ,,, ,numSteps
!pldisp,1

!-----!
!  Modal Analysis
!-----!

FINISH
/sol
ANTYPE, MODAL !Modal analysis
UPCOORD,1.0,ON !Display the mode shapes relative to the deformed
!geometry in the post processor
PSTRES, ON !Use the prestressed matrix
MODOPT, LANB, NumberOfModes !Eigensolver and number of modes
MXPAND, NumberOfModes !Number of modes to expand
PSOLVE, EIGLANB !Calculates the eigenvalues and eigenvectors
!(must match MODOPT command -- either EIGLANB EIGSNODE)

FINISH
/solu

```



```

EXPASS, ON
PSOLVE, EIGEXP !Expands to eigenvector solution to see the mode
!  shapes in the postprocessor

FINISH

!-----!
!  Save the mode shapes
!-----!

*DO,i1,1,NumberOfModes,1

name1 = 'CurvedExp'
name2 = strcat('_Mode_',chrval(i1))
fileNameToSave3 = strcat(name1,name2)

/post1
SET,,, ,,, ,i1
nsel,all !Select all the nodes
/HEADER, OFF, OFF, OFF, OFF
/PAGE,5000,500,5000,500
/FORMAT,3,,15,7
/output,fileNameToSave3,txt
/HEADER,OFF,OFF,OFF,OFF

prnsol,u !Write displacements for each node
/out
pldisp,1

*ENDDO

```

Bibliography

- Addressi, D., Lacarbonara, W., and Paolone, A.** (2005). On the linear normal modes of planar pre-stressed curved beams. *Journal of Sound and Vibration*, **284**:(3), 1075-1097.
- Anderson, T.J., Nayfeh, A.H. and Balachandran, B.** (1996). Experimental verification of the importance of the nonlinear curvature in the response of a cantilever beam. *Journal of Vibration and Acoustics*, **118**:(1), 21-26.
- Anderson, T.J., Nayfeh, A.H. and Balachandran, B.** (1996). Coupling between high-frequency and a low-frequency mode: Theory and experiment. *Nonlinear Dynamics*, **11**:17-36.
- Antman, S. S.** (2005). Nonlinear problems of elasticity. *Springer Applied Mathematical Sciences*.
- Argyris, J.** (1982). An excursion into large rotations. *Computer Methods in Applied Mechanics and Engineering*, **32**:85-155.
- Bartha, A. R.** (2000). *Dry friction backward whirl of rotors*. Ph.D. Dissertation, Swiss Federal Institute of Technology, Zurich, Switzerland.
- Black, H. F.** (1967). Synchronous whirling of a shaft within a radially flexible annulus having small radial clearance. *Proceedings of the Institution of Mechanical Engineers*, **181**:(4), 65-73.
- Black, H. F.** (1967). Interaction of a whirling rotor with a vibrating stator across a clearance annulus. *Journal of Mechanical Engineering Science*, **10**:(1), 1-12.
- Blekhman, I. I.** (1976). Method of direct motion separation in problems of vibration acting on nonlinear mechanical systems. *Mechanics of Solids*, **11**:(4), 7-19.
- de Bruin, J. C. A., Doris, A., van de Wouw, N. Heemels, W. P. M. H., and Nijmeijer, H.** (2009). Control of mechanical motion systems with non-collocation of actuation and friction: A Popov criterion approach for input-to-state stability and set-valued nonlinearities. *Automatica*, **45**:405-415.
- Bucciarelli, L. L.** (1982). On the instability of rotating shafts due to internal damping. *Journal of Applied Mechanics*, **49**:425-428.

- Chidamparamm, P. and Leissa, A.W.** (1995). Influence of centerline extensibility on the in-plane free vibration of loaded circular arches. *Journal of Sound and Vibration*, **183**:(5), 779-795.
- Childs, D.W.** (1993). Turbomachinery rotordynamics. *John Wiley & Sons*.
- Childs, D.W. and Bhattacharya, A.** (2007). Prediction of dry-friction whirl and whip between a rotor and a stator. *Journal of Vibration and Acoustics*, **129**:(3), 355-362.
- Christoforou, A. P. and Yigit, A. S.** (1997). Dynamic modelling of rotating drillstrings with borehole interactions. *Journal of Sound and Vibration*, **206**:(2), 243-260.
- Christoforou, A. P. and Yigit, A. S.** (2003). Fully coupled vibrations of actively controlled drillstrings. *Journal of Sound and Vibration*, **267**:1029-1045.
- Detournay, E. and Defourny, P.** (1992). A phenomenological model for the drilling action of drag bits. *International Journal of Rock Mechanics and Mining Sciences*, **124**:(2), 209-220.
- Diangui, H.** (2000). Experiment on the characteristics of torsional vibration of rotor-to-stator rub in turbomachinery. *Tribology International*, **33**:75-79.
- Doris, A., Juloski, A. L., Mihajlovic, N., Heemels, W. P. M. H., van de Wouw, N., and Nijmiejter, H.** (2008). Observer designs for experimental non-smooth and discontinuous systems. *IEEE Transactions on Control Systems Technology*, **16**:(6), 1323-1332.
- Edwards, S., Lees, A. W., and Friswell, M. I.** (1999). The influence of torsion on rotor/stator contact in rotating machinery. *Journal of Sound and Vibration*, **255**:(4), 767-778.
- Feng, Z. C. and Zhang, Z. C.** (2002). Rubbing phenomena in rotor-stator contact. *Chaos, Solitons, and Fractals*, **14**:257-267.
- Genta, G.** (2005) Dynamics of rotating systems. *Springer Science+Business Media, Inc.*

- Hendricks, S. L.** (1986) The effect of viscoelasticity on the vibration of a rotor. *Journal of Applied Mechanics*, **53**:412-416.
- Hosseini, S. A. A. and Khadem, S. E.** (2009a) Free vibrations analysis of a rotating shaft with nonlinearities in curvature and inertia. *Mechanism and Machine Theory*, **44**:272-288.
- Hosseini, S. A. A. and Khadem, S. E.** (2009b) Combination resonances in a rotating shaft. *Mechanism and Machine Theory*, **44**:1535-1547.
- Hsieh, S.C., Chen, J.H., and Lee, A.C.** (2006) A modified transfer matrix method for the coupling lateral and torsional vibrations of symmetric rotor-bearing systems. *Journal of Sound and Vibration*, **289**:294-333.
- Huang, D.G.** (2007) Characteristics of torsional vibrations of a shaft with unbalance. *Journal of Sound and Vibration*, **308**:692-698.
- Ishida, Y., Nagasaka, I., Inoue, T. and Lee, S.** (1996). Forced oscillations of a vertical continuous rotor with geometric nonlinearity. *Nonlinear Dynamics*, **11**:107-120.
- Jansen, J. D.** (1993). Nonlinear dynamics of oilwell drill strings. Ph.D. Dissertation, Delft University, Delft, Netherlands.
- Jeffcott, H. H.** (1919) The lateral vibration of loaded shafts in the neighborhood of a whirling speed: The effect of want of balance. *Philosophy Magazine*, **37**:304-315.
- Jiang, J. and Ulbrich, H.** (2005) The Physical Reason and the Analytical Condition for the Onset of Dry Whip in Rotor-to-Stator Contact Systems. *Journal of Vibration and Acoustics*, **127**:(6), 594-603.
- Karkoub, M., Abdel-Magid, Y. L., and Balachandran, B.** (2009) Drill-string torsional vibration suppression using GA optimized controllers. *Journal of Canadian Petroleum Technology*, **48**:(12), 32-38.
- Kreuzer, E. and Struck, H.** (2003) Mechanical modelling of drill-strings. *Proceedings in Applied Mathematics and Mechanics*, **3**:88-91.

- Khulief, Y. and Al-Sulaiman, F.** (2007) Vibration analysis of drillstrings with self-excited stick-slip oscillations. *Journal of Sound and Vibration*, **299**:(3), 540-558.
- Kreuzer, E. and Struck, H.** (2005) Active damping of spatio-temporal dynamics of drill-strings. *IUTAM Symposium on Chaotic Dynamics and Control of Systems in Processes in Mechanics*, **122**:407-417.
- Kreider, W. and Nayfeh, A.H.** (1998) Experimental investigation of single-mode responses in a fixed-fixed buckled beam. *Nonlinear Dynamics*, **15**:155-177.
- Lacarbonara, W.** (2013). Nonlinear structural mechanics. *Springer*.
- Lacarbonara, W. and Antman, S.S.** (2012) Parametric instabilities of the radial motions of non-linearly viscoelastic shells under pulsating pressures. *International Journal of Non-linear Mechanics*, **47**:461-472.
- Lacarbonara, W., Nayfeh, A.H., and Kreider, W.** (1998) Experimental validation of reduction methods for nonlinear vibrations of distributed-parameter systems: Analysis of a buckled beam. *Nonlinear Dynamics*, **17**:95-117.
- Lacarbonara, W., Paolone, A., and Yabuno, H.** (2004) Modeling of planar nonshallow prestressed beams towards asymptotic solutions. *Mechanics Research Communications*, **31**:301-310.
- Leine, R. I., van Campen, D. H., Kraker, A. D. E., and van den Steen, L.** (1998) Stick-slip vibrations induced by alternate friction models. *Nonlinear Dynamics*, **16**:41-54.
- Leine, R. I., van Campen, D. H., and Keultjes, W. J. G.** (2002) Stick-slip whirl interactions in drillstring dynamics. *Journal of Vibration and Acoustics*, **124**:209-220.
- Leine, R. I. and van Campen, D. H.** (2005) Stick-slip whirl interactions in drillstring dynamics. *IUTAM Symposium on Chaotic Dynamics and Control of Systems and Processes in Mechanics*, 287-296.
- Leine, R. I. and Nijmeijer, H.** (2004) Dynamics and bifurcations of non-smooth mechanical systems. *Springer*.

- Li, H. and Balachandran, B.** (2006) Buckling and free oscillations of composite structures. *Journal of Microelectricalmechanical systems*, **15**:(1), 42-51.
- Li, G. X. and Païdoussis, M. P.** (1994) Impact phenomena of rotor-casing dynamical systems. *Nonlinear Dynamics*, **5**:53-70.
- Li, H., Preidikman, S., Balachandran, B. and Mote Jr., C.D.** (2006) Non-linear free and forced oscillators of piezoelectric microresonators. *Journal of Micromechanics and Microengineering*, **16**:356-367.
- Liao, C. M.** (2011). *Experimental and numerical studies of drill-string dynamics*. Ph.D. Dissertation, University of Maryland, College Park, MD.
- Liao, C.M., Balachandran, B., Karkoub, M., and Abdel-Magid, Y.** (2011) Drill-string dynamics: Reduced-order models and experimental studies. *Journal of Vibration and Acoustics*, **133**:(4), 041008-1 041008-8.
- Liao, C.M., Vljajic, N., Karki, H. and Balachandran, B.** (2012) Parametric studies on drill-string motions. *International Journal of Mechanical Sciences*, **54**:(1), 260-268.
- Love, A.E.H.** (1944). A treatise on the mathematical theory of elasticity. *Dover*.
- Matsunaga, H.** (1996) In-plane vibration and stability of shallow circular arches subject to axial forces. *International Journal of Solids and Structures*, **33**:(4), 469-482.
- Meirovitch, L.** (2001). Fundamental of vibrations. *McGraw-Hill Higher Education*.
- Melakhessou, H., Berloiz, A., and Ferraris, G.** (2003). A nonlinear well-drillstring interaction model. *Journal of Vibration and Acoustics*, **125**:46-52.
- Mihajlovic, N.** (2005). *Torsional and lateral vibrations in flexible rotor systems with friction*. Ph.D. Dissertation, Eindhoven University of Technology.
- Mihajlovic, N., van Veggel, A. A., van de Wouw, N., and Nijmeijer, H.** (2004). Analysis of friction-induced limit cycling in an experimental drill-string system. *Journal of Dynamic Systems, Measurement and Control*, **126**:709-720.

- Mihajlovic, N., van de Wouw, N., Rosielle, P. C. J. N., and Nijmeijer, H.** (2007). Interaction between torsional and lateral vibrations in flexible rotor systems with discontinuous friction. *Nonlinear Dynamics*, **50**:679-699.
- Nagasaka, I., Ishida, Y., and Liu, J.** (2008) Forced oscillations of a continuous asymmetrical rotor with geometric nonlinearity (major critical speed and secondary critical speed). *Journal of Vibration and Acoustics*, **130**:(3).
- Nagasaka, I., Liu, J., and Ishida, Y.** (2010) Forced vibrations of a very slender continuous rotor with geometrical nonlinearity (harmonic and subharmonic resonances). *Journal of Vibration and Acoustics*, **132**:(2).
- Nataraj, C.** (1993) On the interaction of torsion and bending in rotating shafts. *Journal of Applied Mechanics*, **60**:239-241.
- Nayfeh, A. H. and Balachandran, B.** (1995). Applied nonlinear dynamics: Analytical, computational and experimental methods. *John Wiley and Sons Inc.*
- Nayfeh, A.H. and Emam, S.A.** (2008). Exact solution and stability of postbuckling configurations of beams. *Nonlinear Dynamics*, **54**:395-408.
- Nayfeh, A.H. and Kreider, W.** (1995). Investigation of natural frequencies and mode shapes of buckled beams. *AIAA Journal*, **33**:(6), 1121-1126.
- Nayfeh, A. H. and Mook, D.T.** (1979). Nonlinear oscillations. *Wiley*.
- Nayfeh, A. H. and Pai, P. F.** (2004). Linear and nonlinear structural mechanics. *John Wiley and Sons Inc.*
- Nguyen, V. and Balachandran, B.** (2011). Supercavitating vehicles with non-cylindrical, nonsymmetric cavities: Dynamics and instabilities. *ASME J. of Computational Dynamics and Control*, **6**:(4), 041001-1 – 41001-11.
- Oestreich, M., Hinrichs, N., and Popp, K.** (1996). Bifurcation and stability analysis for a non-smooth friction oscillator. *Archive of Applied Mechanics*, **66**:301-314.
- Oh, S.J., Lee, B.K. and Lee, I.W.** (1999). Natural frequencies of non-circular arches with rotatory inertia and shear deformation. *J. of Sound and Vibration*, **219**:(1), 23-33.

- Oh, S.J., Lee, B.K. and Lee, I.W.** (2000). Free-vibrations of non-circular arches with non-uniform cross-section. *Intl. J. of Solids and Structures*, **37**:4871-4891.
- Pai, P. F.** (2007). Highly flexible structures: Modeling, computation, and experimentation. *AIAA Education Series*.
- Piovan, M. T. and Sampaio, R.** (2006). Nonlinear model for coupled vibrations of drill-strings. *Mecanica Computacional*, **25**:1751-1765.
- Pusenjak, R. R. and Oblak, M. M.** (2004). Incremental harmonic balance method with multiple time variables for dynamical system with cubic nonlinearities. *International Journal for Numerical Methods in Engineering*, **59**:255-292.
- Rankin, C.C. and Brogan, F.A.** (1986). An element independent corotational procedure for the treatment of large rotations. *J. of Pressure Vessel Technology*, **108**:165-174.
- Sampaio, R., Piovan, M. T., and Venero Lozano, G.** (2005) Stick-slip patterns in coupled extensional/torsional vibrations of drill-strings. *Mecanica Computacional*, **24**:861-877.
- Sze, K. Y., Chen, S. H. and Huang, J. L.** (2005). The incremental harmonic balance method for nonlinear vibration of axially moving beams. *Journal of Sound and Vibration*, **281**:611-626.
- Shaw, J. and Shaw, S. W.** (1989) Instabilities and bifurcations in a rotating shaft. *Journal of Sound and Vibration*, **132**:(2), 227-244.
- Thomsen, J.J.** (2003) Vibrations and stability. *Springer*.
- Thomsen, J.J.** (1999) Using fast vibrations to quench friction-induced oscillations. *Journal of Sound and Vibration*, **228**:(5), 1079-1102.
- Thomsen, J.J.** (2002) Some general effects of strong high-frequency excitation: Stiffening, biasing and smoothening. *Journal of Sound and Vibration*, **253**:(4), 807-831.

- Tüfekçi, E. and Arpacı, A.** (1998) Exact solution of in-plane vibrations of circular arches with account taken of axial extension, transverse shear and rotary inertia effects. *Journal of Sound and Vibration*, **209**:(5), 845-856.
- Vlajic, N., Liao, C.M., Karki, H. and Balachandran, B.** (2011) Stick-slip and whirl motions of drill strings: Numerical and experimental studies. *ASME IDETC/CIE, DETC2011-47949*.
- Vlajic, N., Liao, C.M., Karki, H. and Balachandran, B.** (2012) Stick-slip motions of a rotor-stator system. *Journal of Vibration and Acoustics*, **136**:(2), 021005-1 – 021005-8.
- Vlajic, N., Liu, X., Karki, H. and Balachandran, B.** (2013) Torsion oscillations of a rotor with continuous stator contact. *International Journal of Mechanical Sciences, under review*.
- Vlajic, N., Liu, X., Karki, H. and Balachandran, B.** (2013) Rotor torsion vibrations in the presence of continuous stator contact. *ASME IMECE, DETC2012/MECH-89195*.
- Vlajic, N., Karki, H. and Balachandran, B.** (2013) Nonlinear rotor response with coupled lateral and torsional motions. *International Symposium on Nonlinear Theory and its Applications (NOLTA)*.
- Vlajic, N., Fitzgerald, T. and Balachandran, B.** (2013) Modal analysis of a geometrically exact planar beam with initial pre-stress and large curvature. *International Journal of Solids and Structures, under review*.
- Wu, J.J.** (2007). Torsional vibration analyses of a damped shafting system using tapered shaft element. *Journal of Sound and Vibration*, **306**:946-954.
- Yabuno, H., Miura, M. and Aoshima, N.** (2004). Bifurcation in an inverted pendulum with tilted high-frequency excitation: Analytical and experimental investigations on the symmetry-breaking of the bifurcation. *Journal of Sound and Vibration*, **273**:493-513.
- Yabuno, H., Kashimura, T. Inoue, T. and Ishida, Y.** (2011). Nonlinear normal modes and primary resonance of horizontally supported Jeffcott rotor. *Nonlinear Dynamics*, **66**:(3), 377-387.

Yamamoto, T. and Ishida, Y. (2002). Linear and Nonlinear Rotordynamics: A Modern Treatment with Applications. *John Wiley and Sons Inc.*

Yigit, A. S. and Christorofou, A. P. (2000) Coupled torsional and bending vibrations of actively controlled drillstrings. *Journal of Sound and Vibration*, **234**:67-83.

Yigit, A. S. and Christoforou, A. P. (2006). Stick-slip and bit-bounce interactions in oil-well drillstrings. *Journal of Energy Resources Technology*, **128**:268-274.